
The Pulsed-DC Plasma Actuator: Characteristics and Stall Control in Axial Compressors and Fans

Ryan C. McGowan

Publication Date

27-11-2017

License

This work is made available under a CC BY 4.0 license and should only be used in accordance with that license.

Citation for this work (American Psychological Association 7th edition)

McGowan, R. C. (2017). *The Pulsed-DC Plasma Actuator: Characteristics and Stall Control in Axial Compressors and Fans* (Version 1). University of Notre Dame. <https://doi.org/10.7274/1c18df68c15>

This work was downloaded from CurateND, the University of Notre Dame's institutional repository.

For more information about this work, to report or an issue, or to preserve and share your original work, please contact the CurateND team for assistance at curate@nd.edu.

THE PULSED-DC PLASMA ACTUATOR:
CHARACTERISTICS AND STALL CONTROL IN AXIAL COMPRESSORS
AND FANS

A Dissertation

Submitted to the Graduate School
of the University of Notre Dame
in Partial Fulfillment of the Requirements
for the Degree of

Doctor of Philosophy

by

Ryan C. McGowan

Thomas C. Corke, Director

Graduate Program in Aerospace and Mechanical Engineering

Notre Dame, Indiana

November 2017

© Copyright by

Ryan McGowan

2017

CC-BY-4.0

THE PULSED-DC PLASMA ACTUATOR:
CHARACTERISTICS AND STALL CONTROL IN AXIAL COMPRESSORS
AND FANS

Abstract

by

Ryan C. McGowan

A new means of powering dielectric barrier discharge (DBD) plasma actuators that utilizes a pulsed-DC waveform is proposed for preventing or delaying stall inception in axial compressors and fans. The plasma actuator arrangement, like most AC DBD designs, has two staggered electrodes that are separated by an insulating dielectric layer. However, instead of an AC voltage input to drive the actuator, the pulsed-DC DBD utilizes a DC voltage source. The DC source is supplied to both electrodes and remains constant in time for the exposed electrode, while a resistor limits the current to the covered electrode. A fast-acting solid-state switch periodically grounds the covered electrode for very short instants and then allows its voltage to rise to the source DC level. This process results in a larger peak induced velocity than that from a purely AC waveform such as a sine or sawtooth wave. Experiments to examine the relevant characteristics for optimizing the pulsed-DC plasma actuator, including frequency, voltage, dielectric material, and static pressure, are presented. A predictive model of stall margin extension (SME) in the Notre Dame Transonic Axial Compressor (ND-TAC) facility is also developed; a plasma-actuator-generated thrust of 300 mN/m is found to result in a 3.4% SME at design conditions. To validate the actuators' ability to interact with and modify the formation of stall cells, a facility

has been designed and constructed around a nonconductive fan rotor. The actuators are installed in the fan casing near the blade tips. The instrumentation allows for the measurement of rotating pressure disturbances (traveling stall cells) in this tip gap region as well as fan performance characteristics including pressure rise and flow rate. The casing plasma actuation successfully reduces the correlation of the rotating stall cells, thereby extending the stall margin of the fan. Various azimuthal arrangements and input voltage levels for the plasma actuator casing treatment are explored to determine optimum conditions.

CONTENTS

Figures	iv
Tables	x
Acknowledgments	xi
Symbols	xii
Chapter 1: Introduction	1
1.1 Pulsed-DC Plasma Actuator	7
1.2 Motivation	9
1.3 Rotating Stall Inception and Control	10
1.4 Objectives	14
Chapter 2: Characterization of the Pulsed-DC Plasma Actuator	16
2.1 Thrust Measurements	16
2.1.1 Experimental Setup	16
2.1.2 Comparison to AC Plasma Actuator	20
2.1.3 Effect of Dielectric Material	20
2.1.4 Effect of Rise Time	23
2.1.5 Effect of Pulse Amplitude	23
2.1.6 Effect of Static Pressure	25
2.2 Velocity Profiles	29
Chapter 3: Model for Stall Margin Extension	33
Chapter 4: Preliminary Work in the ND-TAC Facility	37
4.1 ND-TAC Plasma Actuator Stall Control Design	37
4.2 Parylene Tests	40
4.3 Effect of DC Offset	41
4.3.1 Negative Switch	42
4.3.2 Positive Switch	42

Chapter 5: Stall Margin Extension in the Nonconductive Fan Facility	47
5.1 Nonconductive Fan Plasma Actuator Stall Control Design	47
5.1.1 Inlet Throttling Device	48
5.1.2 Test Section	49
5.1.3 Fan	50
5.1.4 Outlet Settling Chamber	50
5.2 Experimental Setup	52
5.3 Stall Cell Measurements	56
5.3.1 Actuators at $x = -0.07c_{ax}$	58
5.3.2 Actuators at $x = 0.12c_{ax}$	73
5.3.3 Actuators at $x = 0.51c_{ax}$	86
5.4 Fan Performance Curve Measurements	99
Chapter 6: Conclusions and Recommendations	105
6.1 Conclusions	105
6.2 Recommendations	107
Appendix A: Actuator Dimensions and Properties	110
Appendix B: MATLAB Functions	112
Bibliography	115

FIGURES

1.1	The AC DBD; (a) schematic illustration of AC DBD plasma actuator; (b) photograph of ionized air at 1 atm pressure that forms over the covered electrode (from Corke et al. [6])	2
1.2	(a) Time series of PMT output from viewing ionized air light emission at one location over the covered electrode; (b) corresponding AC input to plasma actuator (from Orlov [27])	4
1.3	(a) Schematic of experimental setup for measuring induced thrust from DBD plasma actuator; (b) measured thrust versus applied AC voltage (from Thomas et al. [37])	6
1.4	The pulsed-DC DBD; (a) schematic illustration of pulsed-DC DBD plasma actuator; (b) photograph of ionized air at 1 atm pressure that forms over the covered electrode	8
1.5	Example of a performance map for a transonic compressor stage (from Hill and Peterson [16])	11
1.6	Criteria for spike stall inception; (a) tip clearance flow spillage at leading edge; (b) tip clearance flow reversal at trailing edge (from Vo et al. [43])	12
2.1	Pulsed-DC plasma actuator power system based on Phase I circuit . .	17
2.2	Photograph of electronic force-measuring scale and plasma actuator arrangement used for thrust measurements	18
2.3	Schematic illustration of the total experimental setup used for thrust measurements	19
2.4	Time series for a DC input voltage of 7 kV and an actuation frequency of 1 kHz for a 5-in-long actuator; (top) voltage time series supplied by the function generator; (middle) voltage time series supplied to the covered and exposed electrodes of the plasma actuator; (bottom) corresponding current time series	21
2.5	Comparison between the induced thrust from AC and pulsed-DC plasma actuators	22
2.6	Comparison between the induced thrust using Kapton and Ultem dielectric layers	23
2.7	Comparison between time series using $R_{\text{bias}} = 0.2 \text{ M}\Omega$ and $R_{\text{bias}} = 1 \text{ M}\Omega$	24

2.8	Comparison between the induced thrust using $R_{\text{bias}} = 0.2 \text{ M}\Omega$ and $R_{\text{bias}} = 1 \text{ M}\Omega$	24
2.9	Comparison between time series with complete and incomplete switching	25
2.10	Comparison between the induced thrust with complete and incomplete switching	26
2.11	Photographs of the pressure vessel setup used for measuring the effect of static pressure on the pulsed-DC actuator thrust generation	27
2.12	Effect of static pressure on the pulsed-DC actuator thrust for different DC voltages	28
2.13	Effect of DC voltage on the pulsed-DC actuator thrust for different static pressures	28
2.14	Effect of static pressure on the pulsed-DC actuator voltage-thrust transfer function, dF'_p/dV_{supply}	29
2.15	Photographs of the experimental setup used for velocity profile measurements	31
2.16	Normalized velocity profiles for different downstream locations	32
3.1	Schematic of 1-D momentum balance used in estimating effect of pulsed-DC plasma actuator on compressor stall margin	34
3.2	Effect of tip leakage jet origin on required plasma body force	36
4.1	Cutaway drawing of the ND-TAC facility (from Ross[31])	38
4.2	Schematic drawing showing assembly drawing of casing survey ring with inset plasma actuator	39
4.3	Voltage time series supplied by the negative switch to the covered and exposed electrodes of the plasma actuator. Exposed electrode held at 10 kV.	43
4.4	Voltage time series supplied by the negative switch to the covered and exposed electrodes of the plasma actuator. Exposed electrode held at -10 kV	44
4.5	Voltage time series supplied by the positive switch to the covered and exposed electrodes of the plasma actuator. Exposed electrode held at ground.	45
4.6	Effect of negative offset voltage on the positive pulsed-DC actuator thrust. Exposed electrode held at ground.	46
5.1	CAD rendering of test section / fan / settling chamber assembly for the nonconductive fan facility	48
5.2	Photograph of nonconductive fan facility	49

5.3	(a) Full azimuth actuator ring; (b) long exposure photograph of ring during operation	53
5.4	Photograph of actuator arc segment installed in test section	53
5.5	(a) Low-pass filtered pressure traces for various throttle positions ($f_c = 5n$); (b) SCM for various throttle positions	59
5.6	Spatial correlation metric with plasma off and plasma on ($f_c = 5n$). The dark bands represent the locations of the actuator segments. . .	60
5.7	00001000 1 segment configuration ($f = 500$ Hz, $x = -0.07c_{ax}$); (left) mean spatial correlation metric with plasma off and plasma on; (right) reduction in mean spatial correlation metric. The dark bands represent the locations of the actuator segments.	61
5.8	00001000 1 segment configuration ($f = 1$ kHz, $x = -0.07c_{ax}$); (left) mean spatial correlation metric with plasma off and plasma on; (right) reduction in mean spatial correlation metric. The dark bands represent the locations of the actuator segments.	62
5.9	00001000 1 segment configuration ($f = 2$ kHz, $x = -0.07c_{ax}$); (left) mean spatial correlation metric with plasma off and plasma on; (right) reduction in mean spatial correlation metric. The dark bands represent the locations of the actuator segments.	63
5.10	10001000 2 segment configuration ($f = 500$ Hz, $x = -0.07c_{ax}$); (left) mean spatial correlation metric with plasma off and plasma on; (right) reduction in mean spatial correlation metric. The dark bands represent the locations of the actuator segments.	64
5.11	10001000 2 segment configuration ($f = 1$ kHz, $x = -0.07c_{ax}$); (left) mean spatial correlation metric with plasma off and plasma on; (right) reduction in mean spatial correlation metric. The dark bands represent the locations of the actuator segments.	65
5.12	10001000 2 segment configuration ($f = 2$ kHz, $x = -0.07c_{ax}$); (left) mean spatial correlation metric with plasma off and plasma on; (right) reduction in mean spatial correlation metric. The dark bands represent the locations of the actuator segments.	66
5.13	10101010 4 segment configuration ($f = 500$ Hz, $x = -0.07c_{ax}$); (left) mean spatial correlation metric with plasma off and plasma on; (right) reduction in mean spatial correlation metric. The dark bands represent the locations of the actuator segments.	67
5.14	10101010 4 segment configuration ($f = 1$ kHz, $x = -0.07c_{ax}$); (left) mean spatial correlation metric with plasma off and plasma on; (right) reduction in mean spatial correlation metric. The dark bands represent the locations of the actuator segments.	68

5.15	10101010 4 segment configuration ($f = 2\text{ kHz}$, $x = -0.07c_{ax}$); (left) mean spatial correlation metric with plasma off and plasma on; (right) reduction in mean spatial correlation metric. The dark bands represent the locations of the actuator segments.	69
5.16	11111111 8 segment configuration ($f = 500\text{ Hz}$, $x = -0.07c_{ax}$); (left) mean spatial correlation metric with plasma off and plasma on; (right) reduction in mean spatial correlation metric. The dark bands represent the locations of the actuator segments.	70
5.17	11111111 8 segment configuration ($f = 1\text{ kHz}$, $x = -0.07c_{ax}$); (left) mean spatial correlation metric with plasma off and plasma on; (right) reduction in mean spatial correlation metric. The dark bands represent the locations of the actuator segments.	71
5.18	11111111 8 segment configuration ($f = 2\text{ kHz}$, $x = -0.07c_{ax}$); (left) mean spatial correlation metric with plasma off and plasma on; (right) reduction in mean spatial correlation metric. The dark bands represent the locations of the actuator segments.	72
5.19	00001000 1 segment configuration ($f = 500\text{ Hz}$, $x = 0.12c_{ax}$); (left) mean spatial correlation metric with plasma off and plasma on; (right) reduction in mean spatial correlation metric. The dark bands represent the locations of the actuator segments.	74
5.20	00001000 1 segment configuration ($f = 1\text{ kHz}$, $x = 0.12c_{ax}$); (left) mean spatial correlation metric with plasma off and plasma on; (right) reduction in mean spatial correlation metric. The dark bands represent the locations of the actuator segments.	75
5.21	00001000 1 segment configuration ($f = 2\text{ kHz}$, $x = 0.12c_{ax}$); (left) mean spatial correlation metric with plasma off and plasma on; (right) reduction in mean spatial correlation metric. The dark bands represent the locations of the actuator segments.	76
5.22	10001000 2 segment configuration ($f = 500\text{ Hz}$, $x = 0.12c_{ax}$); (left) mean spatial correlation metric with plasma off and plasma on; (right) reduction in mean spatial correlation metric. The dark bands represent the locations of the actuator segments.	77
5.23	10001000 2 segment configuration ($f = 1\text{ kHz}$, $x = 0.12c_{ax}$); (left) mean spatial correlation metric with plasma off and plasma on; (right) reduction in mean spatial correlation metric. The dark bands represent the locations of the actuator segments.	78
5.24	10001000 2 segment configuration ($f = 2\text{ kHz}$, $x = 0.12c_{ax}$); (left) mean spatial correlation metric with plasma off and plasma on; (right) reduction in mean spatial correlation metric. The dark bands represent the locations of the actuator segments.	79

5.25	10101010 4 segment configuration ($f = 500 \text{ Hz}$, $x = 0.12c_{ax}$); (left) mean spatial correlation metric with plasma off and plasma on; (right) reduction in mean spatial correlation metric. The dark bands represent the locations of the actuator segments.	80
5.26	10101010 4 segment configuration ($f = 1 \text{ kHz}$, $x = 0.12c_{ax}$); (left) mean spatial correlation metric with plasma off and plasma on; (right) reduction in mean spatial correlation metric. The dark bands represent the locations of the actuator segments.	81
5.27	10101010 4 segment configuration ($f = 2 \text{ kHz}$, $x = 0.12c_{ax}$); (left) mean spatial correlation metric with plasma off and plasma on; (right) reduction in mean spatial correlation metric. The dark bands represent the locations of the actuator segments.	82
5.28	11111111 8 segment configuration ($f = 500 \text{ Hz}$, $x = 0.12c_{ax}$); (left) mean spatial correlation metric with plasma off and plasma on; (right) reduction in mean spatial correlation metric. The dark bands represent the locations of the actuator segments.	83
5.29	11111111 8 segment configuration ($f = 1 \text{ kHz}$, $x = 0.12c_{ax}$); (left) mean spatial correlation metric with plasma off and plasma on; (right) reduction in mean spatial correlation metric. The dark bands represent the locations of the actuator segments.	84
5.30	11111111 8 segment configuration ($f = 2 \text{ kHz}$, $x = 0.12c_{ax}$); (left) mean spatial correlation metric with plasma off and plasma on; (right) reduction in mean spatial correlation metric. The dark bands represent the locations of the actuator segments.	85
5.31	00001000 1 segment configuration ($f = 500 \text{ Hz}$, $x = 0.51c_{ax}$); (left) mean spatial correlation metric with plasma off and plasma on; (right) reduction in mean spatial correlation metric. The dark bands represent the locations of the actuator segments.	87
5.32	00001000 1 segment configuration ($f = 1 \text{ kHz}$, $x = 0.51c_{ax}$); (left) mean spatial correlation metric with plasma off and plasma on; (right) reduction in mean spatial correlation metric. The dark bands represent the locations of the actuator segments.	88
5.33	00001000 1 segment configuration ($f = 2 \text{ kHz}$, $x = 0.51c_{ax}$); (left) mean spatial correlation metric with plasma off and plasma on; (right) reduction in mean spatial correlation metric. The dark bands represent the locations of the actuator segments.	89
5.34	10001000 2 segment configuration ($f = 500 \text{ Hz}$, $x = 0.51c_{ax}$); (left) mean spatial correlation metric with plasma off and plasma on; (right) reduction in mean spatial correlation metric. The dark bands represent the locations of the actuator segments.	90

5.35	10001000 2 segment configuration ($f = 1 \text{ kHz}$, $x = 0.51c_{ax}$); (left) mean spatial correlation metric with plasma off and plasma on; (right) reduction in mean spatial correlation metric. The dark bands represent the locations of the actuator segments.	91
5.36	10001000 2 segment configuration ($f = 2 \text{ kHz}$, $x = 0.51c_{ax}$); (left) mean spatial correlation metric with plasma off and plasma on; (right) reduction in mean spatial correlation metric. The dark bands represent the locations of the actuator segments.	92
5.37	10101010 4 segment configuration ($f = 500 \text{ Hz}$, $x = 0.51c_{ax}$); (left) mean spatial correlation metric with plasma off and plasma on; (right) reduction in mean spatial correlation metric. The dark bands represent the locations of the actuator segments.	93
5.38	10101010 4 segment configuration ($f = 1 \text{ kHz}$, $x = 0.51c_{ax}$); (left) mean spatial correlation metric with plasma off and plasma on; (right) reduction in mean spatial correlation metric. The dark bands represent the locations of the actuator segments.	94
5.39	10101010 4 segment configuration ($f = 2 \text{ kHz}$, $x = 0.51c_{ax}$); (left) mean spatial correlation metric with plasma off and plasma on; (right) reduction in mean spatial correlation metric. The dark bands represent the locations of the actuator segments.	95
5.40	11111111 8 segment configuration ($f = 500 \text{ Hz}$, $x = 0.51c_{ax}$); (left) mean spatial correlation metric with plasma off and plasma on; (right) reduction in mean spatial correlation metric. The dark bands represent the locations of the actuator segments.	96
5.41	11111111 8 segment configuration ($f = 1 \text{ kHz}$, $x = 0.51c_{ax}$); (left) mean spatial correlation metric with plasma off and plasma on; (right) reduction in mean spatial correlation metric. The dark bands represent the locations of the actuator segments.	97
5.42	11111111 8 segment configuration ($f = 2 \text{ kHz}$, $x = 0.51c_{ax}$); (left) mean spatial correlation metric with plasma off and plasma on; (right) reduction in mean spatial correlation metric. The dark bands represent the locations of the actuator segments.	98
5.43	Fan performance curve for actuators at $x = -0.07c_{ax}$	100
5.44	Fan performance curve for actuators at $x = 0.12c_{ax}$	101
5.45	Fan performance curve for actuators at $x = 0.51c_{ax}$	102
A.1	Test article geometry and dimensions	111

TABLES

2.1	Integrated forces	32
5.1	Fan data (at STP)	51
5.2	Function generator settings entered for trigger waveform	54
5.3	Stall margin improvement for various actuator locations	104
A.1	Actuator configurations and nomenclature	111

ACKNOWLEDGMENTS

This work would not have been possible were it not for a support network which is more extensive than I can fully list here. However, I would like to acknowledge a few individuals who have been especially instrumental in the completion of this project.

First of all, I would like to thank my advisor, Dr. Thomas Corke, for his invaluable guidance and support which have propelled me through my graduate career. I would also like to extend my gratitude to the rest of my committee—Dr. Eric Matlis, Dr. Mark Ross, and Dr. Flint Thomas. Without their insights into the complexities of scientific instrumentation, turbomachinery, and fluid mechanics, this work surely would have suffered.

Thank you to all the staff of Hessert Laboratory and the Engineering Machine Shop, including Rod McClain, Gene Heyse, Terry Jacobsen, and Mike Sanders, who worked earnestly to accommodate my research and share their expertise in manufacturing.

Last but not least, I am immensely grateful for my friends and family, who have provided me with their wisdom and encouragement to help me overcome the many challenges of obtaining a Ph.D. I can't overstate how much it means to me to know you are with me in my struggles and triumphs.

The funding for this research came from NASA SBIR Phase I and II contracts NNX13CC27P and NNX14CC12C in cooperation with Creare. It was also supported in part by the Notre Dame Center for Research Computing.

SYMBOLS

c	rotor blade chord
c_{ax}	rotor blade axial chord
C_{dcv}	coefficient of drag for 1-D analysis control volume
D	compressor annulus outer diameter
f	frequency
F_p	plasma actuator body force
F'_p	normalized plasma actuator body force
I	current
K_{Ac}	actual-to-approximated tip leakage jet axial momentum ratio
l	length
\dot{m}	physical mass flow
n	rotational frequency of impeller
n_r	rotor blade count
N	rotational speed of impeller
P	static pressure
P_0	total pressure
\tilde{Q}	approximated tip leakage jet axial momentum flux per unit area
Q_0	approach flow momentum flux per unit area
R	windowed cross-correlation function
R_{bias}	bias resistance
SME	stall margin extension
t	thickness, time

T	static temperature
T_0	total temperature
u	streamwise velocity
V	voltage
w	width
x	streamwise coordinate
x_0	virtual origin of the tip leakage jet
x_{zs}	axial location of the line of zero axial shear
y	wall-normal coordinate
δ	boundary layer thickness, ratio of inlet total pressure to reference pressure
η	adiabatic efficiency
θ	circumferential location, ratio of inlet total temperature to reference temperature
π	total pressure ratio
ρ	density
τ	time lag, tip clearance height
χ	spatial correlation metric

CHAPTER 1

INTRODUCTION

In the last fifteen years, there has been a tremendous growth in the study of dielectric barrier discharge (DBD) “plasma actuators” for flow control. Compared to other methods of flow control (such as blowing/suction, roughness strips, vortex generators, etc.), DBD plasma actuators have a number of unique advantages. These include:

- Being fully electronic with no moving parts (thus reducing or eliminating mechanical fatigue)
- A fast time response for unsteady applications
- A very low mass which is especially important in applications with high g-loads
- A low profile that allows them to be applied to surfaces without the addition of cavities or holes
- An efficient conversion of the electric input energy to kinetic energy when properly optimized [12, 27, 32]
- The ability to easily simulate their effect in numerical flow solvers [5, 27]
- A low manufacturing cost

The predominant DBD configuration used for flow control consists of two metal electrodes separated by a single layer of dielectric material; hence this configuration is known as the single dielectric barrier discharge (SDBD). One electrode remains uncoated and exposed to the air, while the other is encapsulated by the dielectric material. For plasma actuator applications, the electrodes are generally arranged in a highly asymmetric geometry such as is shown in Figure 1.1a. In this work

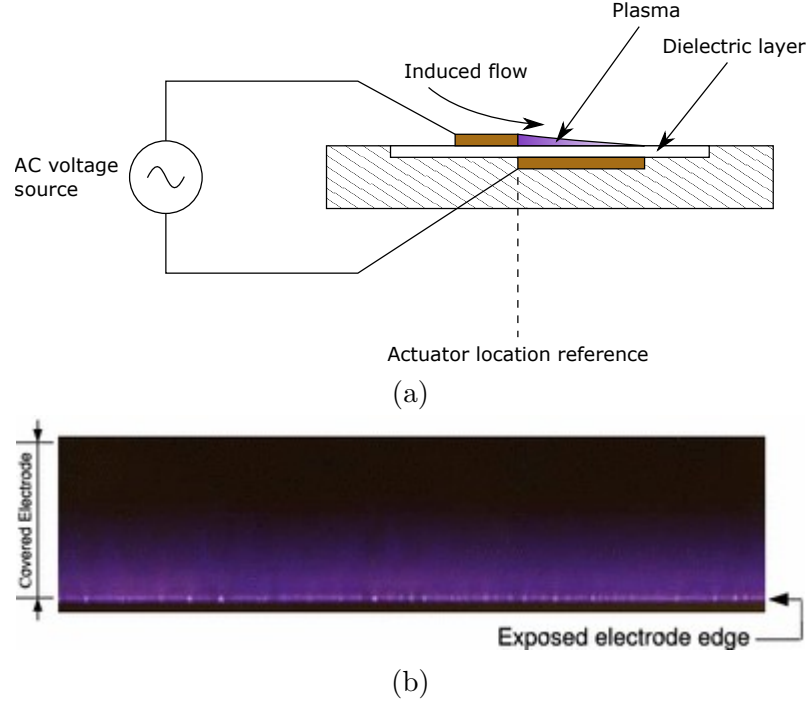


Figure 1.1. The AC DBD; (a) schematic illustration of AC DBD plasma actuator; (b) photograph of ionized air at 1 atm pressure that forms over the covered electrode (from Corke et al. [6])

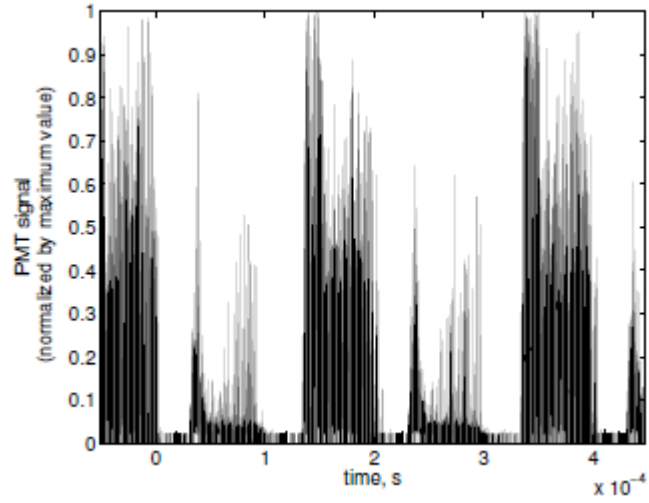
the term “DBD” is used to refer to the SDBD configuration, although other DBD configurations exist in the literature.

DBD actuators can be further categorized based on the shape of the driving voltage waveform supplied to the electrodes. One of the most popular choices of waveform is an AC sine wave, and this type of actuator is known as the AC DBD. When the applied voltage is high enough, the air over the covered electrode becomes weakly ionized. This is typically less than 1 ppm weakly ionized gas. The ionized air produces a blue or purple glow, which is a characteristic of the composition of the air as ionized components of the air recombine and de-excite [8]. The emission intensity is extremely low, requiring a darkened space to view by eye. A photograph of the ionized air produced by an AC plasma actuator is shown in Figure 1.1b.

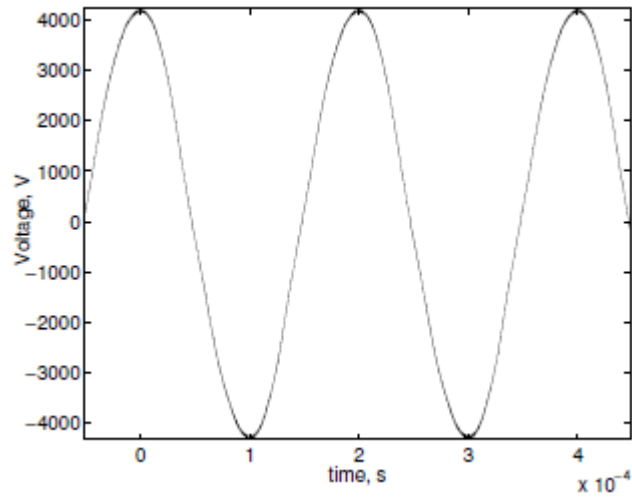
The ionized air, in the presence of the electric field produced by the electrode geometry, results in a body force vector field that acts on the ambient (non-ionized, neutrally charged) air. It is this coupling of the charged air particles' momentum with the surrounding neutral particles that is the mechanism for active aerodynamic control. In determining the response of the ambient air, the body force appears as a term on the right-hand side of the fluid momentum equation.

Enloe et al. [11, 12] studied the space-time evolution of the ionized air light emission over a surface-mounted SDBD plasma actuator using a photomultiplier tube (PMT) fitted with a double-slit aperture to focus on a narrow 2-D region of the plasma. The slit was parallel to the edge of the exposed electrode and could be moved to different locations over the covered electrode. A sample time series from Orlov [27] of the PMT output which was acquired phase-locked with the AC input to the actuator is shown in Figure 1.2a. Also shown for reference in Figure 1.2b is the AC input supplied to the electrodes. The light emission is taken as an indication of the plasma density, which is a good assumption based on the disparate time scales between the recombination time (order of 10^{-8} s) [39] and the discharge time scale (order of 10^{-3} s).

It can be seen from Figure 1.2 that the PMT output is different for each half of the AC cycle. This difference in the emission character can be explained by considering the source of electrons. During the negative-going half cycle, the electrons originate from the bare electrode, which is essentially an infinite source that readily gives them up. These electrons move toward the dielectric where they accumulate locally. In the positive-going half cycle, the electrons originate from the dielectric surface and move back toward the bare electrode. These apparently do not come off as readily, or when they do, they come in the form of fewer, larger micro-discharges. In air at atmospheric pressure, this process takes place over a few tens of nanoseconds [13], but the time scale can differ for other gases, excitation frequencies, and pressures. This



(a)

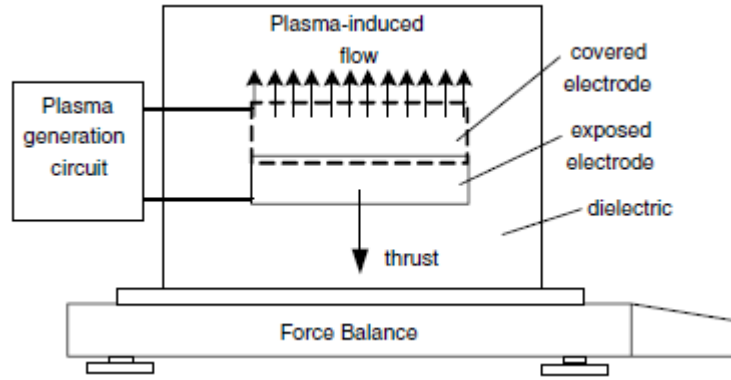


(b)

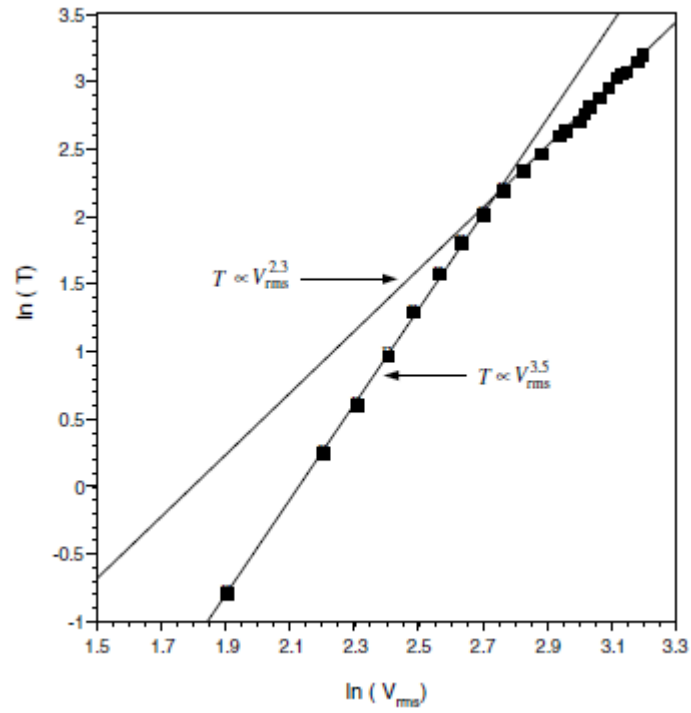
Figure 1.2. (a) Time series of PMT output from viewing ionized air light emission at one location over the covered electrode; (b) corresponding AC input to plasma actuator (from Orlov [27])

asymmetry has been modeled by Boeuf et al. [3] and Orlov et al. [28], and it plays an important role in the efficiency of the momentum coupling to the neutrals. It also suggests that periodic waveforms other than sine waves may be used to improve the performance of the plasma actuator.

In flow control applications, plasma actuators utilizing the offset electrode geometry of Figure 1.1 are typically mounted on an aerodynamic surface and are used to induce a velocity field similar to that of a tangential wall jet. Using a mass balance to measure the reaction force due to the accelerated flow, Enloe et al. [11, 12] correlated the thrust generated by the induced flow with the actuator AC amplitude. A similar experiment was performed by Thomas et al. [37] to investigate other design parameters including dielectric material and thickness, applied voltage amplitude and frequency, voltage waveform, exposed electrode geometry, covered electrode width, and multiple actuator arrays. A schematic of their setup and sample results are shown in Figure 1.3. At lower voltages, the induced thrust was found to be proportional to $V_{rms}^{3.5}$, matching the trend first observed by Enloe et al. [11, 12]. Thomas et al. [37] also used pitot probes and particle image velocimetry (PIV) to measure the velocity profiles downstream of the actuator and then integrated them, thus verifying consistency between the reaction force and the fluid momentum. Post [30] found that the maximum induced velocity was also proportional to $V_{rms}^{3.5}$, which is consistent with conserved momentum in the self-similar velocity profile region near the actuator. At the highest voltages, the thrust change with voltage still appears to follow a power law relation, although the exponent is smaller and not necessarily universally accepted. The voltage at which the power law exponent changes is a function of the area of the covered electrode, with a smaller area causing the change to occur at lower voltages. Further details can be found in the review article by Corke et al. [7].



(a)



(b)

Figure 1.3. (a) Schematic of experimental setup for measuring induced thrust from DBD plasma actuator; (b) measured thrust versus applied AC voltage (from Thomas et al. [37])

1.1 Pulsed-DC Plasma Actuator

As can be inferred from Figure 1.2 and the previous discussion, the body force produced by AC DBD plasma actuators only occurs over a relatively short portion of the AC cycle. In addition, only the portion where the electrons leave the exposed electrode to be deposited onto the dielectric surface has a significant contribution to the net body force. This process of the AC body force generation, visible in Figure 1.2a as two distinct series of spikes per period, is often referred to as “big push, little push.” However, the performance of the actuator could be improved if more air particles were ionized and then exposed to the electric field for a longer fraction of time.

An AC voltage is typically used to power the plasma actuator because it is more effective than DC at ionizing air at atmospheric pressure and higher [19–21, 23, 25]. Ionizing the air makes it conductive and thereby responsive to the electric field. On the other hand, a DC voltage is better at producing a body force if the air is already ionized.

The pulsed-DC plasma actuator is meant to be a hybrid approach that embodies the best aspects of AC and DC plasma actuators. The plasma actuator arrangement is identical to most AC DBD designs (such as was shown in Figure 1.1), with staggered electrodes that are separated by a dielectric insulator. However, instead of an AC voltage input to drive the actuator, the pulsed-DC DBD utilizes a DC voltage source. As shown in the schematic for the pulsed-DC DBD in Figure 1.4a, the DC source is supplied to both electrodes. A resistor, R_{bias} , limits the current to the covered electrode, which is also connected to a fast-acting solid-state switch that shorts the covered electrode to the power supply ground when closed. A periodic trigger signal consisting of a TTL pulse is supplied to activate the solid-state switch. A photograph of the plasma generated by the pulsed-DC operation is shown in Figure 1.4b. There appears to be no discernible differences between its appearance and that of the AC

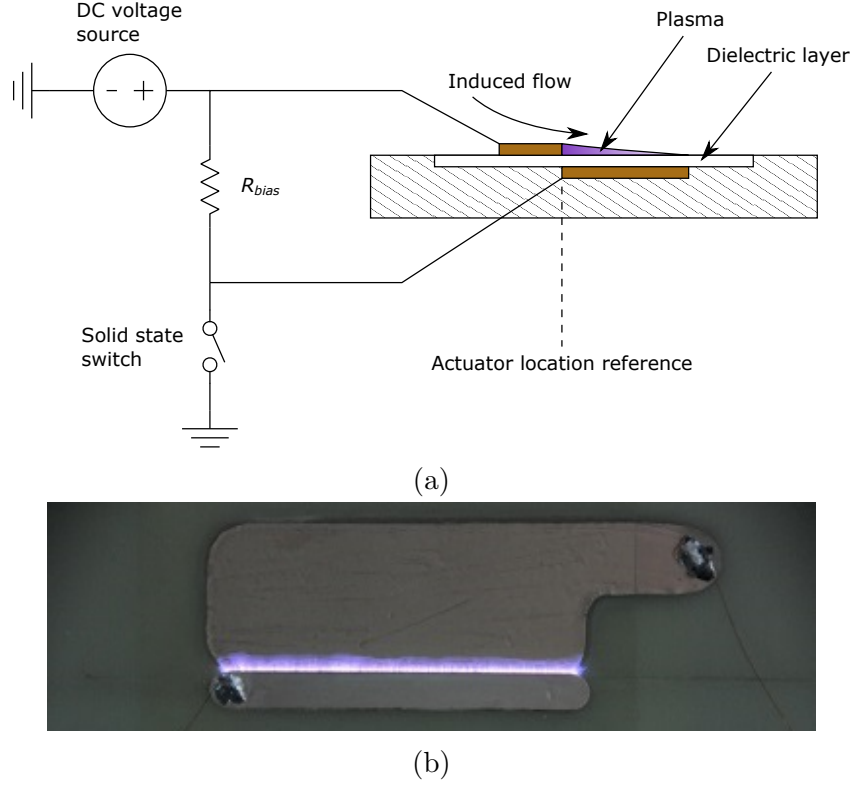


Figure 1.4. The pulsed-DC DBD; (a) schematic illustration of pulsed-DC DBD plasma actuator; (b) photograph of ionized air at 1 atm pressure that forms over the covered electrode

DBD operation, such as was shown in Figure 1.1b.

The breakdown voltage of air at atmospheric pressure is 3.0 MV m^{-1} , but even state-of-the-art transistors are only capable of switching 4500 V maximum. Thus, it is necessary to divide the supply voltage among multiple devices. The fast-acting switch consists of a series-stacked MOSFET design such as was originally presented by Baker and Johnson [2] for high-speed triggering of cameras. The stacked MOSFET topology was later simplified by Hess and Baker [15], who inserted capacitance between adjacent MOSFET gates instead of between each gate and common ground. Mentze [24] derived general analysis and design equations for this circuit, noting that it had the advantages of allowing for the use of capacitors with lower voltage

ratings, improving tolerance to deviations in capacitance values, and reducing the circuit size. The design used for the present results was a five-device stack based on Hess and Baker’s topology.

1.2 Motivation

Due to its improved ability to generate thrust as compared to the AC plasma actuator, the pulsed-DC plasma actuator has many of the same applications in flow control. In this work the pulsed-DC plasma actuator is considered for application in axial compressors and fans.

Axial compressors and fans are important components of modern turbomachines and find application in industries ranging everywhere from air travel to seaborne shipping to power generation. Nonetheless, their performance is limited at low mass flows by a phenomenon known as rotating stall, in which the machine experiences non-axisymmetric flow and a decrease in pressure generation. As the machine enters stall, disturbances in the flow known as stall cells develop in the blade passages and rotate around the annulus. These rotating stall cells lead to a reduction in the thermodynamic efficiency of the compressor or fan.

Rotating stall can also lead to another phenomenon known as surge. During surge the pressure across the compressor or fan rapidly fluctuates, causing flow reversal and exposing the machine to large material stresses. If allowed to continue uninhibited these stresses can damage or destroy the machine.

The performance of an axial compressor or fan can be visualized for a variety of operating conditions on a performance map, as shown in Figure 1.5. The total pressure ratio (or fan static pressure) is plotted as a function of flow rate for each rotor speed; these curves are known as speed lines or characteristics. As the flow rate is decreased, the characteristics terminate at the stalling flow rate. The locus of stall points forms the “stall” or “surge line,” whereas the locus of operating points forms

the “working line.” The difference between these two lines is referred to as the stall or surge margin and can be thought of as a sort of safety factor for the machine.

The goal of compressor and fan design, then, is to maximize the pressure rise or efficiency while maintaining an acceptable margin of safety. Plasma actuators are an attractive modification that can be made to existing designs because of the advantages mentioned previously. Thus, the objective of this work is to investigate the use of pulsed-DC DBD plasma actuators for the purpose of controlling rotating stall in axial compressors and fans.

1.3 Rotating Stall Inception and Control

There are two routes that lead to rotating stall in compressors: modal stall inception (which is characterized by long length scale disturbances) and spike stall inception (which is characterized by short length scale disturbances). In each case the compressor stalls at a different point on the compressor performance map. Plotting the total-to-static pressure ratio as a function of mass flow, the stall point has a zero slope for modal stall and a negative slope for spike stall. This work has focused on preventing spike stall inception, since many compressors stall at a negative slope before reaching the peak total-to-static pressure rise.

Vo et al. [43] identified two criteria for spike stall inception. In the first case, the interface between the approach flow and the tip jet moves upstream of the rotor leading edge, and the tip clearance fluid spills over into the next blade passage. In the second case, the tip jet reverses direction at the trailing edge and impinges on the pressure surface of the adjacent blade. These two criteria are illustrated in Figure 1.6. As both criteria are necessary for the onset of tip blockage growth, they hypothesized that delaying either would also delay stall inception.

To achieve this delay in the onset of rotating stall, a number of passive and active approaches have been devised. One passive method of flow control popular

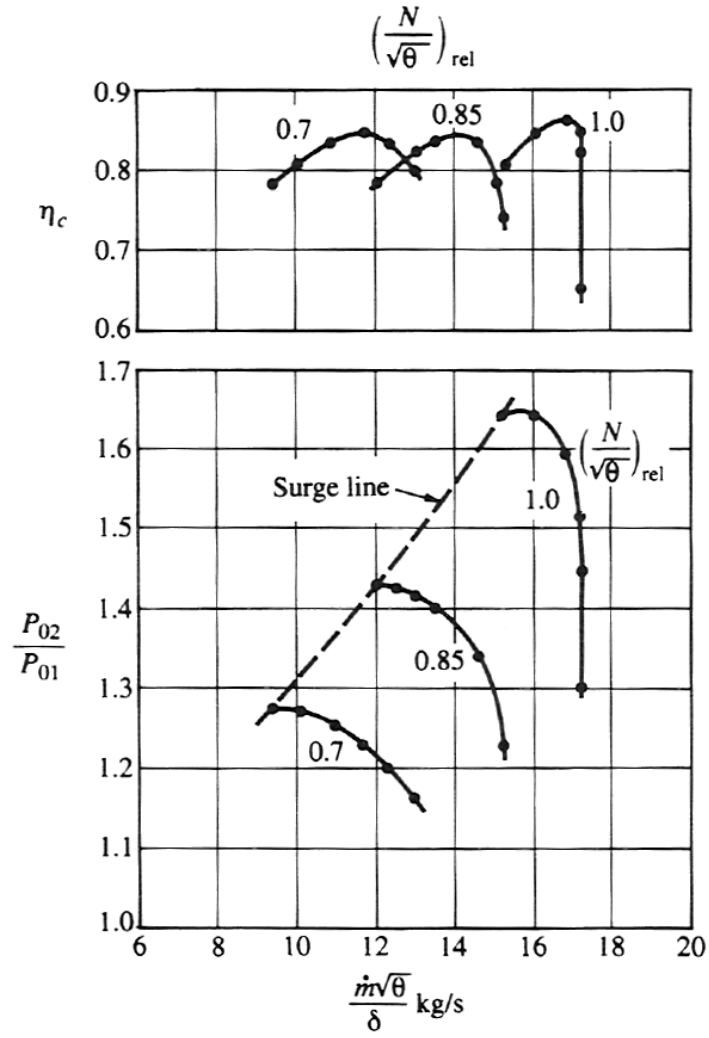


Figure 1.5. Example of a performance map for a transonic compressor stage (from Hill and Peterson [16])

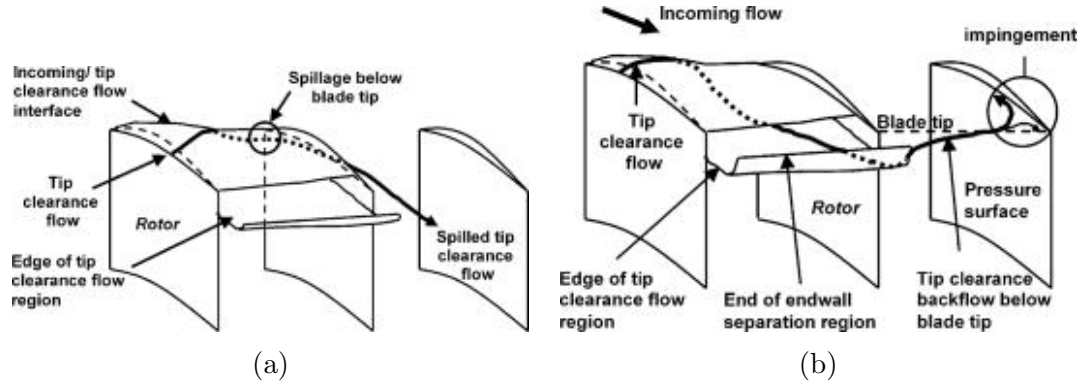


Figure 1.6. Criteria for spike stall inception; (a) tip clearance flow spillage at leading edge; (b) tip clearance flow reversal at trailing edge (from Vo et al. [43])

since the 1970s has been casing treatments, which can be divided into axial slots and circumferential grooves. In the axial slots treatment, the slots are machined into the casing parallel to the approach flow and perpendicular to the direction of blade rotation. These slots can be angled relative to the wall normal vector, in which case they are called axial skewed slots. Conversely, in the circumferential grooves treatment, one or more grooves are machined around the circumference of the rotor casing, perpendicular to the approach flow. The slots and grooves have been shown to extend stall margin by flow recirculation [10] which removes high loss fluid [35] and transports axial momentum radially [34].

Fujita and Takata [14] tested a series of configurations of circumferential grooves and axial slots, measuring the stall margin improvement and change in efficiency due to each one. Notably, they found that the stall margin improvement and compressor efficiency are inversely related, such that there is no one optimum geometry for these casing treatments. Houghton and Day [18] compared the performance of a single groove and multiple grooves at different axial locations, concluding that the efficiency loss is additive but the stall margin improvement is less than the sum from the component grooves. The stall margin was maximized when they located the groove

near the rotor leading edge or midchord. Ross [31] further studied the impact of casing grooves on the tip clearance flow field and surge margin extension, developing a model for the momentum balance as affected by the grooves. The advantages of circumferential groove casing treatments include their effectiveness and simple implementation. However, as a passive method the casing grooves cannot be adjusted or turned on and off, and so they cause a loss in efficiency even when they are not being used for stall margin extension [10, 14, 18].

Active methods of flow control which utilize a feedback loop to manipulate the response have also been attempted. Paduano et al. [29] implemented fast-response, variable-stagger inlet guide vanes (IGVs) in a low-speed axial compressor and successfully controlled modal disturbances to increase the stall margin. Meanwhile, Day [9] used fast-acting air jets along the circumference of the compressor to achieve the same thing. Wiegl et al. [45] also used unsteady air injection to damp pre-stall perturbations, this time in a transonic single-stage axial compressor. Unfortunately, these methods only addressed modal stall inception, as the mechanisms responsible for spike stall inception were still not well-understood at the time. Furthermore, adjustable IGVs and air injectors tend to require complicated arrangements and are limited by their bandwidth, and research investigating these methods of active control has essentially halted [10].

In this work, the pulsed-DC actuator is considered as a means of delaying leading edge tip clearance flow spillage by injecting momentum into the approach flow. (Theoretically, such a device could also be used at the trailing edge to prevent tip clearance flow reversal.) Although this represents the first time pulsed-DC DBDs have been studied experimentally for stall control in a compressor/fan, the use of AC DBDs in compressors has been examined before. Vo et al. [40–42] presented several computational assessments of casing plasma actuation for suppressing both spike and modal stall inception in low- and high-speed compressors. Wadia et al. [44] also used

CFD to analyze the effect of plasma actuators on tip clearance flows in subsonic and transonic compressor rotors. In each case the researchers found that the plasma actuation was effective at delaying spike stall inception but noted the need for induced body forces an order of magnitude higher than that provided by traditional plasma actuators. Li et al. [22] carried out experiments on a low-speed axial compressor with unsteady plasma actuation which was meant to excite turbulent structures in the casing boundary layer and transfer momentum from the outer region where velocities were higher. Using this approach, they achieved a stall margin improvement of up to 2.2%. However, they did not exceed a rotor speed of 2400 rpm, and the stall margin improvement decreased with increasing rotor speeds.

1.4 Objectives

The previous section discussed the motivation behind installing and operating pulsed-DC plasma actuators in axial compressors and fans. In order to accomplish that objective, however, several steps must be completed along the way. The research objectives are as follows:

1. To identify the relevant parameters and their effects for modifying and optimizing the thrust generation of the pulsed-DC plasma actuator
2. To develop a model for predicting the stall margin extension (SME) due to pulsed-DC casing plasma actuation in an axial compressor or fan
3. To validate the SME model by examining the actuation's effect on rotating stall cells and the speed characteristics

First, because the pulsed-DC waveform is a new means of powering plasma actuators, it is necessary to define what the parameters of interest are and then characterize what effects changing them has on the actuator performance. The approach of Enloe et al. [11, 12] and Thomas et al. [37] whereby a digital scale is used to measure the induced thrust is one method of accomplishing this, although a clearer picture of the

pulsed-DC physics and operation can be gained by employing additional experimental methods. This work is covered in Chapter 2.

Chapter 3 discusses a method of modeling the interaction between the approach flow and the tip clearance flow. The model from Ross [31] is modified to predict the effect of casing plasma actuation on the location of this interface and consequently SME.

Chapter 4 focuses on the original work that was planned for the Notre Dame Transonic Axial Compressor (ND-TAC) facility. These experiments entailed the manufacture of a specialized survey ring for housing the pulsed-DC plasma actuators which were to encircle the compressor rotor. Due to a number of difficulties, the ND-TAC experimental setup was set aside in favor of one built around a nonconductive fan. These difficulties and the insights gained from attempted solutions are discussed in this chapter.

Chapter 5 describes the nonconductive fan facility which was designed to replace the ND-TAC experimental setup. The tests carried out in this facility to determine the feasibility of pulsed-DC actuation for stall control are also included in this chapter. The test results can be split into two categories: microphone measurements (for examining stall cell magnitude and correlation) and fan curve measurements (for examining overall fan performance).

Finally, Chapter 6 gives an overall summary of the content in this dissertation as well as recommendations for future work. Descriptions of the actuator constructions used for testing and the corresponding naming conventions are included in Appendix A, while the MATLAB codes employed for data processing are reproduced in Appendix B.

CHAPTER 2

CHARACTERIZATION OF THE PULSED-DC PLASMA ACTUATOR

In order to optimize the pulsed-DC plasma actuator for engineering applications, it is first necessary to identify the relevant characteristics that dictate its performance. This chapter covers experiments undertaken to characterize the induced thrust and velocity profiles produced by the pulsed-DC plasma. The experimental setups and results for each experiment are discussed.

2.1 Thrust Measurements

First, a series of experiments were conducted to determine how the thrust generation of the pulsed-DC plasma actuator is affected by various parameters. These included choice of dielectric material, rise time of the waveform, pulse amplitude, and static pressure. By measuring the thrust as each parameter was individually varied, the relationships between them and the induced thrust were established. These are detailed in the following sections.

2.1.1 Experimental Setup

For the pulsed-DC plasma experiments, the stacked MOSFET switch designed and built by Creare for the Phase I NASA SBIR program was replicated. This switch was connected to the actuator circuit as illustrated in Figure 1.1a. A photograph of the assembled switching circuit is shown in Figure 2.1. Also visible in the photograph are an inductive current sensor (Pearson Model 2100) seen as the thick ring in the

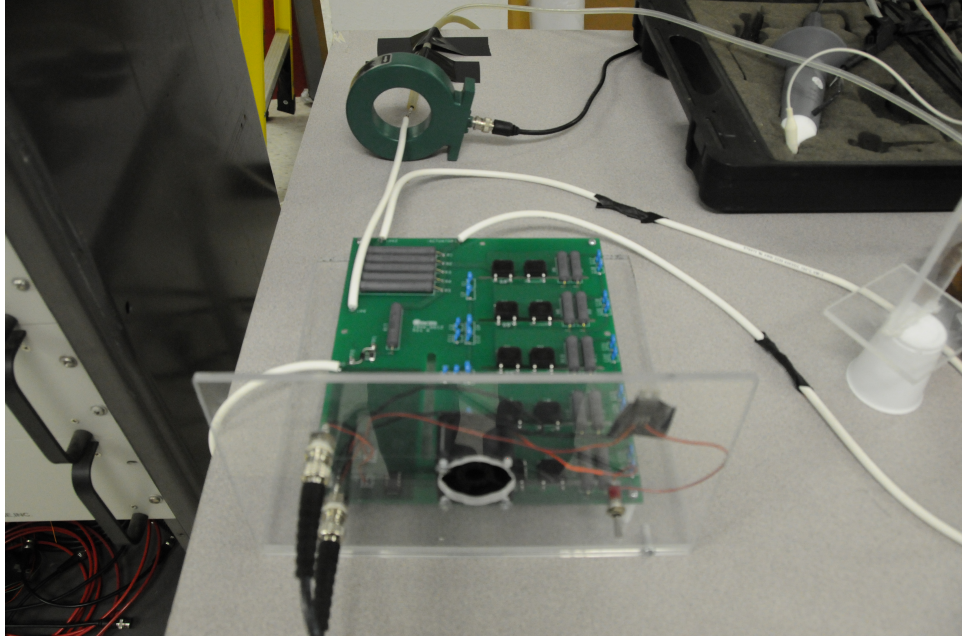


Figure 2.1. Pulsed-DC plasma actuator power system based on Phase I circuit

background and a high voltage probe (LeCroy PPE 20 kV). These were used to record current and voltage time series supplied to the actuator. The time series were then analyzed to correlate their effect on the thrust performance of the actuator. The high-voltage DC power supply used for these experiments was a Glassman PS/PH050R60-X18 with a maximum voltage rating of 50 kV and a maximum current limit of 60 mA.

The thrust generated by the plasma actuator was measured by mounting the actuator on an Acculab ALC-320.3 electronic force-measuring scale with a resolution of 1 mg. A photograph of the electronic force scale with the plasma actuator is shown in Figure 2.2. The electronic force scale was shielded from electromagnetic interference (EMI) by a covering of copper foil. To further minimize the effect of EMI generated by the plasma actuator operation, the actuator was suspended above the force-measuring platform by a balsa wood stand. Balsa wood was chosen as a neutral material in order to minimize charge buildup and electrostatic interactions between

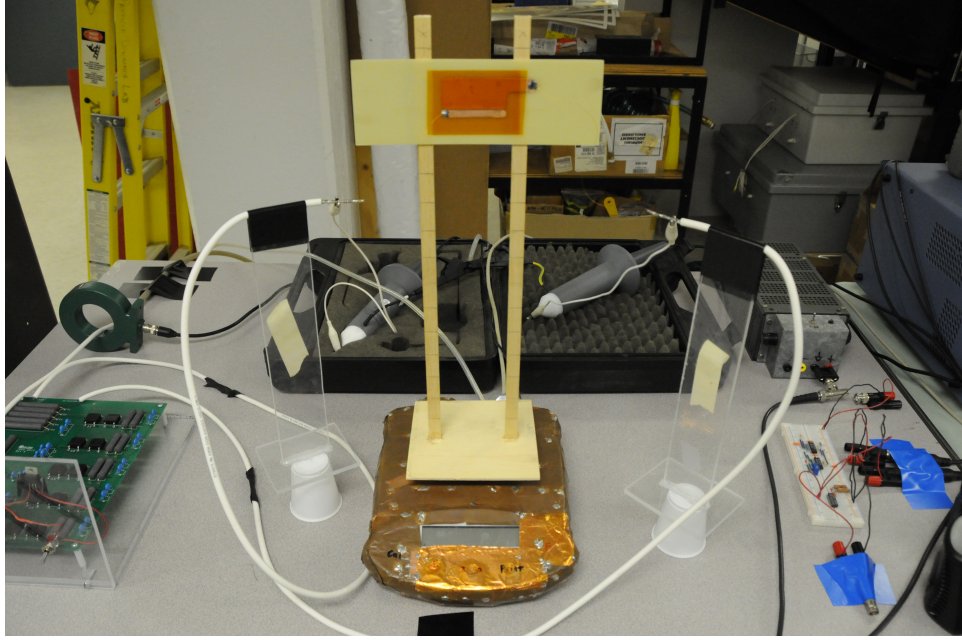


Figure 2.2. Photograph of electronic force-measuring scale and plasma actuator arrangement used for thrust measurements

the stand and scale. For this same reason, the metal weighing pan supplied with the scale was not used during experiments; instead, the stand was placed directly on the pan support. The distance of the actuator from the electronic force scale (12 in) was determined in separate experiments to be beyond that where any EMI generated by the actuator had any influence on the scale reading. The wire connections to the actuator were fine gauge coated copper wire. These are nearly invisible in the image but run between the clips at the ends of the white leads and the copper electrodes on the plasma actuator.

A schematic illustration of the complete experimental setup for the plasma actuator thrust measurements is shown in Figure 2.3. This includes at the right side of the figure an Agilent 33220A variable frequency waveform generator and a four-channel LeCroy WaveRunner 6050A digital oscilloscope. The waveform generator produced a narrow trigger pulse with a 5 V amplitude, 2.5 V offset, 1% duty cycle, and 5 ns

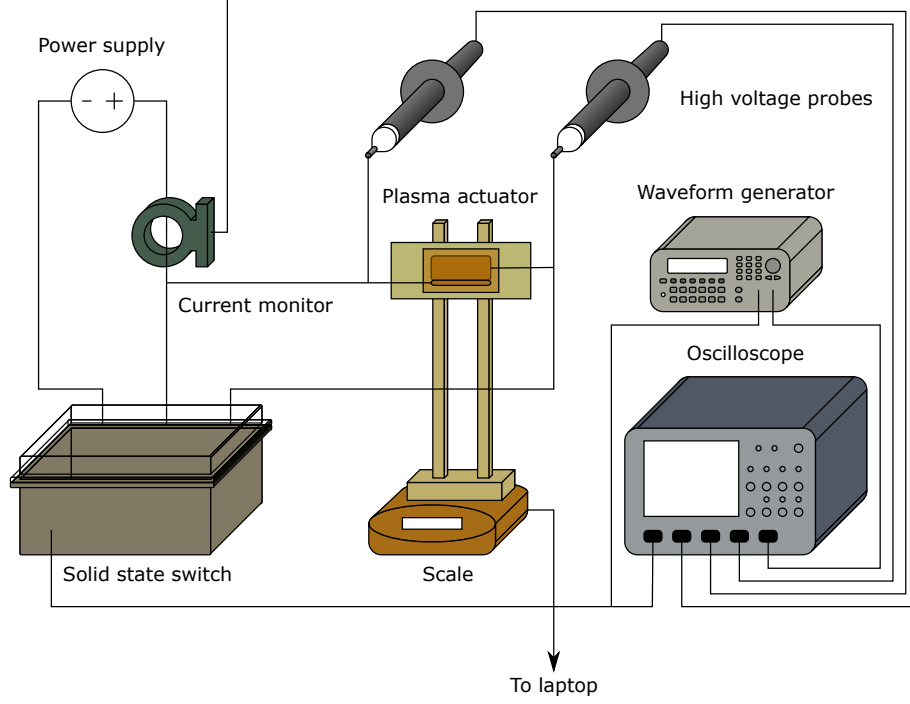


Figure 2.3. Schematic illustration of the total experimental setup used for thrust measurements

edge time that was supplied to the stacked MOSFET fast-acting solid-state switch. The current and voltage time series to the plasma actuator were acquired and stored to a USB flash drive by the oscilloscope. These were then transferred to a laptop computer where they were archived and post-processed.

An example of the simultaneously-captured voltage and current time series is shown in Figure 2.4. This corresponds to a supply voltage of 7 kV and an actuation frequency of 1 kHz for a 5-in-long actuator. The top plot shows the trigger signal supplied by the function generator, while the middle plot shows two simultaneous voltage time traces. The trace with the sharp downward peaks is measured at the drain of the highest power MOSFET in the stack of the solid-state switch and corresponds to the voltage time series that is supplied to the covered electrode of the plasma actuator. The other, relatively flat, voltage time trace corresponds to the DC

voltage that is supplied to the exposed electrode of the plasma actuator. Lastly, the bottom plot in Figure 2.4 shows the time series of the current being supplied to the switch and actuator by the high-voltage supply.

2.1.2 Comparison to AC Plasma Actuator

Experiments were performed to document the induced thrust produced by a DBD plasma actuator mounted on a force-measuring scale in the manner shown in Figure 2.3. For this, the plasma actuator consisted of electrodes that were 5 in long. The dielectric layer consisted of two 2-mil-thick layers of Kapton film. The actuator was operated either with an AC input as shown in Figure 1.1 or with a pulsed-DC input as shown in Figure 1.4. The two approaches were categorized in terms of the amount of induced thrust they produced. The results are shown in Figure 2.5. For the AC operation, the voltage scale is peak-to-peak voltage. For the pulsed-DC operation, it is the DC supply voltage. During the experiments, the temperature and humidity in the lab were monitored. These were respectively 21.7°C and 54% relative humidity.

The AC plasma actuator thrust displays the characteristic power law relation, namely, $F'_p \sim V^{3.5}$. In contrast, the pulsed-DC-generated thrust is linear with the input DC voltage. Most notably, the thrust generated by the pulsed-DC operation is more than an order of magnitude larger than that produced by the AC operation. In fact, the pulsed-DC thrust levels in Figure 2.5 are larger than the largest thrust levels documented with AC plasma actuators, which occurred at voltages that were ten times as high [37].

2.1.3 Effect of Dielectric Material

Although a Kapton dielectric was used in the previous thrust measurements, it generally is not suitable for experiments that operate for long periods of time, since it is degraded by the O_3 generated by the plasma. Another dielectric material that has

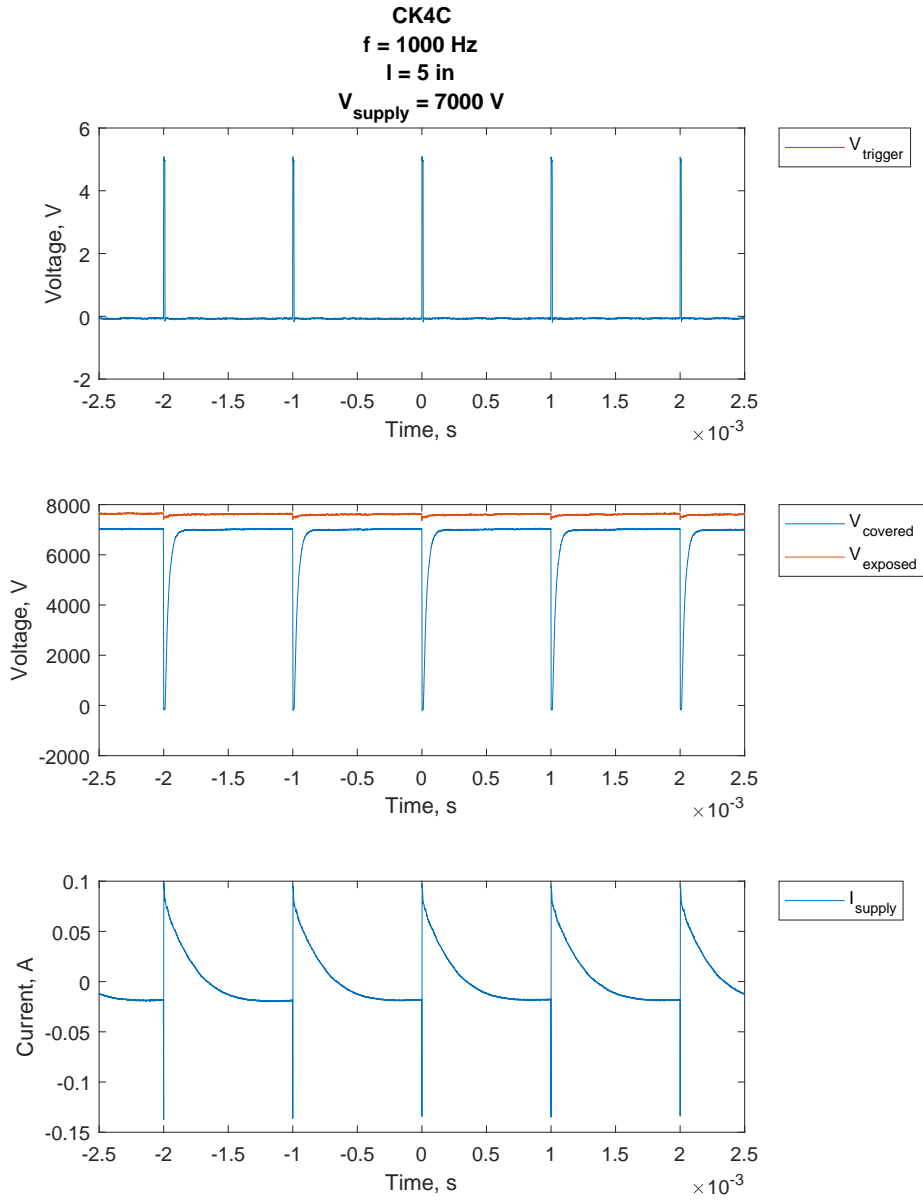


Figure 2.4. Time series for a DC input voltage of 7 kV and an actuation frequency of 1 kHz for a 5-in-long actuator; (top) voltage time series supplied by the function generator; (middle) voltage time series supplied to the covered and exposed electrodes of the plasma actuator; (bottom) corresponding current time series

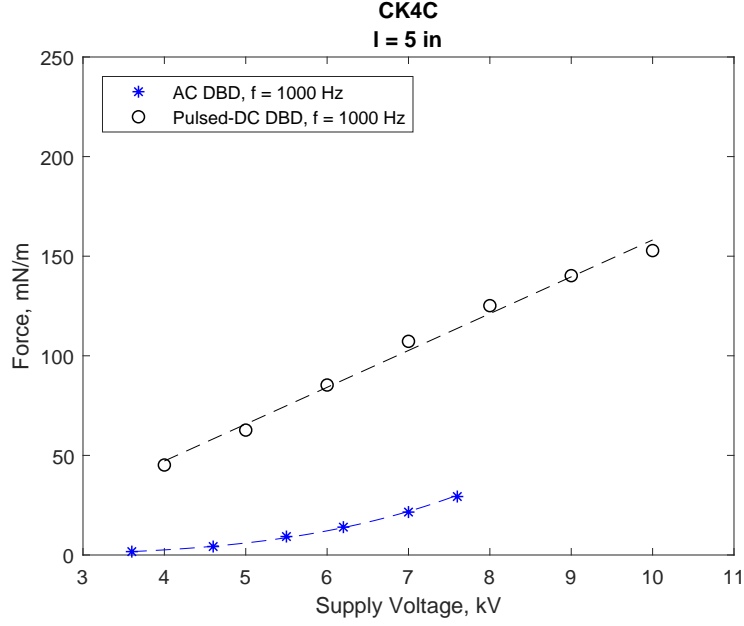


Figure 2.5. Comparison between the induced thrust from AC and pulsed-DC plasma actuators

been used is Ultem film, which is a polyetherimide (PEI) that is more resistant to O_3 . The dielectric strength of Ultem film is lower than that of Kapton film; however, this is not a critical issue with the lower voltages of the pulsed-DC operation. Therefore, experiments were performed to compare the thrust generated with the Ultem film dielectric to that with the Kapton film. The thickness of the Ultem film used in these experiments was 3 mil.

The thrust comparison between the Ultem and Kapton dielectric materials with 2.5-in-long actuators is shown in Figure 2.6. Two pulsed-DC frequencies of 500 Hz and 1 kHz are presented. In general, the thrust produced with the Ultem dielectric is less than that with the Kapton at lower voltages. The change in the thrust with voltage is however higher with the Ultem, so that at higher voltages, the thrusts produced with the two different dielectric materials are comparable.

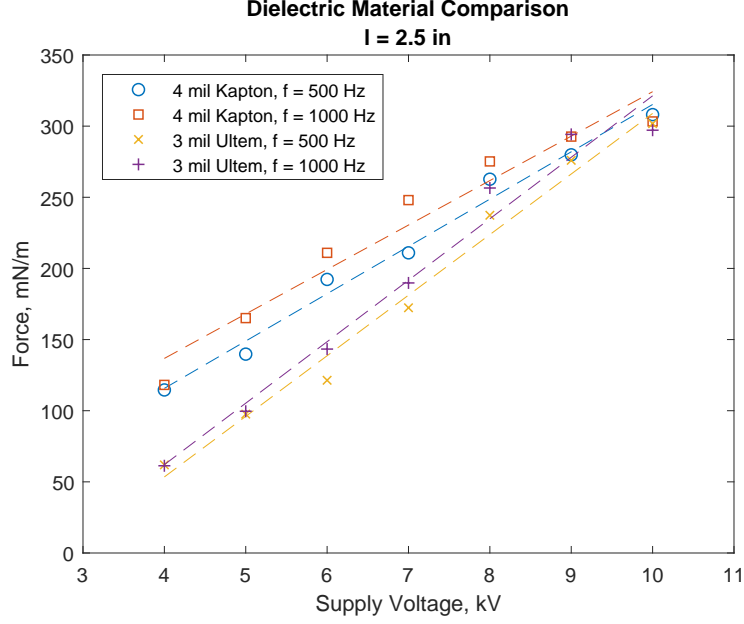


Figure 2.6. Comparison between the induced thrust using Kapton and Ultem dielectric layers

2.1.4 Effect of Rise Time

The RC time constant of the MOSFET switch can be adjusted by changing the value of R_{bias} or the actuator capacitance. This affects the time it takes for the covered electrode voltage to recover to the supply voltage as shown in Figure 2.7; increasing R_{bias} causes the rise time of the voltage waveform to increase.

Figure 2.8 shows the thrust comparison for a 2.5-in-long actuator using a bias resistance of $0.2 \text{ M}\Omega$ and $1 \text{ M}\Omega$. The thrust is higher for the lower value of R_{bias} (and faster rise time).

2.1.5 Effect of Pulse Amplitude

One of the most important parameters in the consideration of thrust generation is the pulse amplitude. In addition to being controlled by the supply voltage, the pulse amplitude can also vary depending on whether the stacked MOSFET switch is

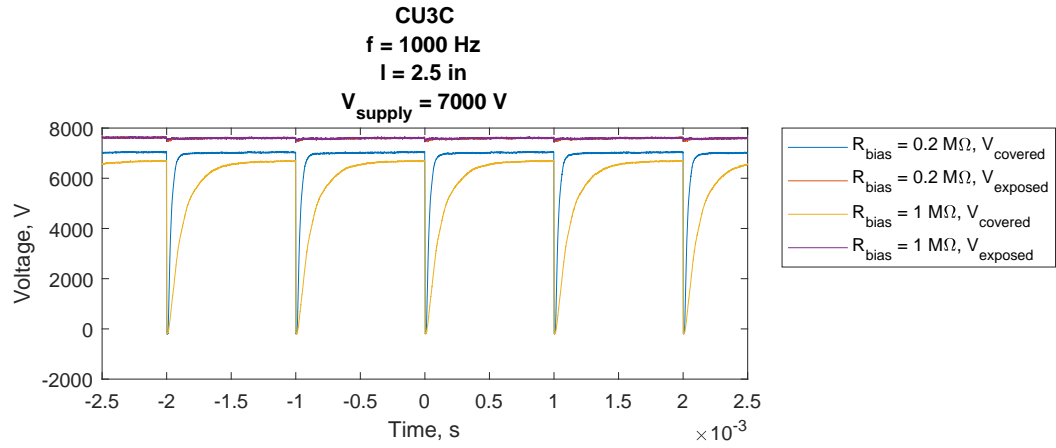


Figure 2.7. Comparison between time series using $R_{\text{bias}} = 0.2 \text{ M}\Omega$ and $R_{\text{bias}} = 1 \text{ M}\Omega$

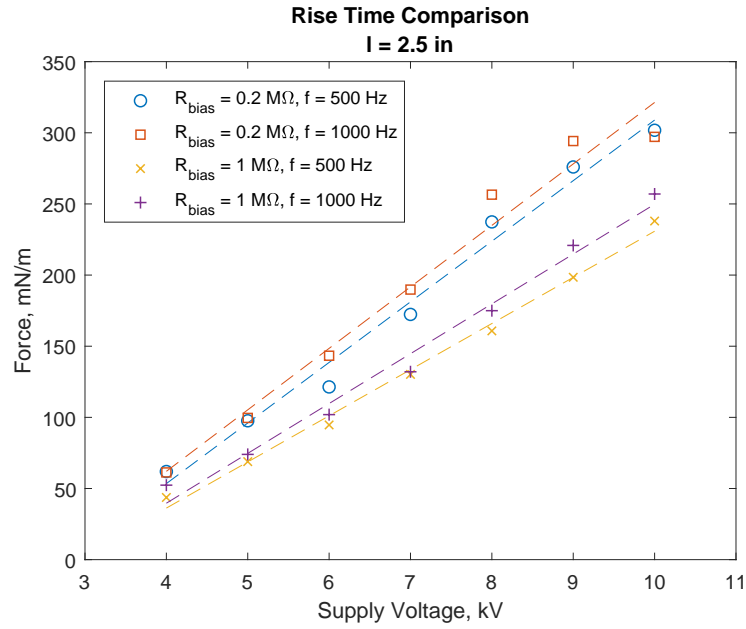


Figure 2.8. Comparison between the induced thrust using $R_{\text{bias}} = 0.2 \text{ M}\Omega$ and $R_{\text{bias}} = 1 \text{ M}\Omega$

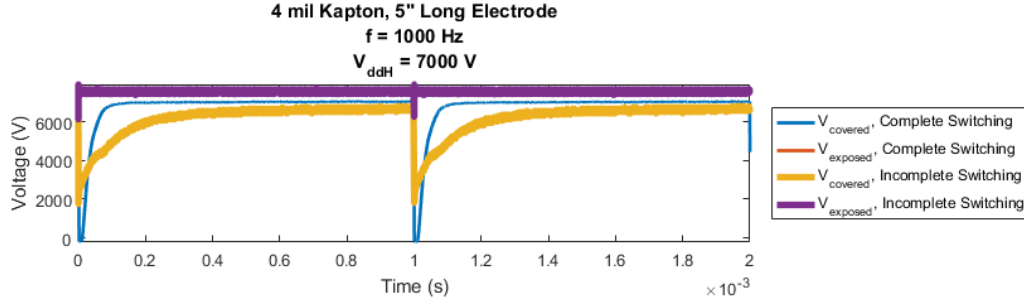


Figure 2.9. Comparison between time series with complete and incomplete switching

switching the covered electrode to ground correctly. For example, if one or more of the MOSFETs in the stack are damaged, the covered electrode voltage may not be pulled all the way to ground, reducing the pulse amplitude. Voltage waveforms for a complete switching case and an incomplete switching case are compared in Figure 2.9.

As can be seen in Figure 2.10, incomplete switching results in significantly lower thrust generation by the actuator. This is likely a result of weaker ionization, as the ionization is related to the change in voltage over time.

2.1.6 Effect of Static Pressure

Experiments were also performed to examine the effect of static pressure on the thrust produced by the pulsed-DC plasma actuator. The experiments followed the approach used by Valerioti and Corke [38] and consisted of placing the thrust-measuring setup shown in Figure 2.2 inside of a pressure chamber. The pressure chamber used for these experiments was a cylindrical steel vessel 24 in long and 16 in in diameter. It is capable of holding up to 350 psi of pressure and has feedthroughs for two high-voltage cables as well as various low-voltage cables. To pressurize the chamber, it was connected to a compressed air line available in the lab. This air line was capable of pressurizing the chamber up to 100 psig. The pressure was read off a dial indicator

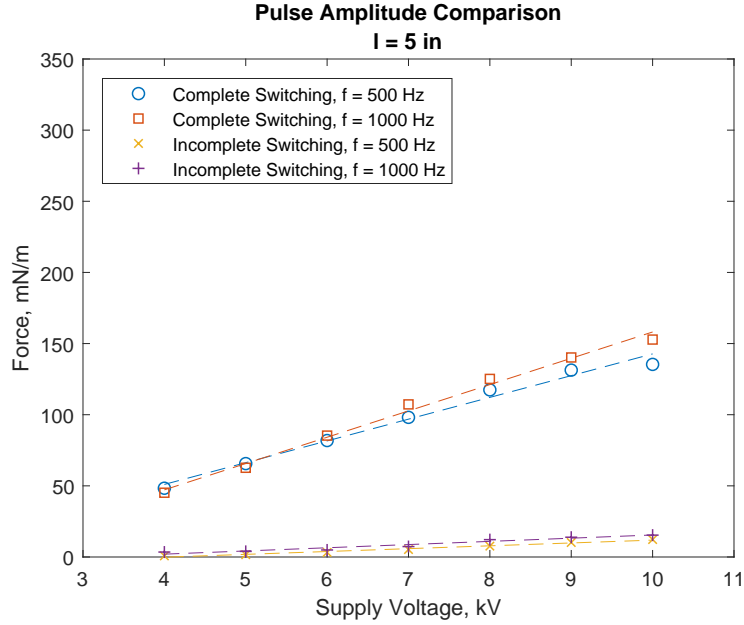


Figure 2.10. Comparison between the induced thrust with complete and incomplete switching

located on the side of the chamber as well as another one located on the air line regulator. Figure 2.11 shows photographs of the exterior and interior of the pressure vessel, with the plasma actuator mounted on the electronic force-measuring scale. The pressure vessel was sealed to prevent air leakage when pressurized. A viewing window built into the pressure vessel allowed for reading the force off of the scale display.

The actuator was powered at voltages ranging from 4 kV to 10 kV at pulse frequencies of 500 Hz and 1 kHz. Then, the static pressure in the chamber was increased from 0 psig (atmospheric pressure) to 100 psig in 20 psig increments. The temperature of the air inside the chamber was allowed to reach thermal equilibrium with the outside temperature in the laboratory before measurements were taken. This temperature was nominally 25 °C. The air in the chamber was frequently purged to minimize any effect due to buildup of ozone gas. In addition, repeatability checks

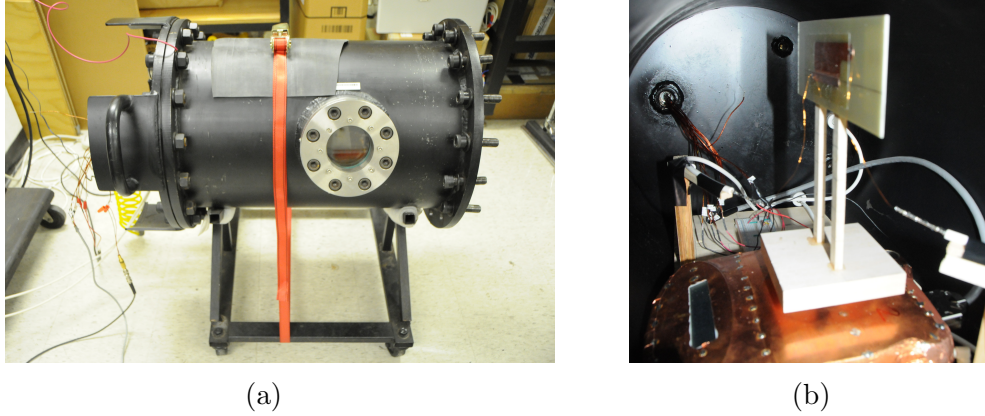


Figure 2.11. Photographs of the pressure vessel setup used for measuring the effect of static pressure on the pulsed-DC actuator thrust generation

were performed that included purging and re-pressurizing the air in the vessel. Because pressurizing the chamber caused the zero of the scale to change, the value on the scale display was recorded with plasma off for each test case, and the thrust was taken as the difference between this and the plasma-on value.

The results are shown in Figures 2.12 and 2.13. Figure 2.12 shows the change in the generated thrust as a function of the static pressure for different DC voltages. At any voltage, the thrust generally decreases with increasing static pressure until it reaches a minimum at approximately 80 psig (5.5 bar) and then begins to increase. This behavior is similar to that found by Valerioti and Corke [38] for the AC-powered plasma actuator, although the minimum thrust in that case was at a lower static pressure of 29 psig (2 bar).

The data in Figure 2.12 were replotted in Figure 2.13 to illustrate the change in the generated thrust as a function of the DC voltage for different static pressures. This illustrates that at any of the static pressures, the thrust varies linearly with DC voltage. The slope of the linear transfer function, dF'_p/dV_{supply} , for each of the static pressures is shown in Figure 2.14. This mimics the pressure dependence of the thrust at any of the voltage levels that was shown in Figure 2.12. This is somewhat

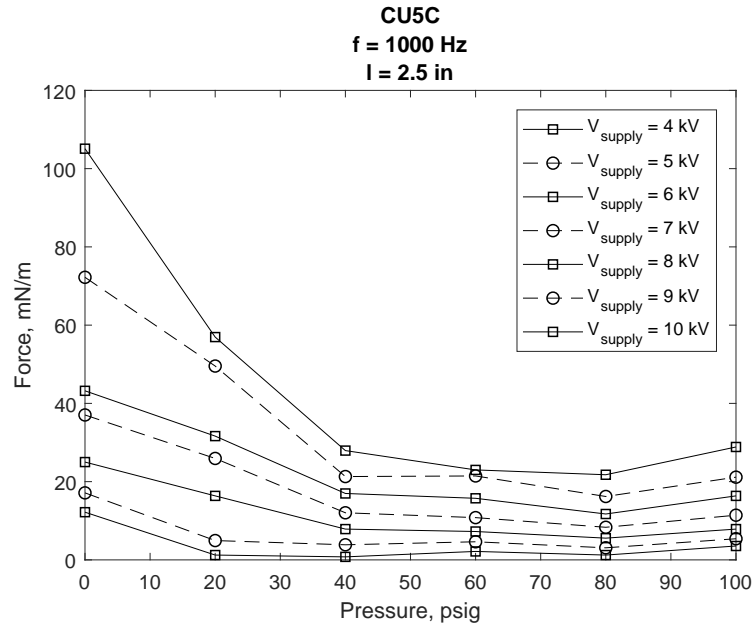


Figure 2.12. Effect of static pressure on the pulsed-DC actuator thrust for different DC voltages

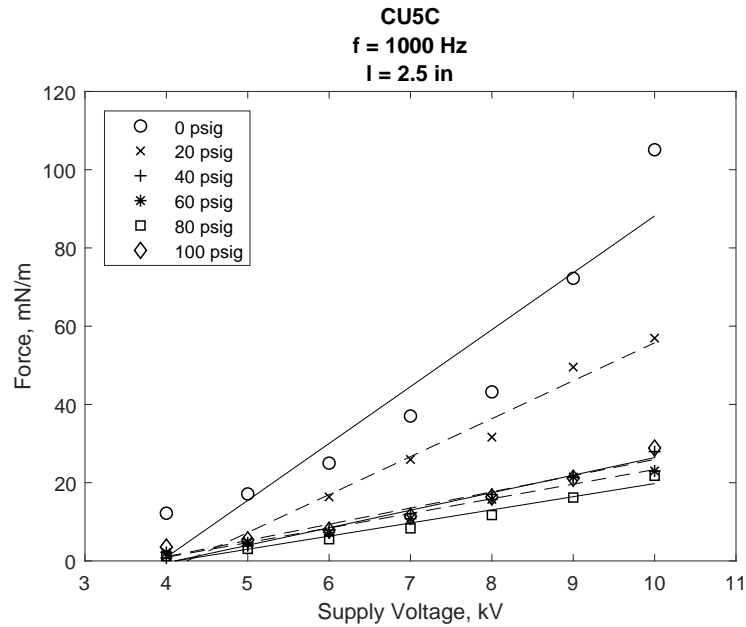


Figure 2.13. Effect of DC voltage on the pulsed-DC actuator thrust for different static pressures

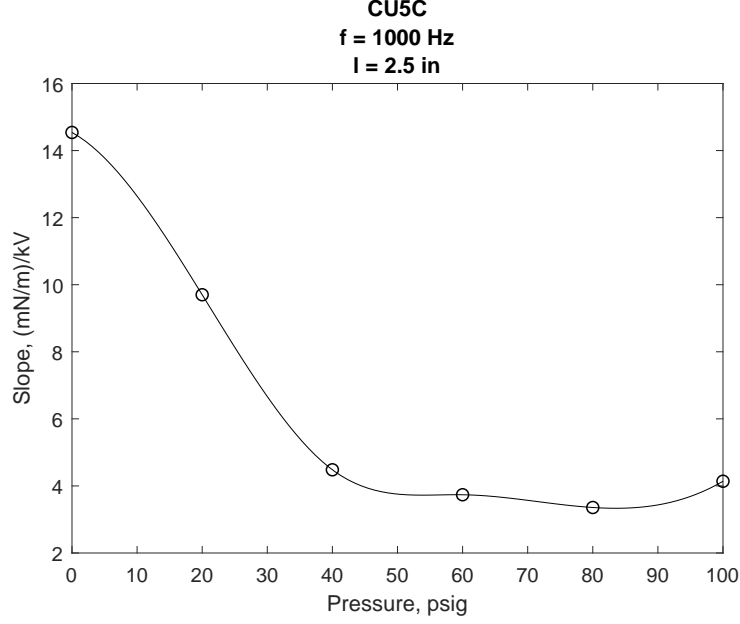


Figure 2.14. Effect of static pressure on the pulsed-DC actuator voltage-thrust transfer function, dF'_p/dV_{supply}

in contrast to the AC plasma actuator, where Valerioti and Corke [38] found that the exponent of the power-law relation between the generated thrust and voltage increased with increasing pressure even in the portion up to 2 bar pressure where the thrust was decreasing. The exponent eventually saturated for pressures above 6 bar. These fundamental differences between the AC and pulsed-DC plasma actuators need further investigation.

2.2 Velocity Profiles

To gain more understanding of the physics behind the pulsed-DC actuator, velocity profiles were obtained at several locations downstream of an actuator. This time, the actuator consisted of two 2.5-in-long electrodes separated by a 3-mil-thick Ultem dielectric on a 1/16-in-thick G-10/FR4 Garolite substrate. The exposed electrode was 1/16-in-wide aluminum tape, while the covered electrode was 1-in-wide copper tape.

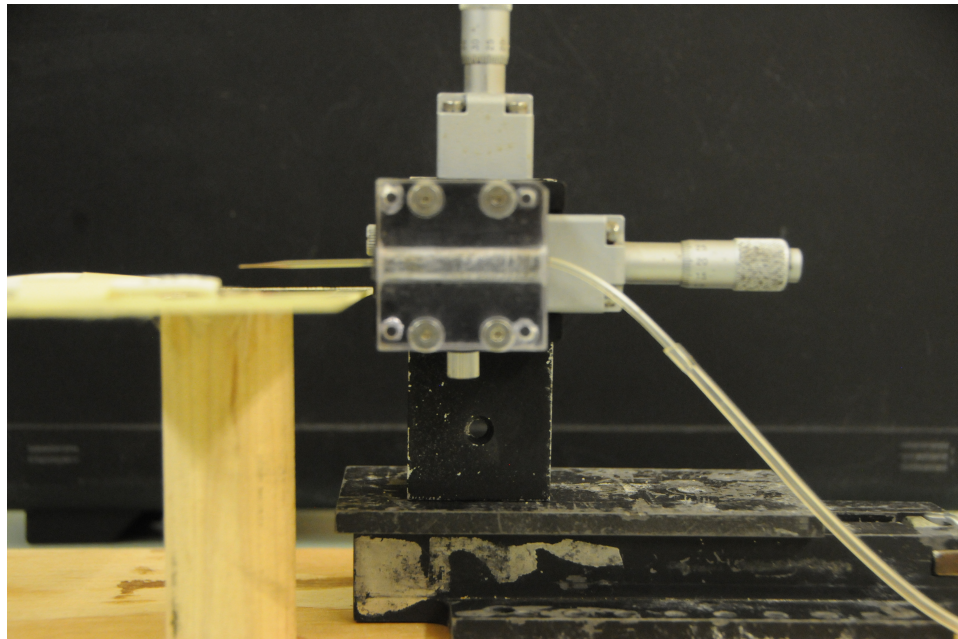
Because the actuator would arc to an ordinary metal pitot probe, a glass pitot probe was instead mounted on a hand-operated traverse. The pitot probe was connected to a Validyne DP103 differential pressure transducer with a -12 diaphragm. When run at 500 Hz and 10 kV, the actuator produced EMI which decreased the signal-to-noise ratio, so the transducer signal was passed through an active low-pass filter and then recorded on a computer. The noise was symmetric about the mean, so the data were averaged over 1 min. The experimental setup is shown in Figure 2.15.

The normalized velocity profiles at locations 4 mm, 8 mm, 16 mm, 20 mm, and 24 mm downstream of the actuator are shown in Figure 2.16. The highest maximum velocity of 0.64 m s^{-1} was found closest to the actuator, with peak velocities decreasing for profiles farther downstream.

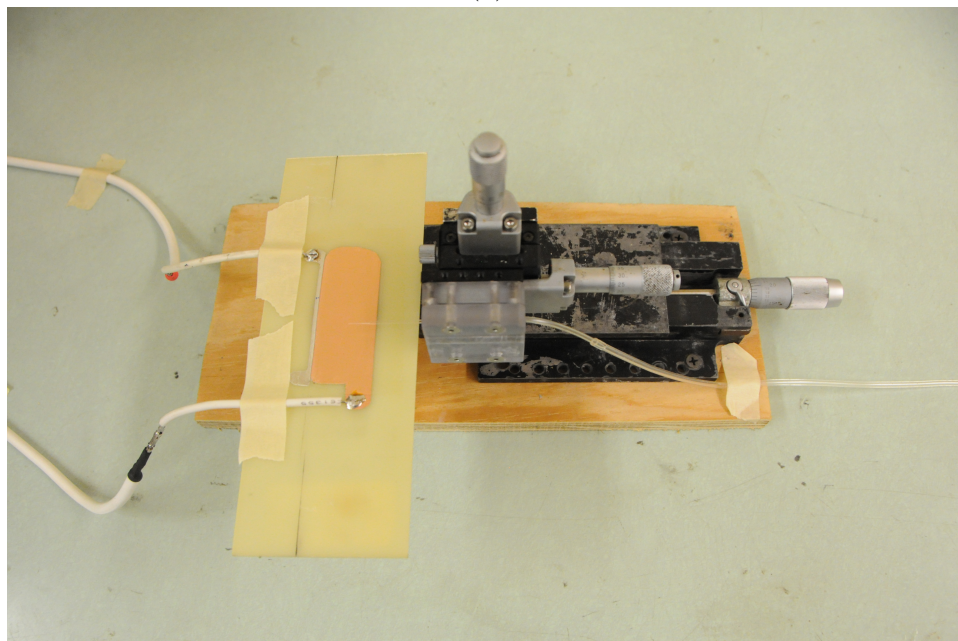
Once the velocity profiles were obtained, the force per unit length was estimated using Equation 2.1. This comes from a control volume analysis as described by Hoskinson et al. [17].

$$F'_p = \rho \int u^2 dy \quad (2.1)$$

The integrated forces are summarized in Table 2.1. These values are two to three orders of magnitude lower than those obtained with the digital balance. One major reason for this is that the peak induced velocity occurs over a very short period of time, so that the time-averaged velocity measured by the glass pitot probe is much lower. This is the basis for ongoing work by Sontag et al. [36], who measured the air pulse velocity using an isolated constant-current hot wire anemometer with a floating ground. They confirmed the existence of a large peak velocity corresponding to the time interval of the trigger pulse, recording a maximum velocity of 20 m s^{-1} for a pulsing frequency of 500 Hz and supply voltage of 10 kV.



(a)



(b)

Figure 2.15. Photographs of the experimental setup used for velocity profile measurements

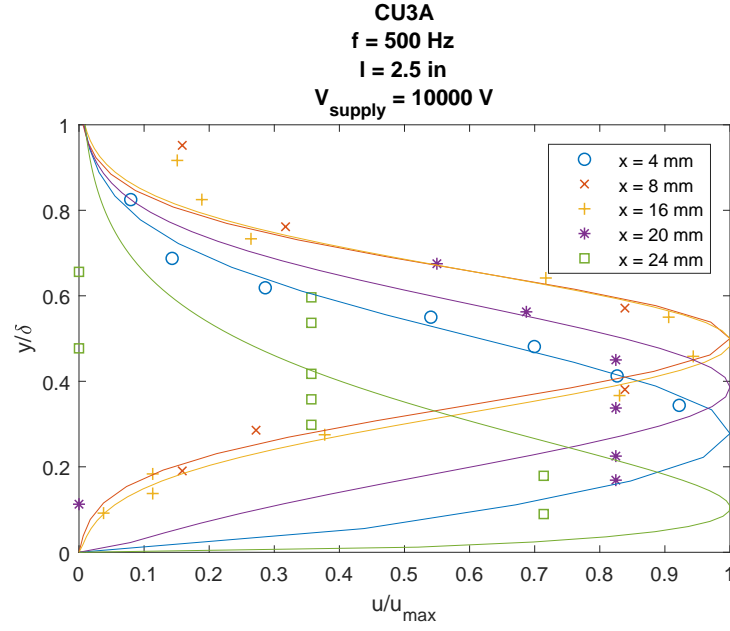


Figure 2.16. Normalized velocity profiles for different downstream locations

TABLE 2.1

INTEGRATED FORCES

x , mm	F'_p (Experimental Data), mN/m	F'_p (Skewed Gaussian Fit), mN/m
4	0.36	0.69
8	0.33	0.34
16	0.28	0.27
20	0.018	0.019
24	0.0044	0.0049

CHAPTER 3

MODEL FOR STALL MARGIN EXTENSION

Extensive experiments have been performed in the ND-TAC facility by Ross [31] to investigate the effects of circumferential groove casing treatments for stall control. Ross developed a functional relationship between the surge margin extension due to a casing treatment and the smooth wall tip clearance flow field. This considered a one-dimensional control volume that involved a balance between axial momentum in the tip leakage flow and the drag force produced by the casing grooves. This is embodied in the following relation

$$C_{d_{cv}} Q_0 \pi D (x_0 - x_{zs}) = n_r K_{A_c} \tilde{Q} \tau c_{ax} - F_g \quad (3.1)$$

in which $C_{d_{cv}}$ is the experimentally-determined drag coefficient for the control volume, Q_0 is the approach flow momentum per unit area, D is the compressor annulus outer diameter, x_0 is the virtual origin of the tip leakage jet, x_{zs} is the axial location of the line of zero axial shear, n_r is the blade count of the rotor, K_{A_c} is the actual-to-approximate tip leakage jet axial momentum ratio, \tilde{Q} is the momentum flux of the tip leakage flow per unit area, τ is the tip gap dimension, c_{ax} is the rotor blade axial chord, and F_g is the drag force produced by the casing grooves.

In this approach, the drag force produced by the casing grooves is substituted with the body force produced by the pulsed-DC plasma actuator. This is shown schematically in Figure 3.1. The schematic shows what is believed to be the optimum location of the plasma actuator, which is near the leading edge of the compressor blade row.

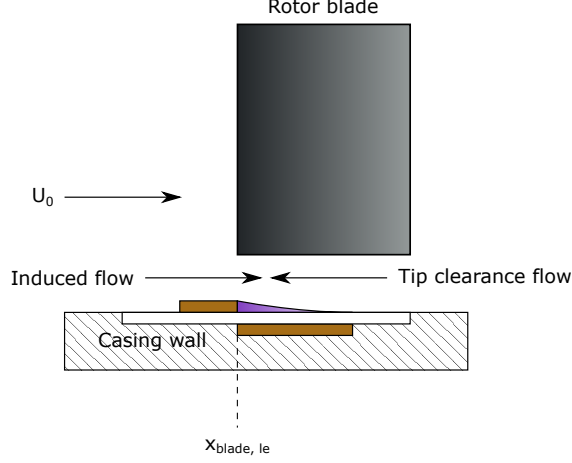


Figure 3.1. Schematic of 1-D momentum balance used in estimating effect of pulsed-DC plasma actuator on compressor stall margin

The choice of this location for the plasma actuator is based on Vo et al. [43] who suggested a criteria for spike stall inception in which reverse flow in the tip gap region moves forward (upstream) of the blade row leading edge, designated as $x_{blade, le}$ in Figure 3.1. The leading edge plasma actuation is therefore intended to resist the upstream motion of the reverse flow front. This alteration of the axial momentum balance is believed to be the mechanism by which casing grooves suppress stall, although the grooves do so indirectly through radial transport of axial momentum [31].

The upstream edge of the reverse flow on the casing wall that is caused by the tip leakage will be marked by a stagnation line where the wall shear stress is zero [33]. Its location is denoted as x_{zs} . Therefore Equation 3.1 can be rearranged to solve for x_{zs} , namely

$$\frac{x_{zs}}{c_{ax}} = \frac{x_0}{c_{ax}} - \frac{n_r}{\pi} \frac{K_{Ac}}{C_{dcv}} \frac{\tilde{Q}}{Q_0} \frac{\tau}{D} + \frac{1}{\pi} \frac{F_p}{C_{dcv} Q_0 c_{ax} D} \quad (3.2)$$

where F_p is the plasma actuator body force. Many of the quantities in Equation 3.2 such as x_0 , K_{Ac} , C_{dcv} , and \tilde{Q} came from Ross [31] for a smooth casing reference.

At stall, $x_{zs} = 0$; therefore, Equation 3.2 can be solved for Q_0 in terms of a known

compressor geometry and other constant values known from previous experiments. Having Q_0 allows the approach Mach number to be determined via manipulation of the mass flow function. Then, assuming isentropic flow, the approach flow static pressure P_1 can be found. Assuming the total-to-static pressure ratio across the compressor rotor, P_{0_2}/P_1 , remains constant and equal to its magnitude at the smooth wall stall point, the total pressure downstream of the rotor, P_{0_2} , is found by multiplying P_1 and P_{0_2}/P_1 . Thus the total pressure rise across the rotor at stall, π_{s_2} , is computed.

Again assuming isentropic flow, the approach flow static temperature T_1 is found based on the approach flow Mach number and total temperature. The approach flow density, ρ_1 , is then found using the ideal gas equation of state. Having ρ_1 and Q_0 , the approach flow velocity can be found. Finally, with the air density, approach flow velocity, and inflow cross-sectional area all known, the mass flow at stall, \dot{m}_{s_2} is determined.

Assuming the same design point performance as the smooth wall compressor, the stall margin extension is defined as the difference between the stall margin with the plasma actuator (subscript 2) and that with the smooth casing without the plasma actuator (subscript 1). This is given by Equation 3.3.

$$\text{SME} = \frac{\pi_d}{\dot{m}_d} \left(\frac{\dot{m}_{s_1}}{\pi_{s_1}} - \frac{\dot{m}_{s_2}}{\pi_{s_2}} \right) \quad (3.3)$$

A Mathematica script was generated to solve Equations 3.2 and 3.3 as well as perform the other ancillary calculations needed in their solution. Based on a plasma actuator body force of 300 mN m^{-1} , a stall margin extension of 3.4% was obtained for the ND-TAC facility.

This model can also be used to estimate (within an order of magnitude) the plasma force needed to obtain a given stall margin extension in the nonconductive fan facility. To start, c_{ax} , D , n_r , and τ are known for the facility. The values of x_0 and

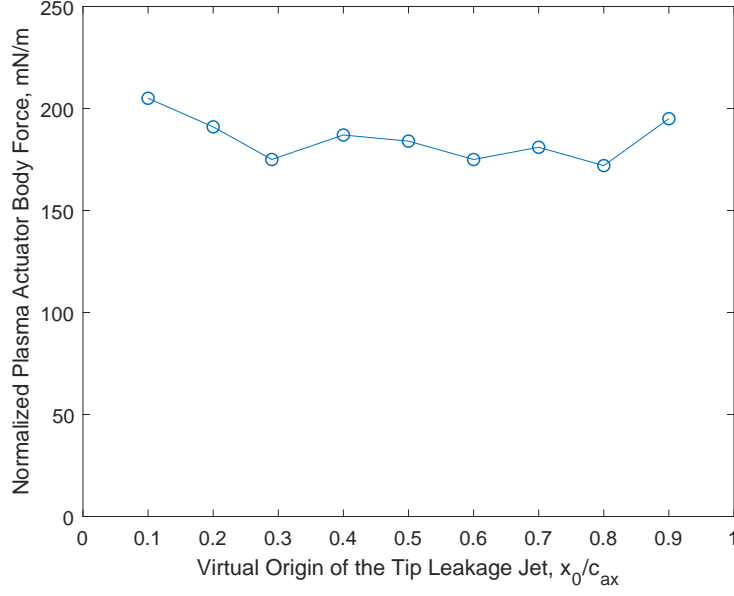


Figure 3.2. Effect of tip leakage jet origin on required plasma body force

C_{dcv} are assumed to be on the same order of magnitude as those for the compressor facility, so those are substituted into Equation 3.2 as well. Therefore, the unknowns are K_{Ac} and \tilde{Q} (which can be combined into one constant) and F_p . Assuming that Q_0 scales with the stall margin improvement and applying a least-squares fit to the data in Table 5.3, the corresponding plasma force can be determined. Figure 3.2 shows this force as a function of x_0 , and it is found to fall between the values from the scale measurements and the pitot probe measurements.

CHAPTER 4

PRELIMINARY WORK IN THE ND-TAC FACILITY

Originally, experiments had been planned in the Notre Dame Transonic Axial Compressor to demonstrate the pulsed-DC actuator's ability to suppress traveling stall cells and validate the model in Chapter 3. However, concerns over electric arcing and potential damage to the magnetic levitation bearings in the ND-TAC facility precluded the completion of these tests. Instead, the experiments were conducted in a different facility utilizing a nonconductive fan. Nonetheless, the design of the ND-TAC test casing and attempts to prevent arcing inside of it informed the designs and experimental methodology used later for the nonconductive fan facility.

4.1 ND-TAC Plasma Actuator Stall Control Design

The Notre Dame Transonic Axial Compressor is a 1.5-stage compressor that was designed to investigate a variety of flow control methods relating to compressor stall and surge. It is powered by a 400 hp variable-speed electric motor that is connected to the rotor through a gearbox which spins the rotor up to 17,000 rpm. With a 17.936-in-diameter rotor, the tip Mach number at the highest rpm is 1.2. The rotor spins on magnetic bearings that provide static and dynamic tip gap control. A cutaway schematic of the flow path design is shown in Figure 4.1.

A CAD rendering of the plasma actuator implementation for stall control in the ND-TAC facility is shown in Figure 4.2. The plasma actuator is located in a specially-designed survey ring that becomes part of the outer casing directly over the compressor rotor. The survey ring consists of one aluminum ring, one Ultem insert, and six

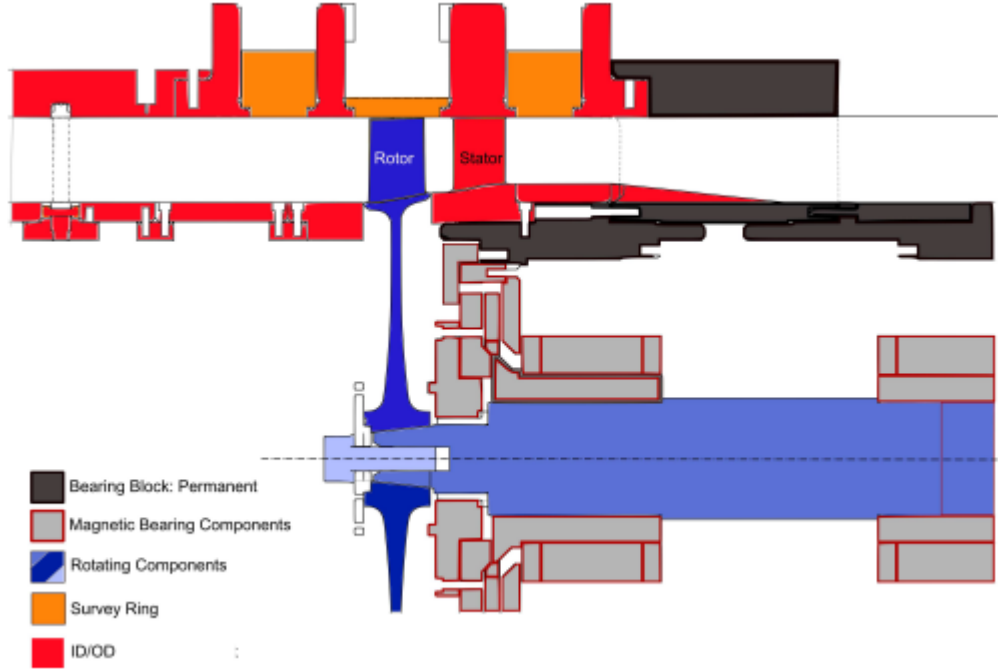


Figure 4.1. Cutaway drawing of the ND-TAC facility (from Ross[31])

Teflon plugs. The aluminum ring has an inside diameter of 18 in, giving a tip clearance gap of 32 mil (2.3% of axial chord). The Ultem insert has a recessed section in which the DBD plasma actuator is placed as well as a dovetail shape so that it interlocks with the aluminum ring. Except for the recessed section, the inner diameter of the Ultem insert is flush with the inner diameter of the aluminum ring. The six Teflon plugs are inserted into the aluminum ring. There are four plugs (one pair on either azimuthal side of the actuator) which each house a Kulite XTL-190-25A pressure transducer and two plugs which house the DBD electrode cables (the latter two are also inserted into the Ultem piece).

In its current implementation, the actuator assembly covers a 6 in (38.2°) arc segment of the ring. Of this, the plasma actuator length covers 5 in (31.8°). The Kulites are located at the leading edge of the blade row, 11.6° (1.82 in) from the edge of the actuator and 20° (3.14 in) from each other. The purpose of these pressure

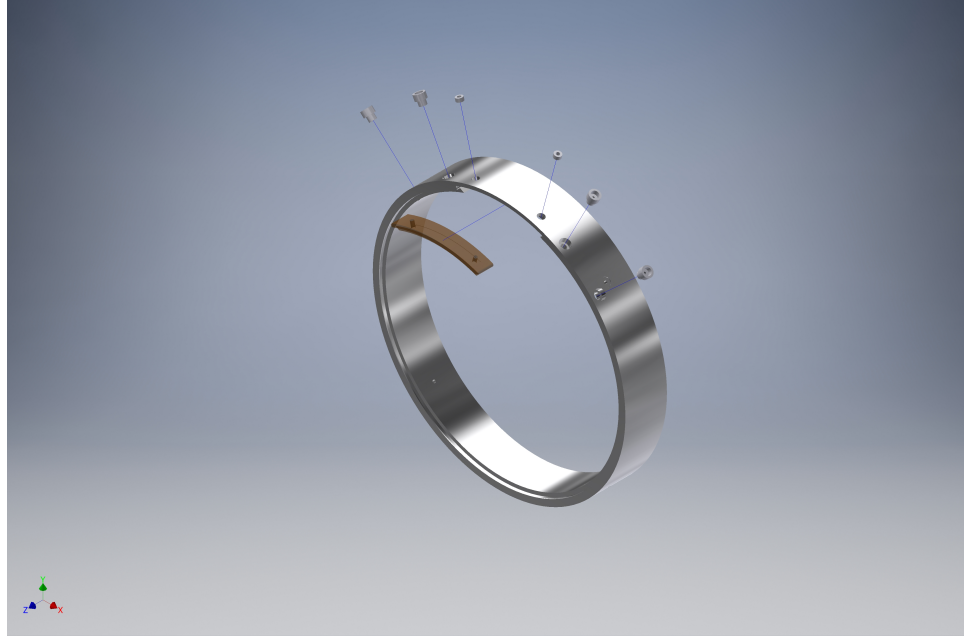


Figure 4.2. Schematic drawing showing assembly drawing of casing survey ring with inset plasma actuator

transducers is to detect the passage of traveling stall cells that are known to form prior to a fully-stalled condition.

The objective was to dynamically observe a suppression of the traveling stall cells as they convected past the plasma actuator. As the ND-TAC stalls via spike-type inception [4, 31], the compressor was to be throttled from the design operating point until stall occurred. At the same time, the Kulite signals would be acquired with a simultaneous once-per-revolution pulse to provide a temporal reference. This experiment would have been repeated with and without plasma actuation.

Following the demonstration of the ability to suppress traveling stall cells, seven additional arc segments of plasma actuators were to be added to cover the full azimuth of the survey ring. This ring would have been used to validate the predicted 3.4% stall margin extension. The compressor mass flow would be measured by a Venturi flow meter located near the outdoor inlet box. Meanwhile, the total pressure at the

compressor stage inlet and exit would be measured by Kiel probes located around the circumference of the compressor. These data would have been used to calculate the pressure ratio across the compressor, which would have been plotted against the mass flow to construct plasma-on and -off performance maps for the compressor. Although these measurements were unable to be performed in the ND-TAC facility, similar experiments described in Chapter 5 allowed the stall margin extension for the nonconductive fan to be determined.

4.2 Parylene Tests

The tip clearance height τ inside the compressor is 32 mil, but the thickness of the exposed electrode further reduces the distance between the actuator and the rotating blades. This presented a challenge because the dielectric strength of air is about 3.0 MV m^{-1} , meaning that if the exposed electrode were raised to a 10 kV potential, the separation would need to be greater than $(10 \text{ kV}) / (3.0 \text{ MV m}^{-1}) = (3.3 \text{ mm})$, or 130 mil to prevent arcing. To address this issue, one option that was considered was to coat the rotor blades in a material with a dielectric strength stronger than that of air.

The coating had to be able to withstand a maximum compressor temperature of 200 °F. It also had to be thin enough to fit in the remaining space without substantially affecting the flow in the tip gap region. After unsuccessfully testing coatings of boron nitride and Performix Liquid Tape, a sample of parylene C was requested. Parylene is a chemical vapor deposited polymer which has a number of advantages over spray coatings, including:

- A dielectric strength of 6900 V/mil
- Thermal stability up to 248 °F
- Conformal coating of all surfaces including sharp edges
- No pinholes

The samples consisted of aluminum coupons which were coated with 1 mil of parylene C. To ensure that a parylene coating would prevent arcing inside the compressor between the actuator and rotor blades, the samples were placed 20 mil above a flat plate mock-up of the plasma actuator and grounded to earth. The actuator was then powered to 10 kV. During this testing, no arcing was observed between the actuator and the aluminum coupons, even at the edges. Therefore, it was decided to test a parylene C coating on the rotor itself.

After the rotor was coated in a 48.33-micron- (1.903-mil-) thick layer of parylene, the previous test was repeated. This time, the plasma actuator was built into the survey ring, which was then placed around the rotor with the same spacing as it would have had for testing in the TAC facility. Unfortunately, discharges were observed between the exposed electrode and the tips of the rotor blades. It is believed that this was due to concentration of the electric field at the very sharp edges of the rotor blades. Whereas the aluminum coupons were essentially two flat plates, the electric field present in the vicinity of the rotor blades and curved survey ring was more complicated. A thicker coating of parylene could have provided more insulation, but it was decided to try grounding the exposed electrode to prevent arcing instead.

4.3 Effect of DC Offset

Due to the parylene's inability to adequately insulate the rotor, a negative-pulsing switch was developed which shifts the voltages of both actuator electrodes down so that the exposed electrode is always at ground while the covered electrode is pulled to a negative high voltage and rises to ground. Thus, there was no voltage potential between the exposed electrode and the rotor blades. The dielectric layer of the actuator acted as insulation between the high voltage covered electrode and the rotor blades. It was verified that no arcing occurred using this configuration; however, thrust measurements showed that the negative switch generated little to no

body force. In addition, although there was no voltage discharge to the grounded equipment, a layer of plasma still formed between the covered electrode and the rotor blades since the blades essentially acted as additional exposed electrodes. Since it was known that the positive switch, with the exposed electrode at a constant high voltage, produced more thrust, the effect of adding a DC offset was investigated. Ideally, the DC offset would be large enough to generate the needed thrust but not so large that arcing would occur.

4.3.1 Negative Switch

Since the negative switch by itself generated negligible body force, the exposed electrode was shifted from ground to both 10 kV and -10 kV to see the effect on thrust. This resulted in higher readings (although not high enough to match the maximum thrust recorded with the positive switch). In practice, however, the voltage applied to the exposed electrode would also have to be lower than the threshold for arcing to occur. Figures 4.3 and 4.4 show the voltage waveforms supplied to the covered and exposed electrodes for the 10 kV and -10 kV cases respectively.

4.3.2 Positive Switch

The positive switch generated more thrust than the negative switch, but having the exposed electrode at a constant high voltage increases the risk of arcing. Therefore, thrust measurements were taken with the exposed electrode grounded and compared to those from the standard configuration. Figure 4.5 shows the voltage waveforms supplied to the exposed and covered electrodes. Meanwhile, Figure 4.6 shows the force as a function of time. Not only is the peak thrust lower than the maximum value of $1.964 g_f$ which was recorded when the exposed electrode was powered, but the thrust also decreases over time. This may be because the positive ions which would normally be repelled by the exposed electrode now see an infinite source of

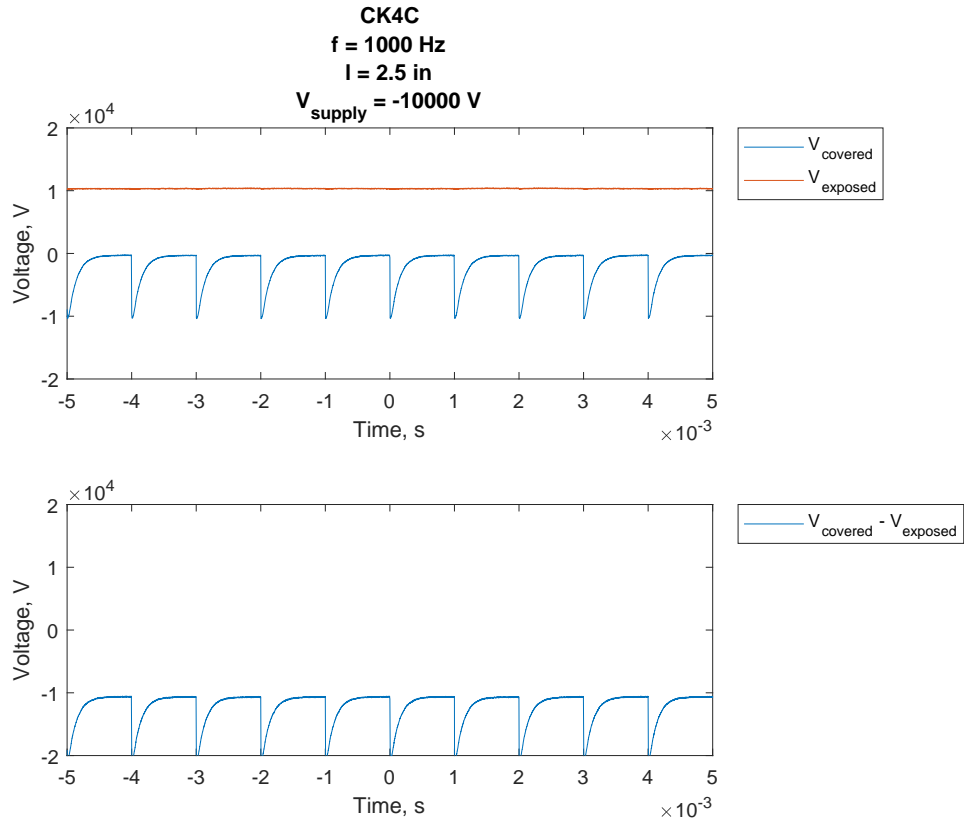


Figure 4.3. Voltage time series supplied by the negative switch to the covered and exposed electrodes of the plasma actuator. Exposed electrode held at 10 kV.

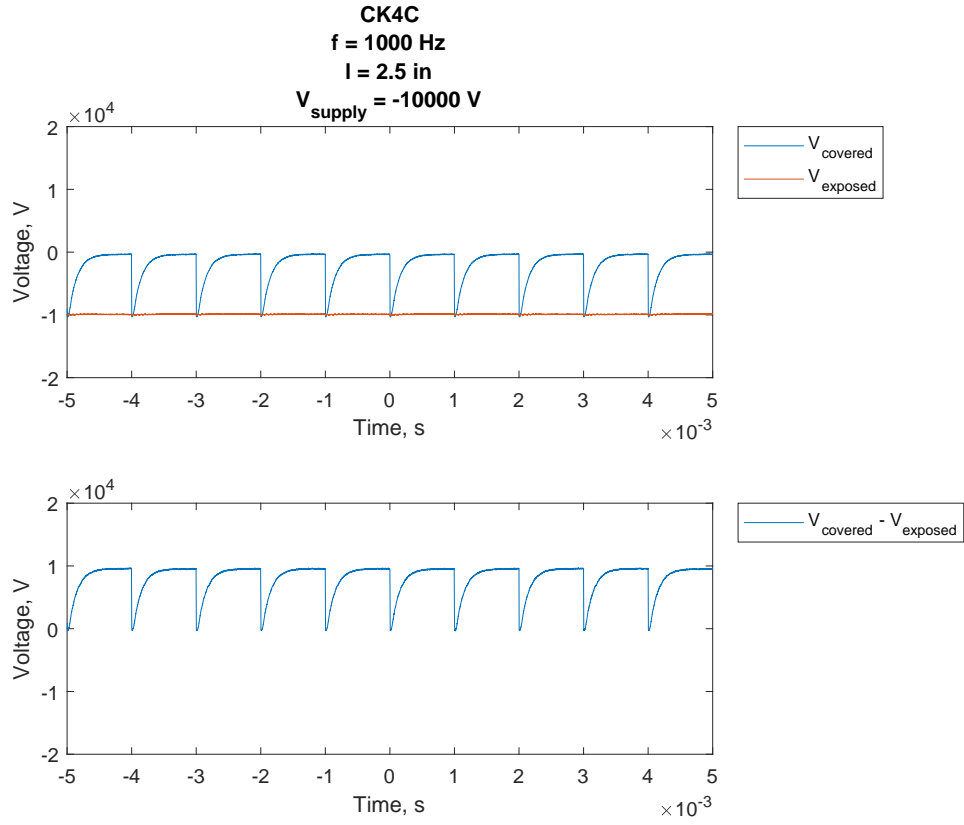


Figure 4.4. Voltage time series supplied by the negative switch to the covered and exposed electrodes of the plasma actuator. Exposed electrode held at -10 kV.

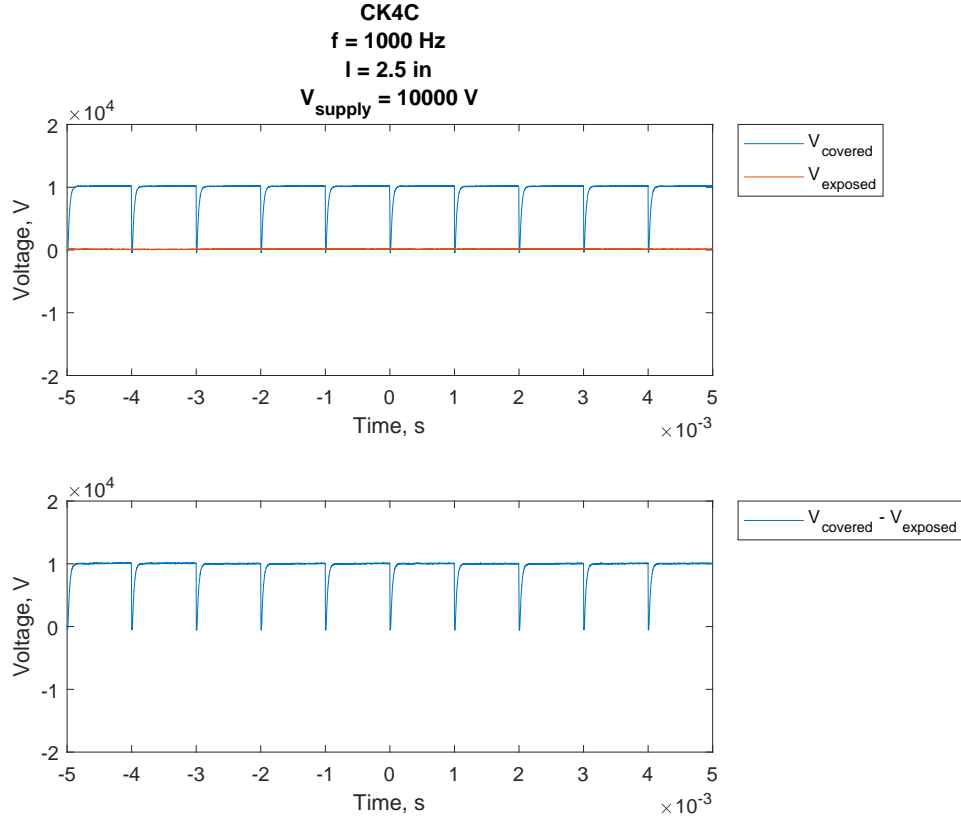


Figure 4.5. Voltage time series supplied by the positive switch to the covered and exposed electrodes of the plasma actuator. Exposed electrode held at ground.

negative charge which acts to neutralize them. Although the plasma itself should be electrically neutral, a surface DC voltmeter has been used to show that the actuator generally has a positive surface charge.

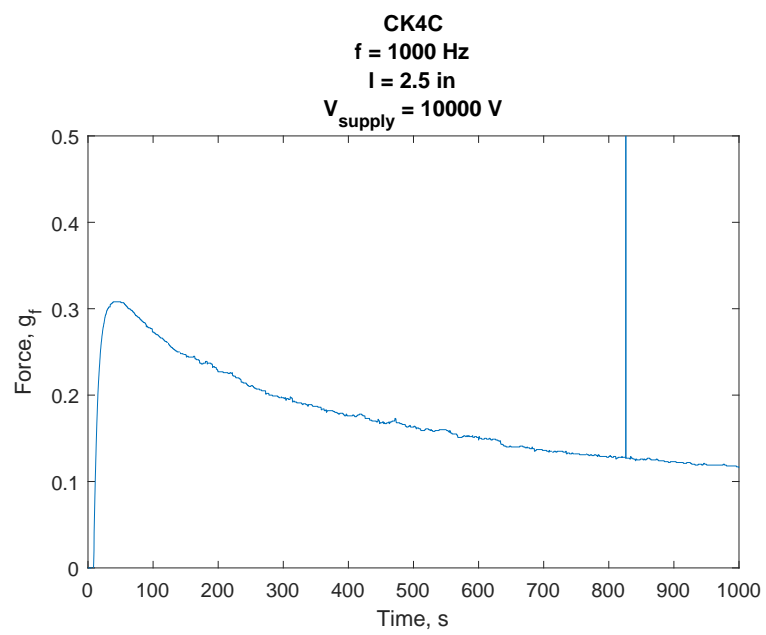


Figure 4.6. Effect of negative offset voltage on the positive pulsed-DC actuator thrust. Exposed electrode held at ground.

CHAPTER 5

STALL MARGIN EXTENSION IN THE NONCONDUCTIVE FAN FACILITY

Since the parylene coating did not provide adequate electrical insulation for the ND-TAC rotor, and the negative switch and other configurations with DC offset did not provide enough control authority, a new facility utilizing a nonconductive fan was designed and constructed for stall control experiments. The fan can be stalled in the same manner as the transonic axial compressor, and similar instrumentation as was proposed for the ND-TAC facility allowed the pulsed-DC actuator's ability to control and suppress the onset of rotating stall to be quantified. The design features of the nonconductive fan facility are detailed in the following sections, along with the experimental methodology and results.

5.1 Nonconductive Fan Plasma Actuator Stall Control Design

The “test article” of the nonconductive fan facility is an AID120 inline fan produced by Continental Fan. This fan has one rotor which was used to model and study compressor stall. The rotor blades are made from nonconductive GRP (polypropylene). Construction utilizing nonconductive materials simplified the investigation of high-voltage plasma actuation in the tip gap region: Originally, it was planned to conduct the experiment in the ND-TAC facility, but the exposed electrode had a tendency to arc to the stainless steel rotor (even when it was insulated with 1 mil of parylene C). Without an insulating coating strong and thin enough to withstand conditions in the compressor, the risk of electrical damage to the ND-TAC facility proved unacceptable.

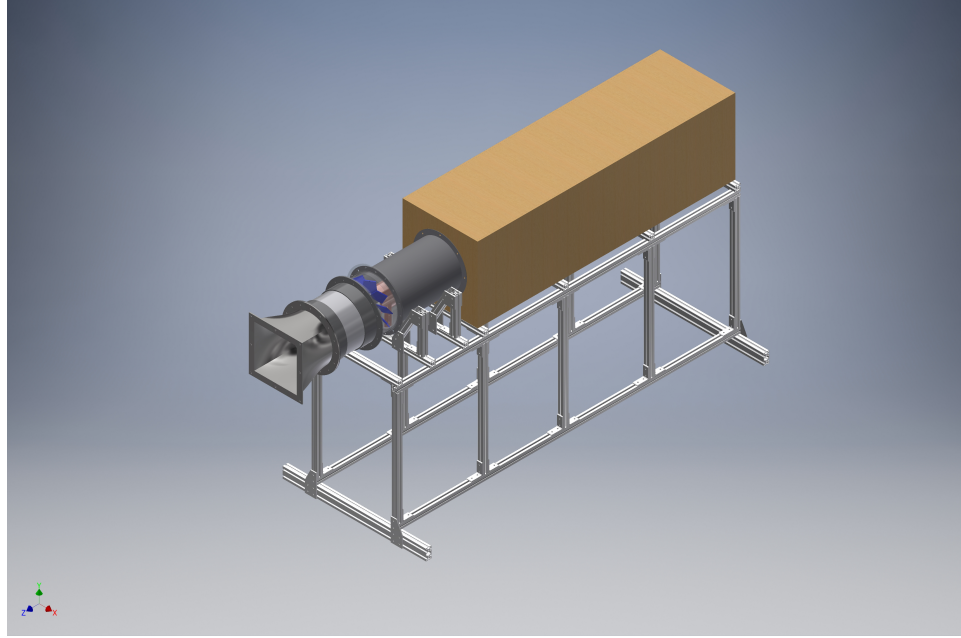


Figure 5.1. CAD rendering of test section / fan / settling chamber assembly for the nonconductive fan facility

In the nonconductive facility, the fan itself is powered by an IronHorse MTR-002-3BD36 2 hp motor, the speed of which is controlled by a GS1-22P0 variable-frequency drive (VFD). The facility also consists of an inlet contraction, a PVC test section, a downstream settling chamber, and two carts made out of 80/20 extruded aluminum. One cart supports the inlet contraction, while the other supports the test section / fan / settling chamber assembly. Figure 5.1 shows a CAD rendering of the test section / fan / settling chamber assembly. Figure 5.2 is a photograph of the constructed facility including all of the instrumentation.

5.1.1 Inlet Throttling Device

In order to control the flow rate through the fan facility, a throttling device was built out of foam board. This throttling device covered the inlet contraction. The cover was symmetrical about the duct axis and could be rotated to adjust the inlet

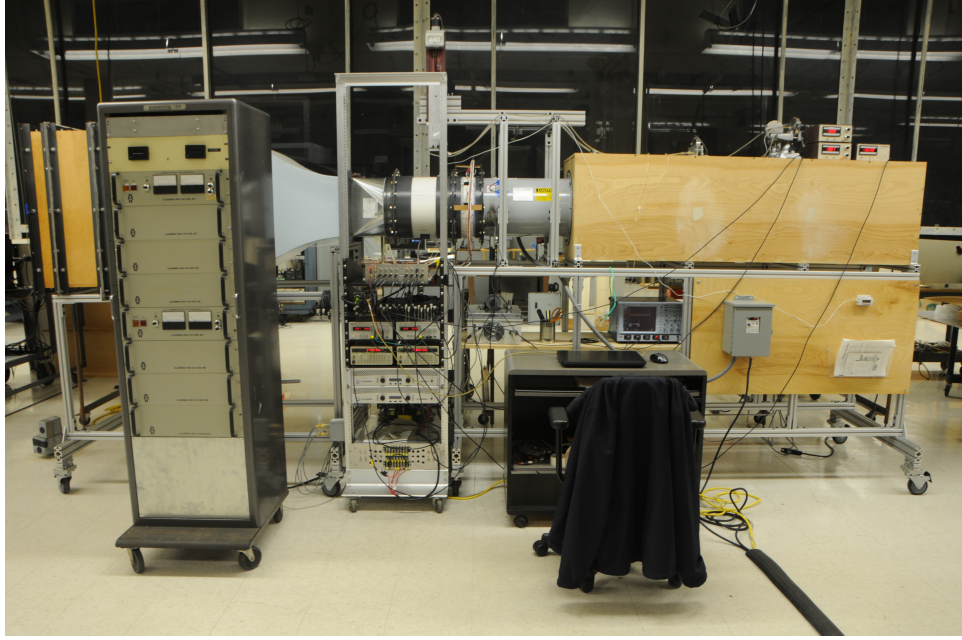


Figure 5.2. Photograph of nonconductive fan facility

area. The dimensions of the inlet throttling device are provided in the supplemental files.

To maintain consistent flow rates between experiments, the different positions of the throttling cover were marked in terms of percentage of maximum achievable open area. Therefore, the 100% throttle position refers to when it is fully open, and the 0% throttle position refers to when it is completely closed (zero flow rate).

5.1.2 Test Section

The test section can be broken down into two pieces: an 18-in-long straightening section and a 6-in-long pressure-sensing stall control section. Both pieces were machined out of NPS 12 SCH 40 PVC pipe. The length of the straightening section was selected in order to provide at least one pipe diameter for the flow to become organized before reaching the measurement stations. At the inlet of the straightening section, an aluminum perforated sheet with a porosity of 79% also helps to ensure

homogeneous, fully-developed flow. The straightening section has a 12.19-in inside diameter (the same as that of the fan housing).

For stall control experiments, the 6-in-long tube is located between the 18-in-long tube and the AID120 fan to act as the outer casing directly over the fan rotor. This tube has the same inside diameter of 12.19 in, giving a tip clearance gap of 95 mil (3.0% of tip chord). It also includes a circumferential recess for up to eight plasma actuator segments, sixteen ports for housing the DBD electrode cables, and eight equally-spaced ports for pressure-sensing microphones. The circumferential recess is 2 in long and 20 mil deep and provides flexibility for a variety of plasma actuator configurations and axial locations. Meanwhile, the microphone ports are located $0.1c$ upstream of the rotor leading edge plane, which is a commonly-used placement in the literature [4]. These ports have been sized for Knowles FG Series omni-directional microphones. The complete dimensions of the stall control test section are provided in the supplemental files.

5.1.3 Fan

The rotor used in the AID120 fan is an Elta Model 012/150/10/34. The fan data as specified by the manufacturer are summarized in Table 5.1. This fan is powered by an IronHorse MTR-002-3BD36 2 hp motor, the speed of which is controlled by a GS1-22P0 variable-frequency drive. The VFD displays the motor rpm based on the input frequency.

5.1.4 Outlet Settling Chamber

A wooden box just downstream of the fan acts as an outlet settling chamber. The purpose of this chamber is to absorb the kinetic energy of the upstream flow and allow its expansion as though it were unconfined. The box measures 21 in \times 21 in \times 72 in and is built out of 1/2-in-thick birch plywood. As with the straightening section,

TABLE 5.1

FAN DATA (AT STP)

Quantity	Value
Type	Axial impeller
Diameter	12 in
Hub	150 mm
Impeller Blades	10
Pitch	34°
Blade Material	GRP (polypropylene)
Speed	3500 rpm
Absorbed Power	1.82 hp
Peak Power	1.92 hp
Total Efficiency	39%

an aluminum perforated sheet with a porosity of 79% is located at the inlet to help ensure the flow is homogeneous and fully-developed after exiting the fan.

5.2 Experimental Setup

To determine whether pulsed-DC plasma actuation would have any effect on the stall cells (and consequently the fan performance), eight 2.5-in-long actuator segments were installed to cover the full azimuth of the test section ring. This length was chosen because it is the same as that tested during thrust measurements with the digital scale. The electrodes were made out of copper foil tape, while the dielectric layer consisted of 5 mil of Ultem. Plastic shim stock was used to fill the gaps in between the actuator segments and maintain a smooth surface. Figure 5.3a shows all eight actuator segments installed in the test section ring, while Figure 5.3b shows a long exposure photograph taken of the ring during operation. A closeup of an actuator segment is provided in Figure 5.4; two microphones are visible to the left and right of the actuator.

To power the plasma actuators, the stacked MOSFET switch designed by Creare for the Phase I NASA SBIR program was replicated. A Glassman PS/PH050R60-X18 with a maximum voltage rating of 50 kV and a maximum current limit of 60 mA was used for the high-voltage DC power supply. Meanwhile, a Stanford Research Systems DS345 function generator was used to trigger the switch. The settings entered to create the trigger waveform are listed in Table 5.2; these result in a pulse width of 2 μ s.

The current and voltage supplied to the actuators were monitored with an inductive current sensor (Pearson Model 2100) and high voltage probe (LeCroy PPE 20 kV) respectively. These time series were viewed and saved with a LeCroy Waverunner-2 LT264 oscilloscope.

The ambient pressure, temperature, and relative humidity in the lab were all read

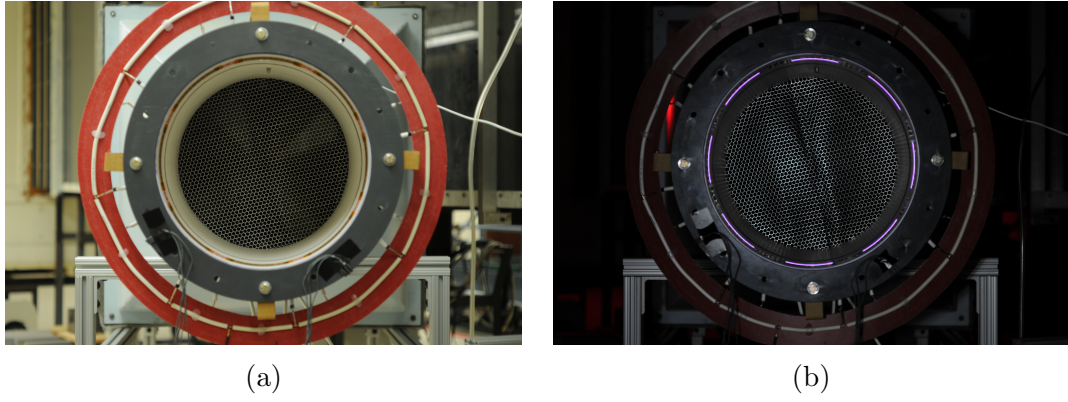


Figure 5.3. (a) Full azimuth actuator ring; (b) long exposure photograph of ring during operation

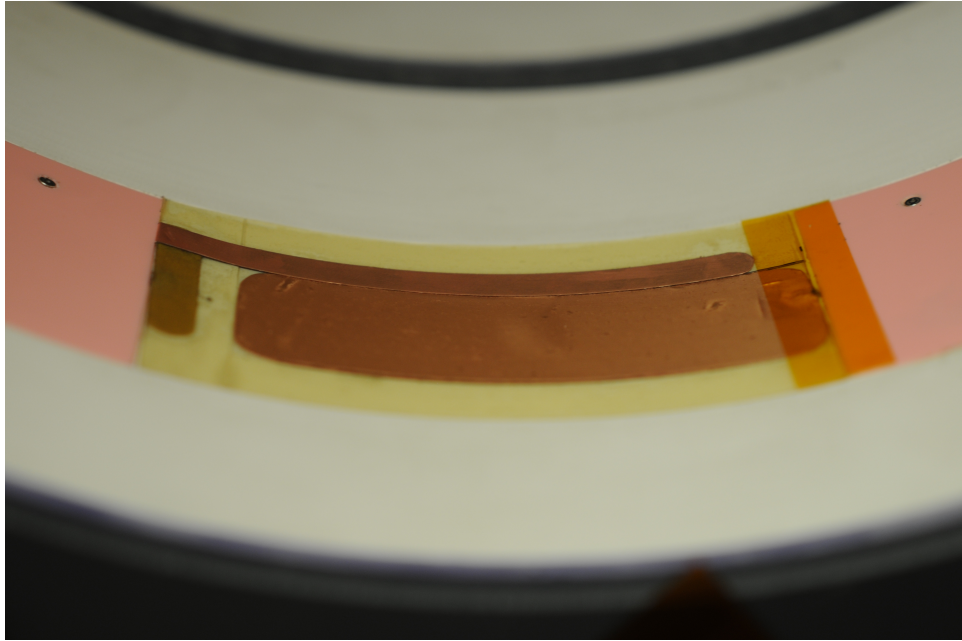


Figure 5.4. Photograph of actuator arc segment installed in test section

TABLE 5.2
FUNCTION GENERATOR SETTINGS ENTERED FOR TRIGGER
WAVEFORM

Setting	Value
Function	Square
Frequency	250 kHz
Amplitude	5 V _{pp}
Offset	2.5 V _{pp}
Phase	180°
Modulation	Burst
Burst Count	1
Trigger Rate	500/1000/2000 Hz

off a digital barometer made by Fisher Scientific (catalog no. 14-650-118). A Taylor 9940 digital thermometer located 9 in upstream of the fan inlet plane was used to record the dry bulb temperature of the flow entering the fan.

The static and dynamic pressure upstream of the fan were measured by means of a Dwyer 166-12 pitot-static tube. Meanwhile, the static pressure downstream of the fan was measured using four wall tapings which were bored into the settling chamber and connected together. The upstream station was located 12 in upstream of the fan inlet plane, while the downstream station was located 13 in downstream of the fan outlet plane. These locations were chosen to minimize the effects of the motor wake and other disturbances in the flow. Two Validyne DP103 pressure transducers attached to the static pressure ports at the upstream and downstream stations output voltage signals proportional to gauge pressure. A -18 diaphragm was used for the upstream station, while a -12 diaphragm was used for the downstream location. Similarly, a DP103 transducer with a -14 diaphragm output a voltage signal proportional to the dynamic pressure measured by the pitot-static tube. All of the DP103 transducers were used in conjunction with CD23/223 demodulator boxes and were positioned on top of the settling chamber as shown in Figure 5.2.

Eight electret microphones (Knowles FG-23329-P07) equally distributed around the test section allowed the detection of traveling stall cells and other pressure fluctuations. These microphones were placed $0.1c$ upstream of the rotor leading edge plane as recommended in Cameron and Morris [4]. To correlate the microphone traces and other time series data to the rotation of the fan, a Monarch Instrument Remote Optical Sensor (ROS) placed at top dead center of the fan measured its rotation rate. The ROS output a voltage pulse whenever its LED light source was reflected from a square of T-5 tape affixed to one of the rotor blades.

Before they were sampled, the voltage signals from the pressure transducers, microphones, and rpm sensor were passed through anti-aliasing filters with cutoff fre-

quencies of 5 kHz and gained as necessary. They were then acquired at 10 kHz by a UEI DNA-AI-201-100 analog input layer installed in a DNA-PPC5-1G PowerDNA I/O Cube. The Cube was connected to a laptop computer which was utilized for post-processing of the data.

Because the pulsed-DC waveform generates significant EMI during the pulse, it was desired to acquire data in between pulses. To do this, it was necessary to synchronize the pulse’s timebase with that of the AI-201. The function generator supplying the trigger waveform was synchronized with another identical function generator via their 10 MHz inputs/outputs. This function generator then supplied a 10 kHz square wave to the AI-201’s EXTCLK input. Finally, the 10 kHz signal was delayed by 6 μ s to give a window of 4 μ s between its rising edges and the pulses.

5.3 Stall Cell Measurements

The purpose of the microphones installed in the test section ring was to detect the passage of traveling stall cells that are known to form prior to a fully-stalled condition. In turn, it was desired to dynamically observe the suppression of these stall cells as they convected past the plasma actuators. The article by Cameron and Morris [4] compares various methods of analyzing axial compressor stall inception using unsteady casing pressure measurements. For these experiments, two methods of data processing are considered. First, it is possible to identify rotating features through visual inspection of the pressure traces, although the method is more qualitative than quantitative and somewhat open to interpretation. Furthermore, this method is sensitive to filtering, and the data have been passed through anti-aliasing filters as mentioned previously. Regardless, visual inspection provides an easy means of qualitatively comparing the plasma-on and -off traces to identify whether the actuator is effective at reducing the magnitude or frequency of the rotating features.

The second method considered is the spatial correlation metric (SCM) developed

by Cameron and Morris [4]. This technique utilizes a windowed two-point time-delay correlation between adjacent sensors, so the SCM can be calculated at eight unique azimuthal locations in the nonconductive fan facility. The SCM is a scalar metric which is nonzero only when disturbances which rotate in the same direction as the rotor are present. It is defined as

$$\chi(\theta, t_0) = \int_{\tau_{\min}}^{\tau_{\max}} R_{\theta, \theta + \delta\theta}(\tau|_{t_0}) d\tau \quad (5.1)$$

where the windowed, two-point cross-correlation of the casing pressure is defined as

$$R_{\theta, \theta + \delta\theta}(\tau|_{t_0}) = \int_{-\infty}^{\infty} \hat{P}_{\theta}(t|_{t_0}) P_{\theta + \delta\theta}(\tau - t) dt \quad (5.2)$$

Compared to visual inspection, the SCM provides a more quantitative analysis of stall inception and is less sensitive to filtering.

The plasma actuators were hypothesized to have the most effect on the stall cells when they first start to form and rotate around the fan. (At higher flow rates, there are no stall cells to control, but at lower flow rates, the stall cells may be too strong.) To find the corresponding throttle position, the throttle was closed off in steps, and both the pressure traces and the spatial correlation metric were examined for evidence of rotating disturbances. The pressure traces were low-pass filtered at $5n$ in order to remove higher-frequency content associated with the blade passage. A cross-correlation window length corresponding to 0.25 of a rotor revolution was chosen for calculating the SCM, and the rotating speed range was selected to be between 0.3 and 1.0 times the shaft rotation rate.

Figures 5.5a and 5.5b show the pressure traces and SCM respectively for various throttle positions. The stall cells are visible as pressure fluctuations which rotate around the ring as time increases. Note that the stall cells travel in the same direction as the rotor (θ has been defined to increase in the direction of rotor rotation), but they

rotate at approximately half the rate of the rotor. At 60% of the maximum open inlet area, some faint streaks are visible, but the magnitude of the SCM is comparatively low. At 50%, disturbances begin to grow and dissipate around $\theta = 180^\circ$. At 40%, the stall cells are clearly visible in the pressure traces and the SCM has the highest magnitude; a change in the sound produced by the fan indicated this was close to its stall point. At 30%, the fan goes deeper into stall, and the disturbances either grow in size or rotate at a different speed so that they lose correlation.

As the stall cells were most easily observed at the 40% throttle position, this point was then used to study the effect of pulsed-DC plasma actuation. The fan was operated in the stall condition at 3501 rpm for 90 s. At $t = 40$ s, the switching circuit was turned on and the voltage raised to the desired amplitude. Both pulse frequency and amplitude were varied to see which values were most effective.

5.3.1 Actuators at $x = -0.07c_{ax}$

The first actuator location to be discussed is $0.07c_{ax}$ upstream of the rotor leading edge plane. This location was found by Vo [40] to be optimal for casing plasma actuation, and he used it later for an updated simulation of SDBD actuators in subsonic compressors [41]. The electrodes of the actuator were therefore positioned to overlap one another at this location.

The pressure traces are useful for visualizing the stall cells, but it is difficult to quantify the effect of the plasma actuator by looking for differences in their magnitudes. A better way to measure the plasma's impact on the correlation of rotating disturbances in space and time is to use the SCM; here a lower SCM corresponds to less correlation. In Figure 5.6, the SCM is computed for one window of time with plasma off and one with plasma on. As can be seen by comparing the left and right halves of the figure, the plasma actuation reduces the streaks associated with rotating disturbances.

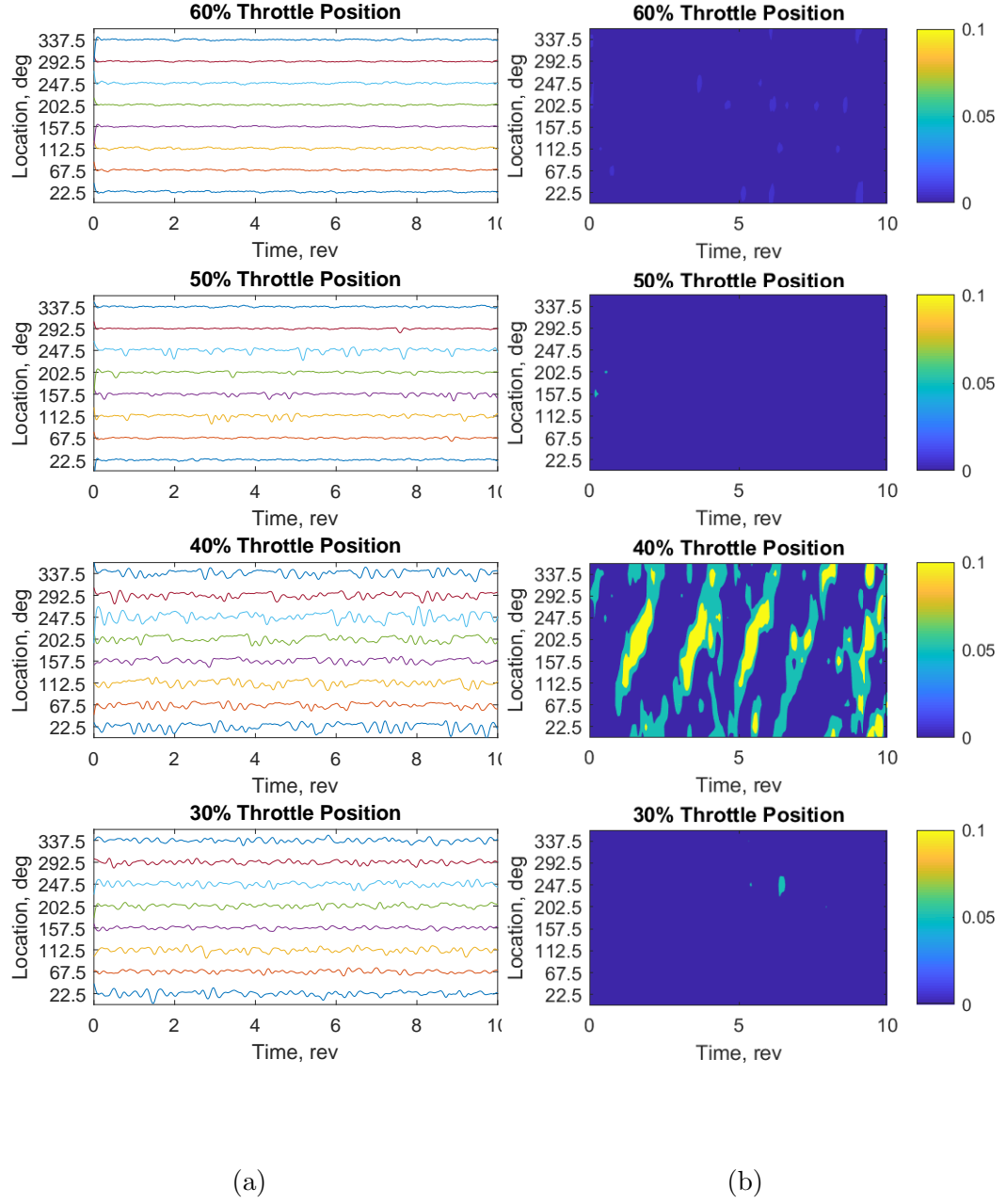


Figure 5.5. (a) Low-pass filtered pressure traces for various throttle positions ($f_c = 5n$); (b) SCM for various throttle positions

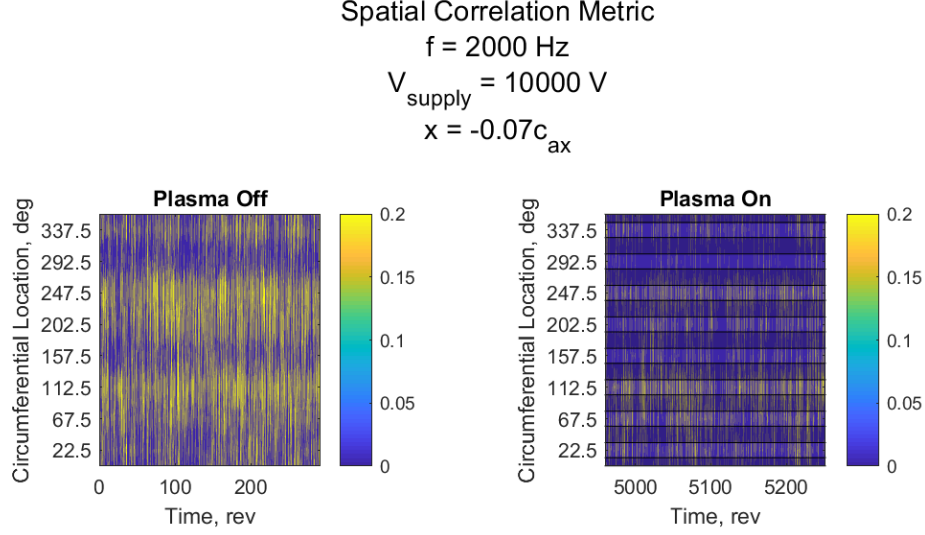


Figure 5.6. Spatial correlation metric with plasma off and plasma on ($f_c = 5n$). The dark bands represent the locations of the actuator segments.

On the left side of Figures 5.7–5.18, the mean of the spatial correlation metric is calculated for the same time windows and plotted as a function of location for several different pulse amplitudes. The reduction in this mean due to plasma actuation is plotted on the right side. Because a reduction in an already negative χ value would mean an increase in pressure fluctuation magnitude, any negative χ values have been set to 0 before taking the mean. (Negative χ values indicate similarly-shaped disturbances of opposite sign at the adjacent microphone; thus, the original disturbance either has not rotated across the sensors or has changed.) Examining Figures 5.7–5.18, we can more easily see that the plasma actuation generally reduces the correlation of the pressure fluctuations at each location as compared to the plasma-off cases. The reduction in correlation increases with frequency and number of actuator segments.

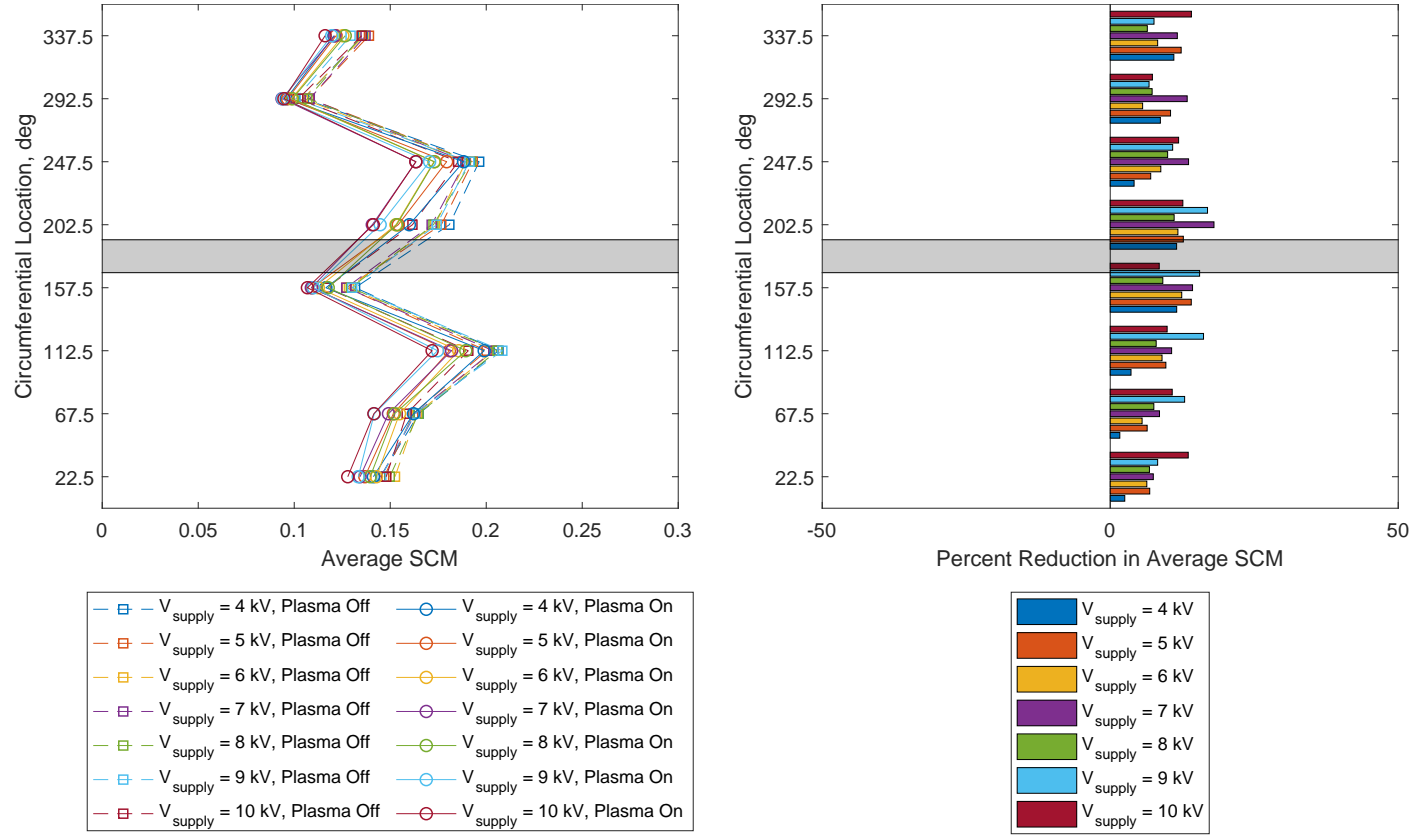


Figure 5.7. 00001000 1 segment configuration ($f = 500 \text{ Hz}$, $x = -0.07c_{ax}$);
 (left) mean spatial correlation metric with plasma off and plasma on;
 (right) reduction in mean spatial correlation metric. The dark bands
 represent the locations of the actuator segments.

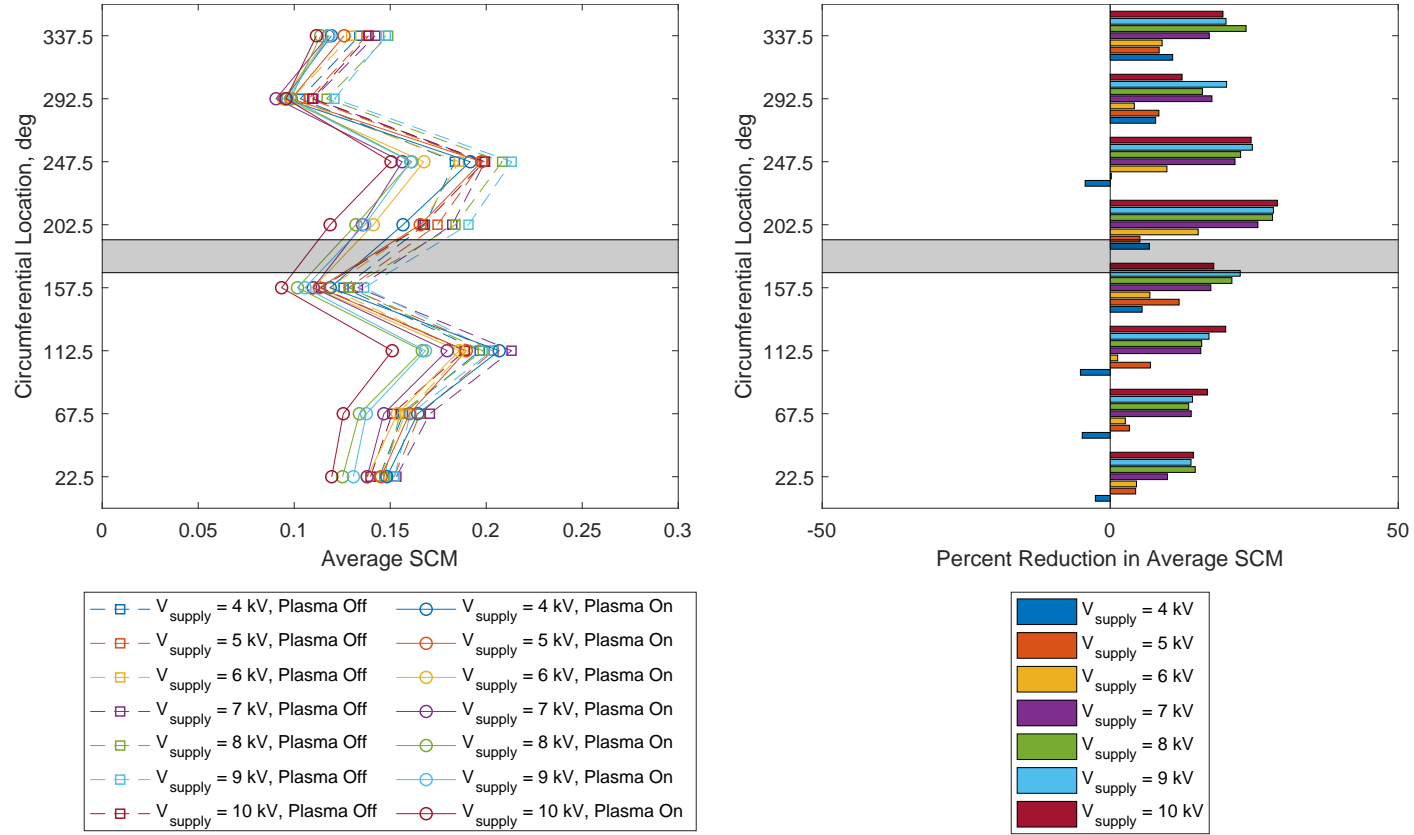


Figure 5.8. 00001000 1 segment configuration ($f = 1$ kHz, $x = -0.07c_{ax}$);
 (left) mean spatial correlation metric with plasma off and plasma on;
 (right) reduction in mean spatial correlation metric. The dark bands
 represent the locations of the actuator segments.

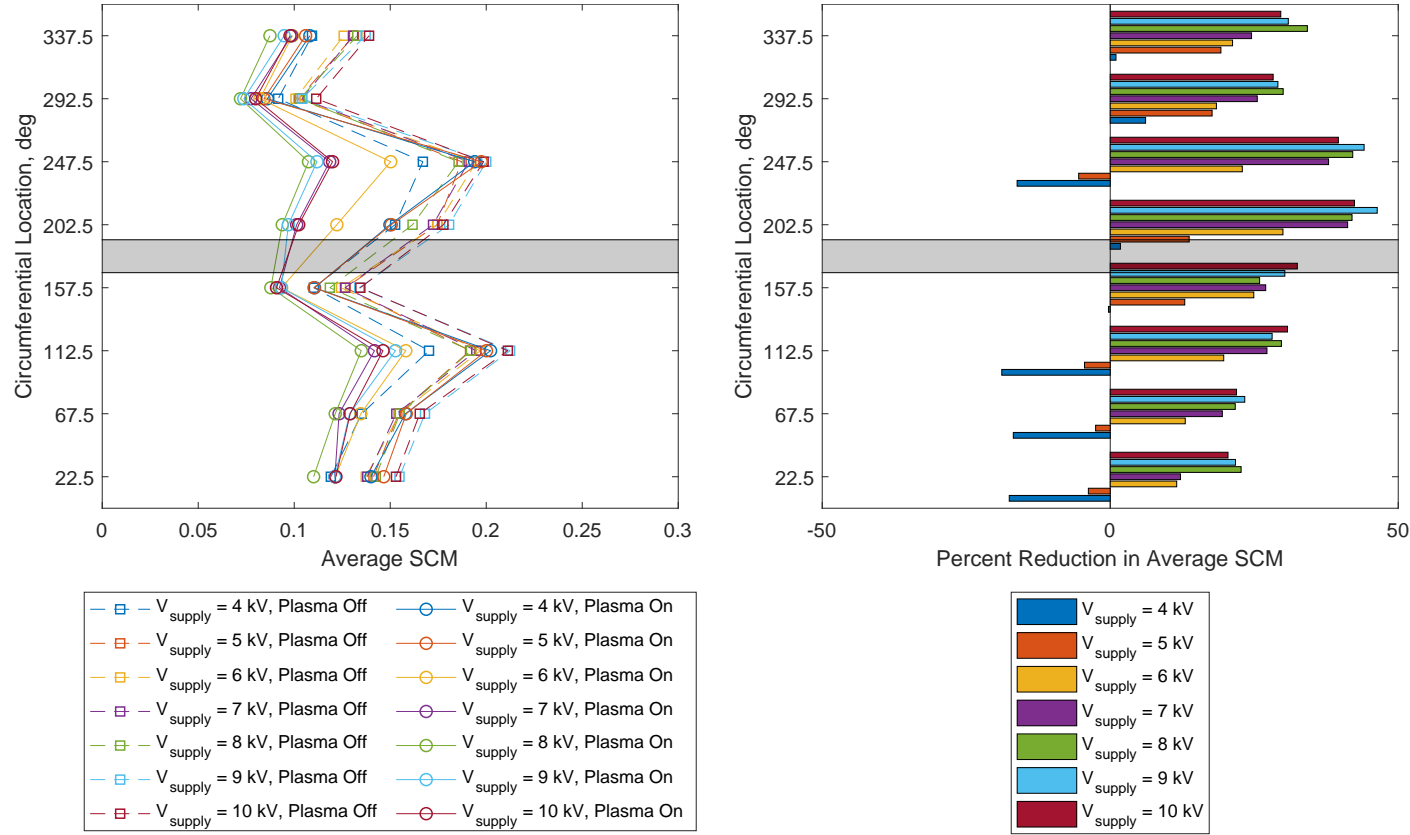


Figure 5.9. 00001000 1 segment configuration ($f = 2$ kHz, $x = -0.07c_{ax}$);
 (left) mean spatial correlation metric with plasma off and plasma on;
 (right) reduction in mean spatial correlation metric. The dark bands
 represent the locations of the actuator segments.

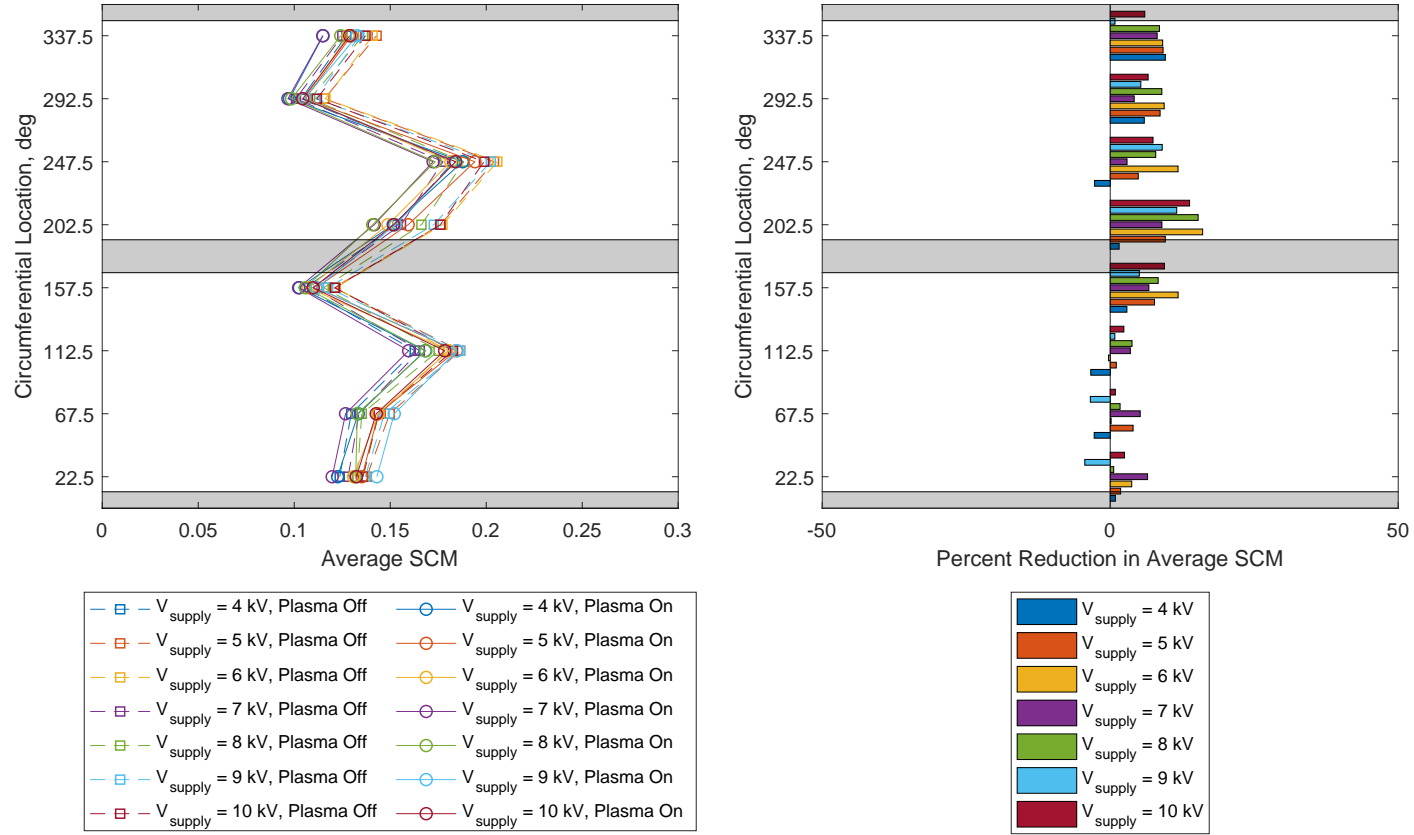


Figure 5.10. 10001000 2 segment configuration ($f = 500 \text{ Hz}$, $x = -0.07c_{ax}$);
 (left) mean spatial correlation metric with plasma off and plasma on;
 (right) reduction in mean spatial correlation metric. The dark bands
 represent the locations of the actuator segments.

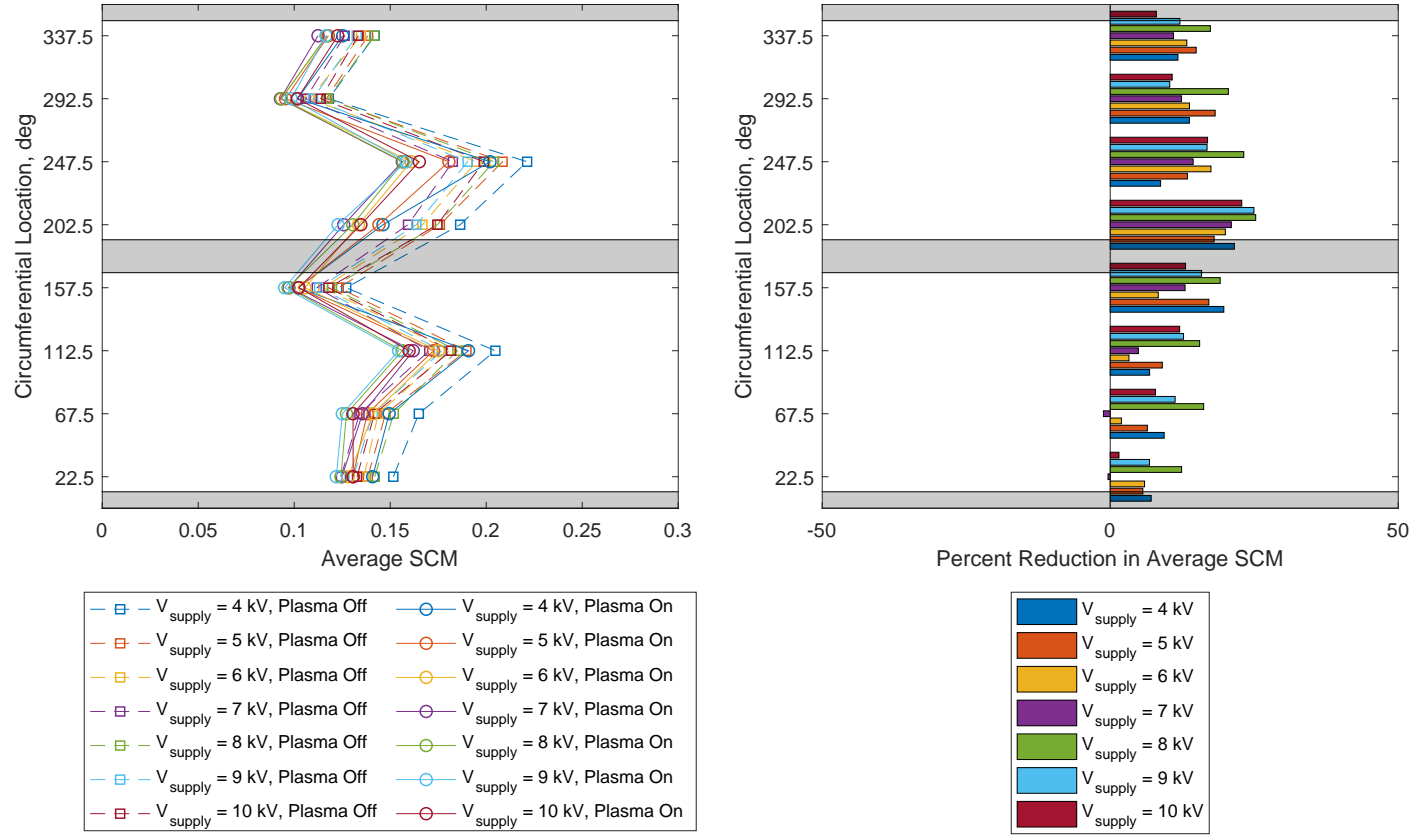


Figure 5.11. 10001000 2 segment configuration ($f = 1 \text{ kHz}$, $x = -0.07c_{ax}$);
 (left) mean spatial correlation metric with plasma off and plasma on;
 (right) reduction in mean spatial correlation metric. The dark bands
 represent the locations of the actuator segments.

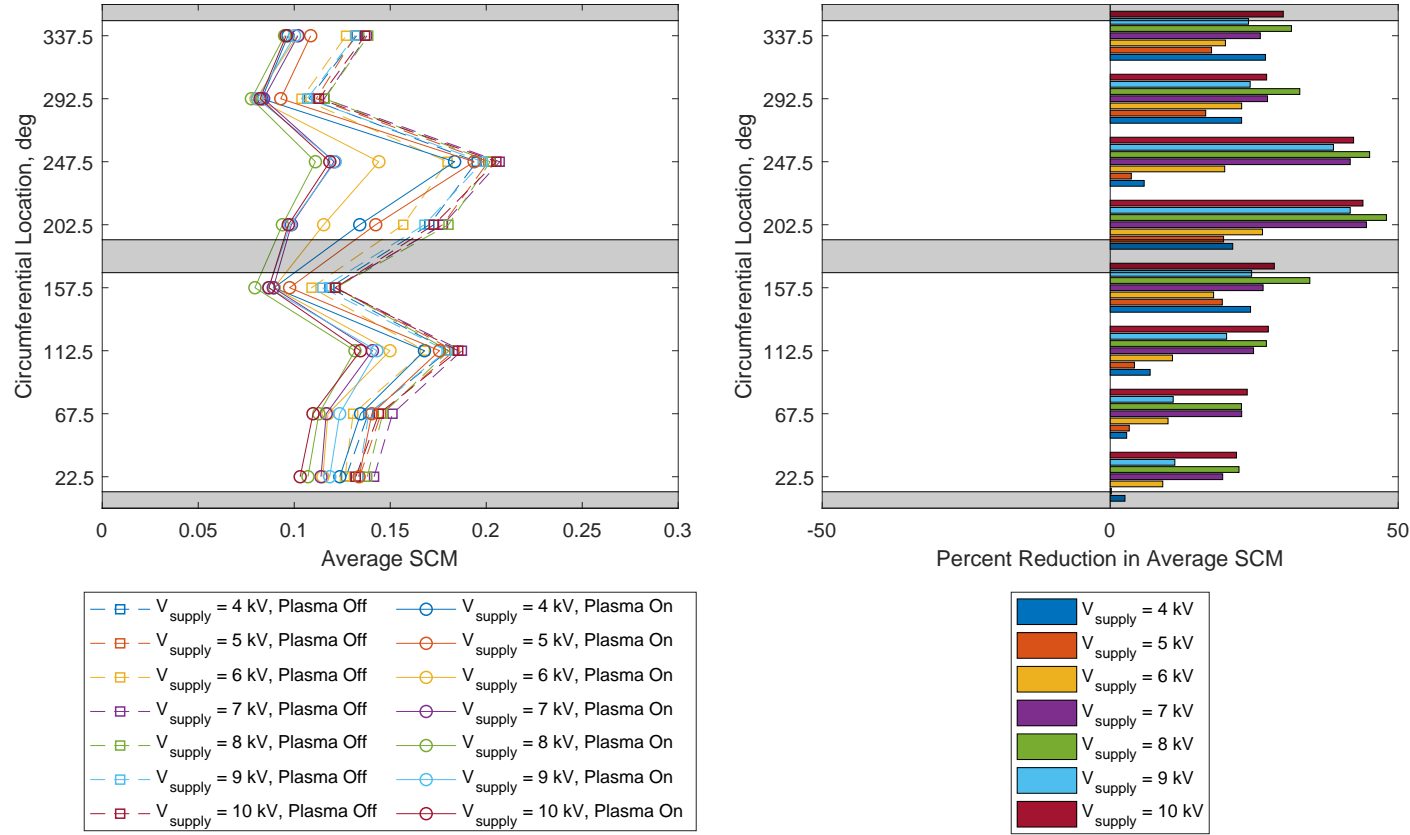


Figure 5.12. 10001000 2 segment configuration ($f = 2 \text{ kHz}$, $x = -0.07c_{ax}$);
 (left) mean spatial correlation metric with plasma off and plasma on;
 (right) reduction in mean spatial correlation metric. The dark bands
 represent the locations of the actuator segments.

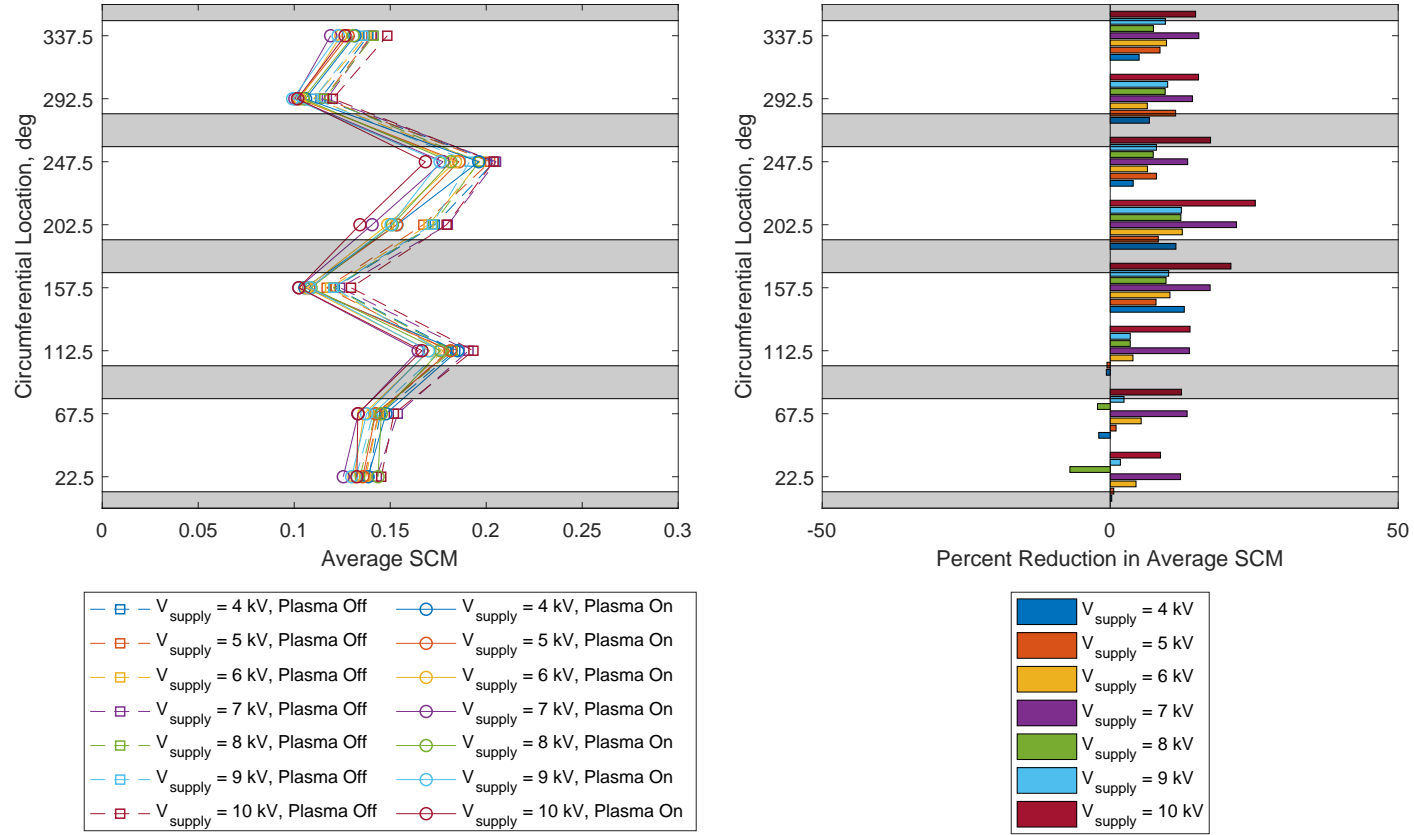


Figure 5.13. 10101010 4 segment configuration ($f = 500 \text{ Hz}$, $x = -0.07c_{ax}$);
 (left) mean spatial correlation metric with plasma off and plasma on;
 (right) reduction in mean spatial correlation metric. The dark bands
 represent the locations of the actuator segments.

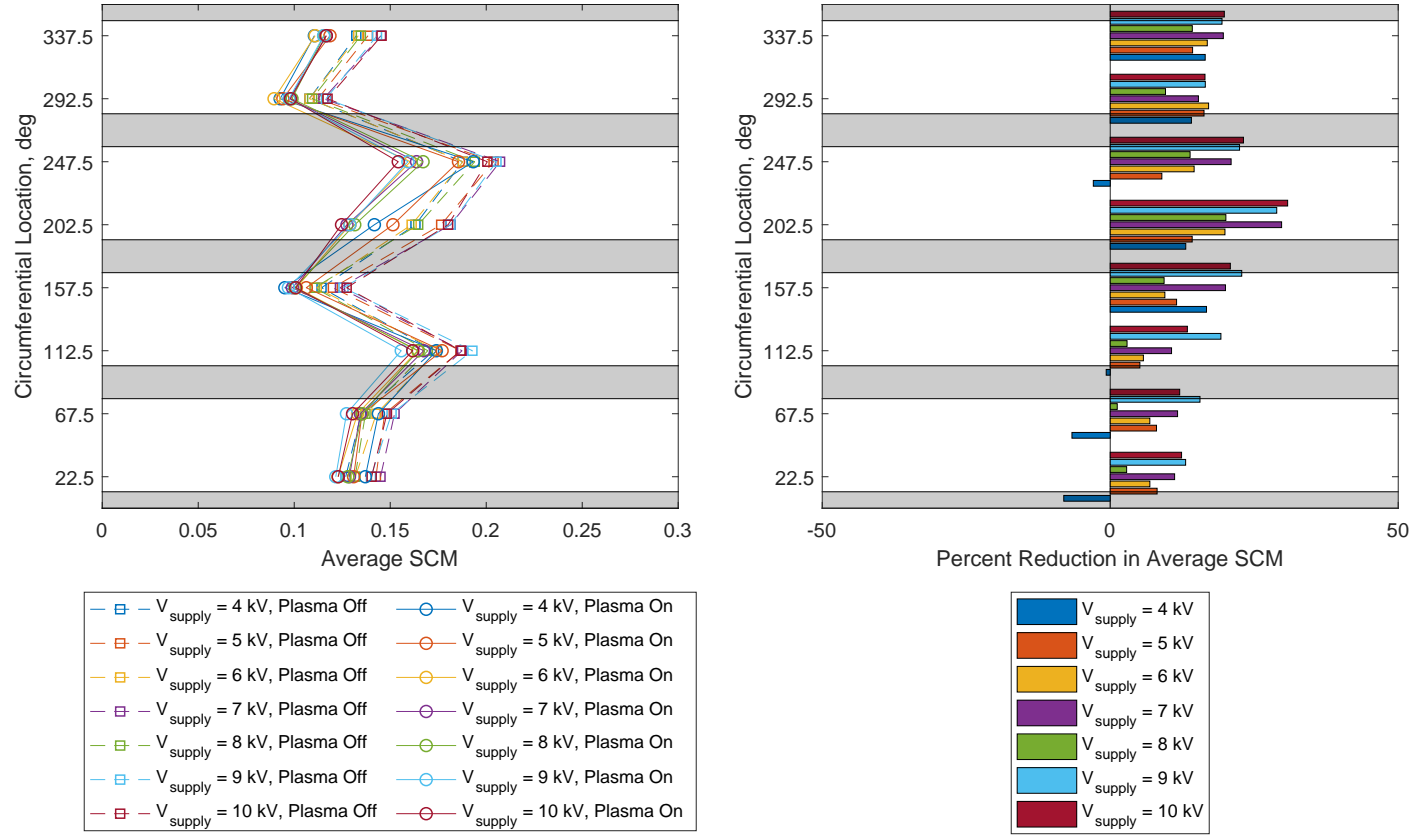


Figure 5.14. 10101010 4 segment configuration ($f = 1 \text{ kHz}$, $x = -0.07c_{ax}$);
 (left) mean spatial correlation metric with plasma off and plasma on;
 (right) reduction in mean spatial correlation metric. The dark bands
 represent the locations of the actuator segments.

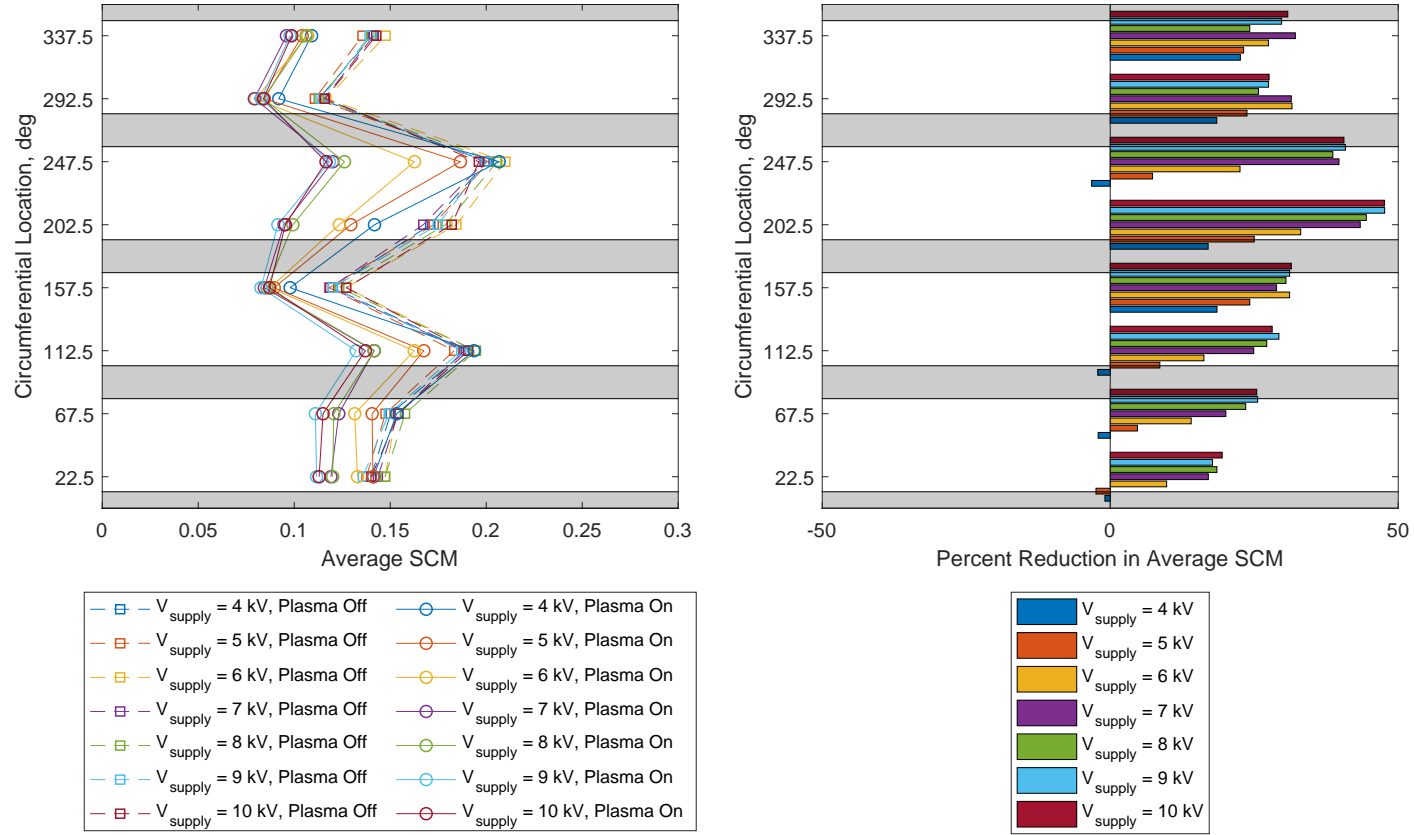


Figure 5.15. 10101010 4 segment configuration ($f = 2 \text{ kHz}$, $x = -0.07c_{ax}$);
 (left) mean spatial correlation metric with plasma off and plasma on;
 (right) reduction in mean spatial correlation metric. The dark bands
 represent the locations of the actuator segments.

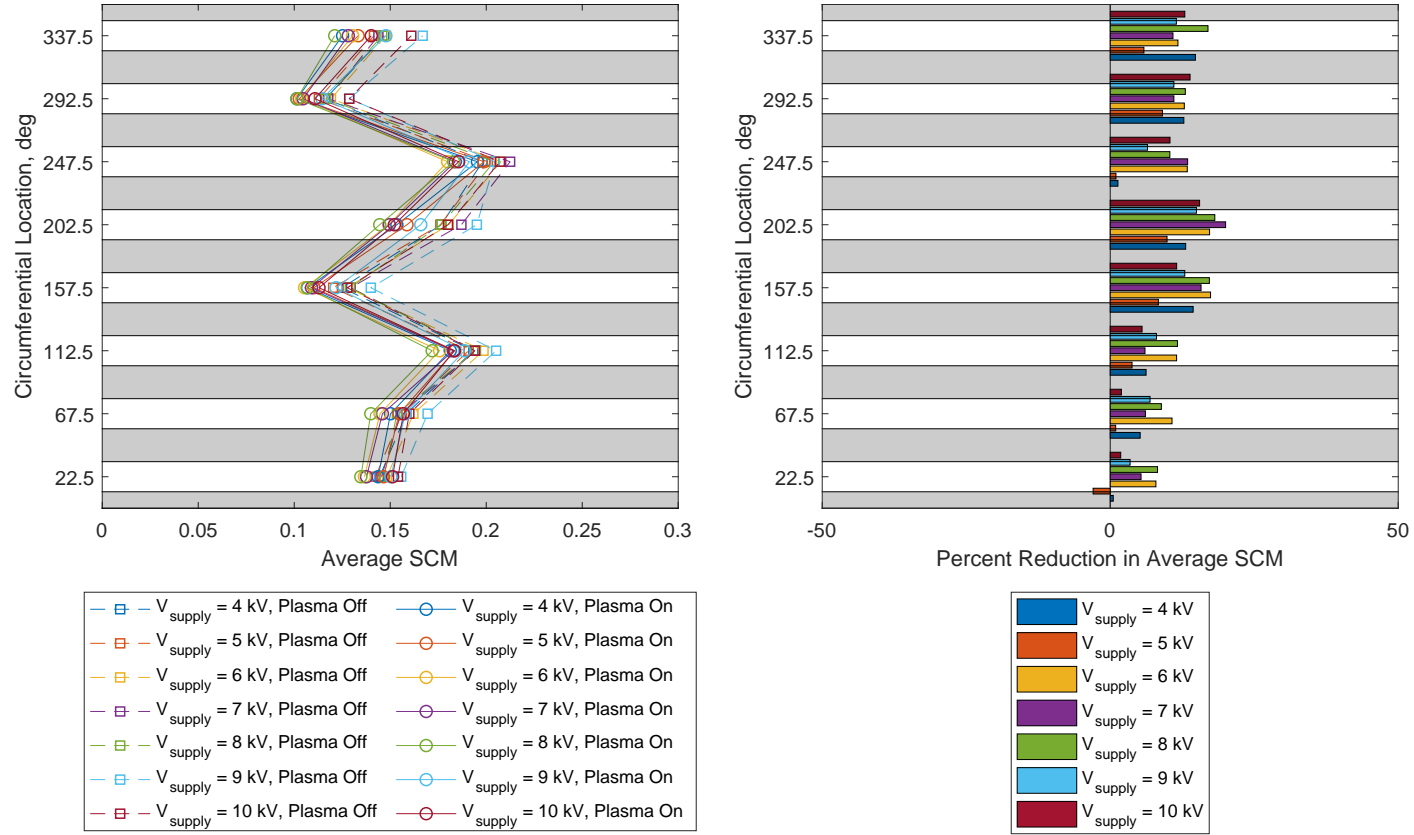


Figure 5.16. 11111111 8 segment configuration ($f = 500 \text{ Hz}$, $x = -0.07c_{ax}$);
 (left) mean spatial correlation metric with plasma off and plasma on;
 (right) reduction in mean spatial correlation metric. The dark bands
 represent the locations of the actuator segments.

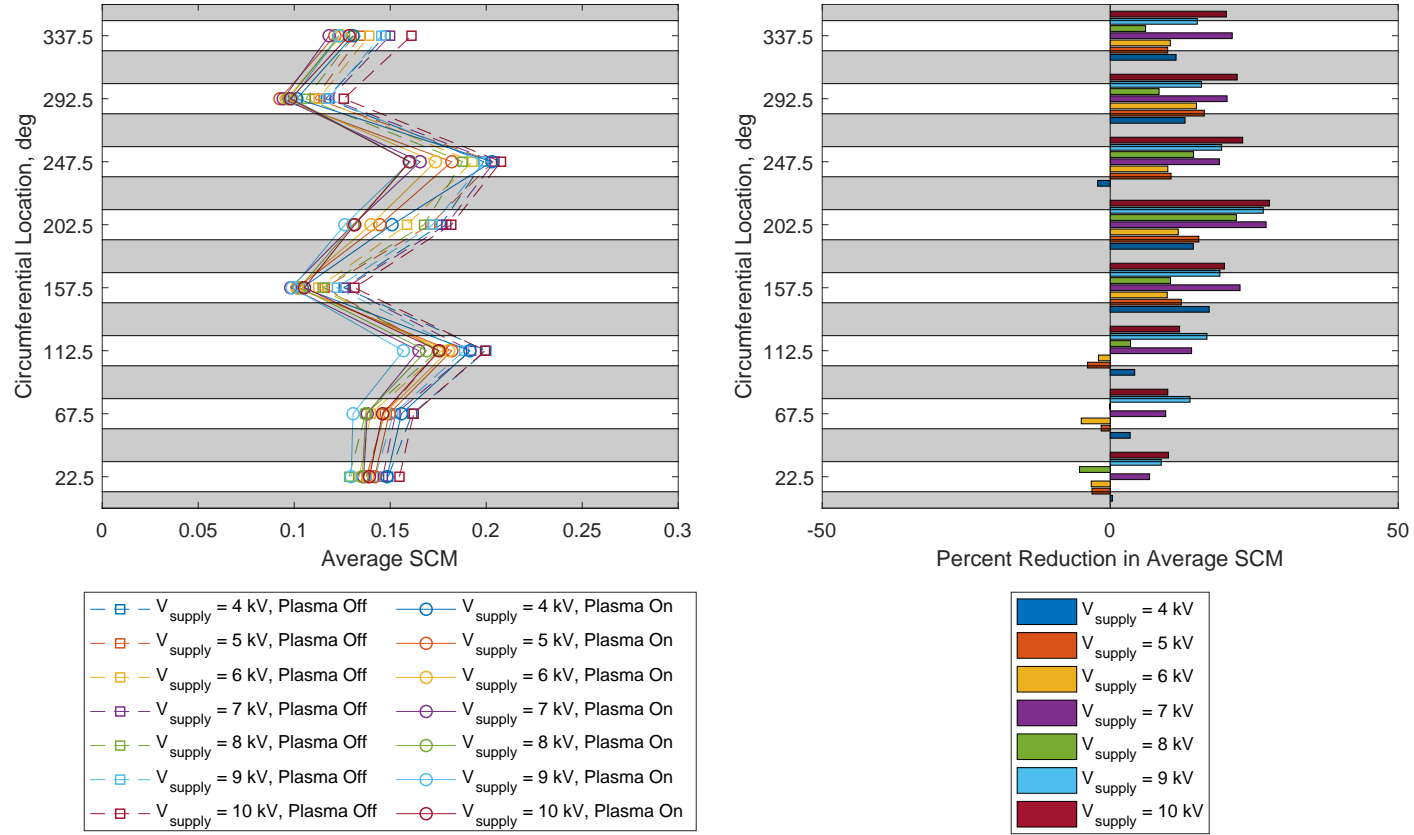


Figure 5.17. 11111111 8 segment configuration ($f = 1 \text{ kHz}$, $x = -0.07c_{ax}$);
 (left) mean spatial correlation metric with plasma off and plasma on;
 (right) reduction in mean spatial correlation metric. The dark bands
 represent the locations of the actuator segments.

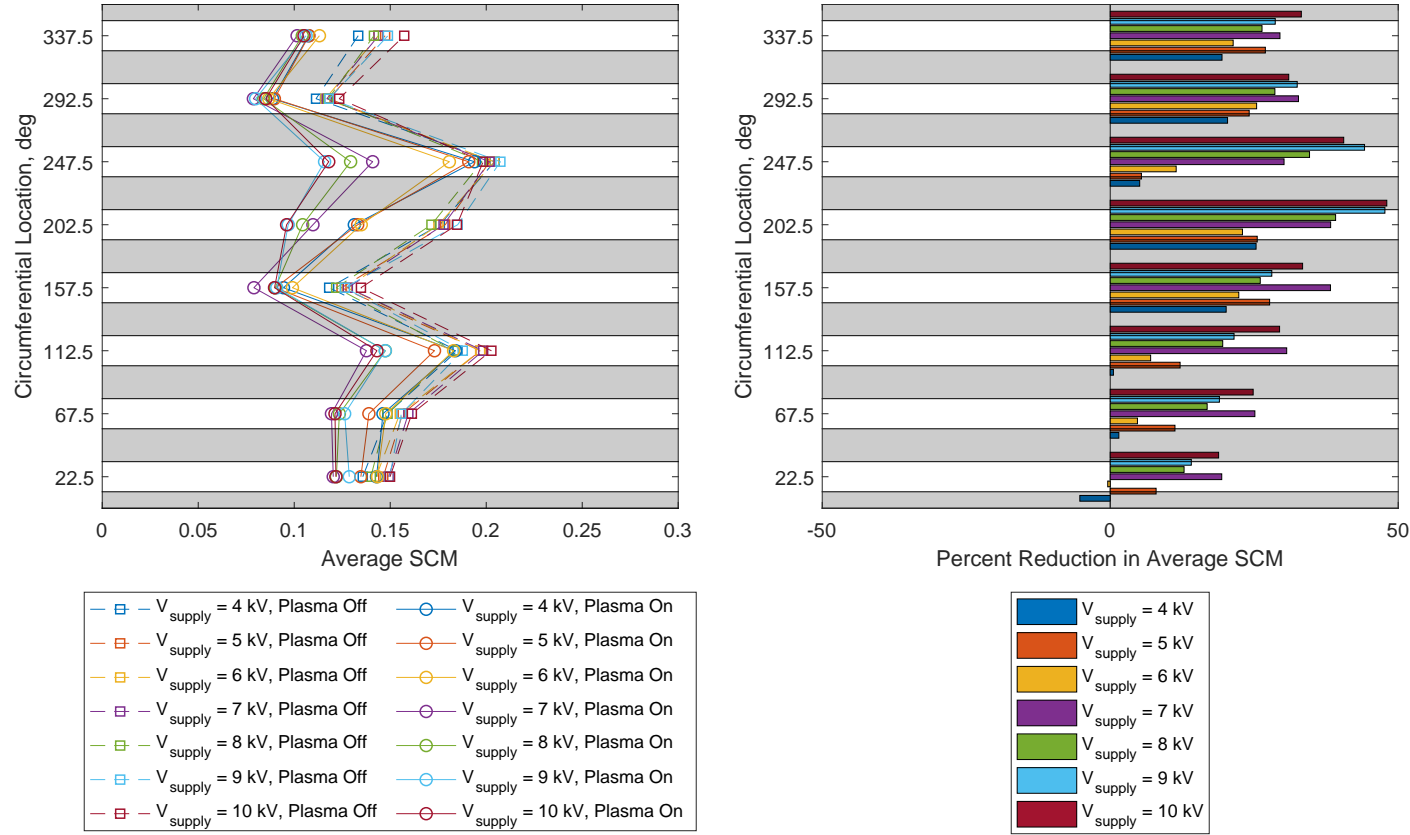


Figure 5.18. 11111111 8 segment configuration ($f = 2 \text{ kHz}$, $x = -0.07c_{ax}$);
 (left) mean spatial correlation metric with plasma off and plasma on;
 (right) reduction in mean spatial correlation metric. The dark bands
 represent the locations of the actuator segments.

5.3.2 Actuators at $x = 0.12c_{ax}$

Another actuator location which was investigated was downstream of the rotor leading edge plane at $x = 0.12c_{ax}$. Houghton and Day [18] found a local maximum at this location while performing a parametric study on stall margin improvement as affected by the location of casing grooves. Although the present work investigates a plasma casing treatment as opposed to circumferential grooves, the method of extending stall margin by axially injecting momentum into the tip jet is thought to be the same. On the left side of Figures 5.19–5.30, the mean of the spatial correlation metric is calculated for a plasma-off and plasma-on time window and plotted as a function of location for several different pulse amplitudes. The reduction in this mean due to plasma actuation is plotted on the right side. The change in correlation is minimal or positive at the 292.5° location, but here the correlation is low to begin with.

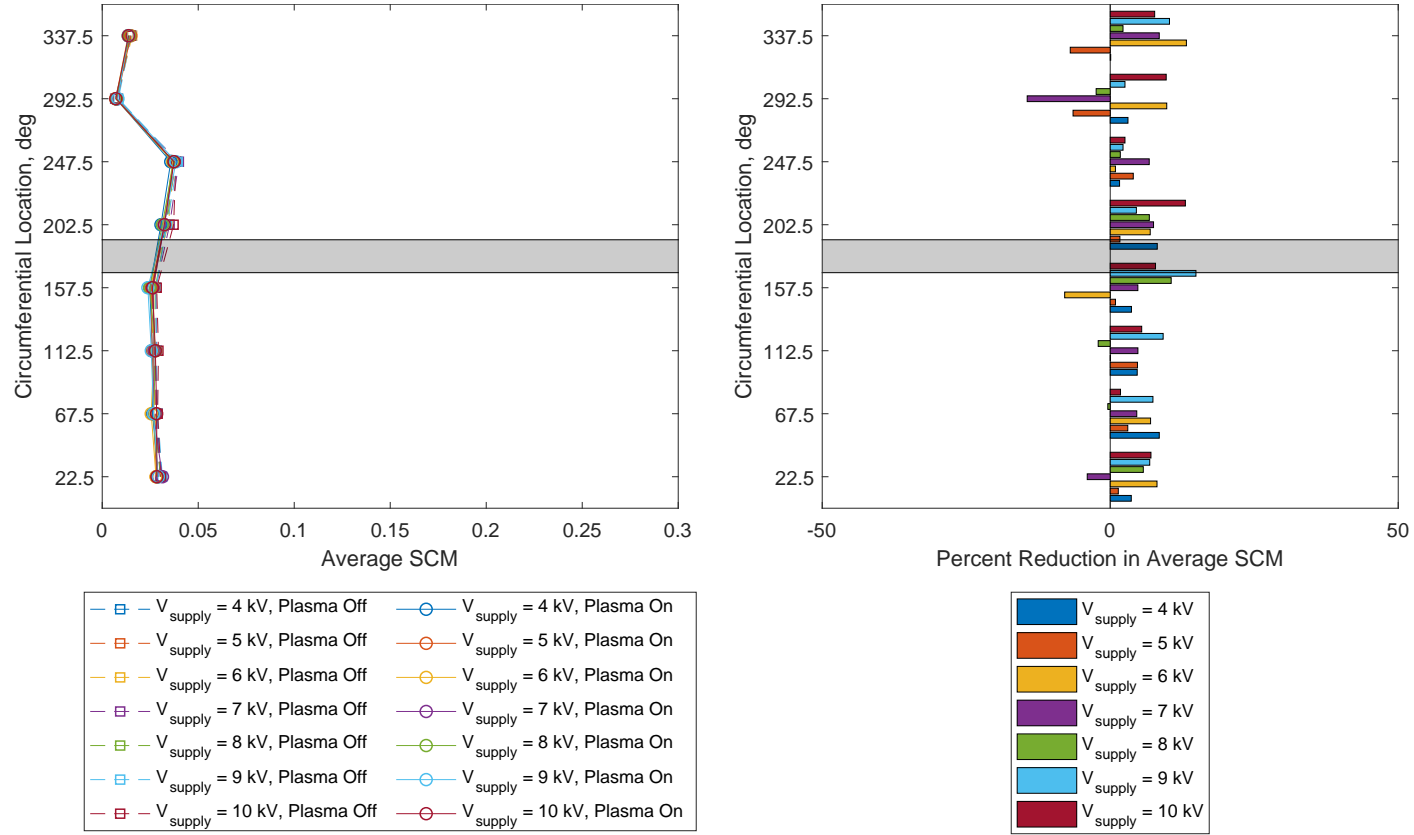


Figure 5.19. 00001000 1 segment configuration ($f = 500$ Hz, $x = 0.12c_{ax}$);
 (left) mean spatial correlation metric with plasma off and plasma on;
 (right) reduction in mean spatial correlation metric. The dark bands
 represent the locations of the actuator segments.

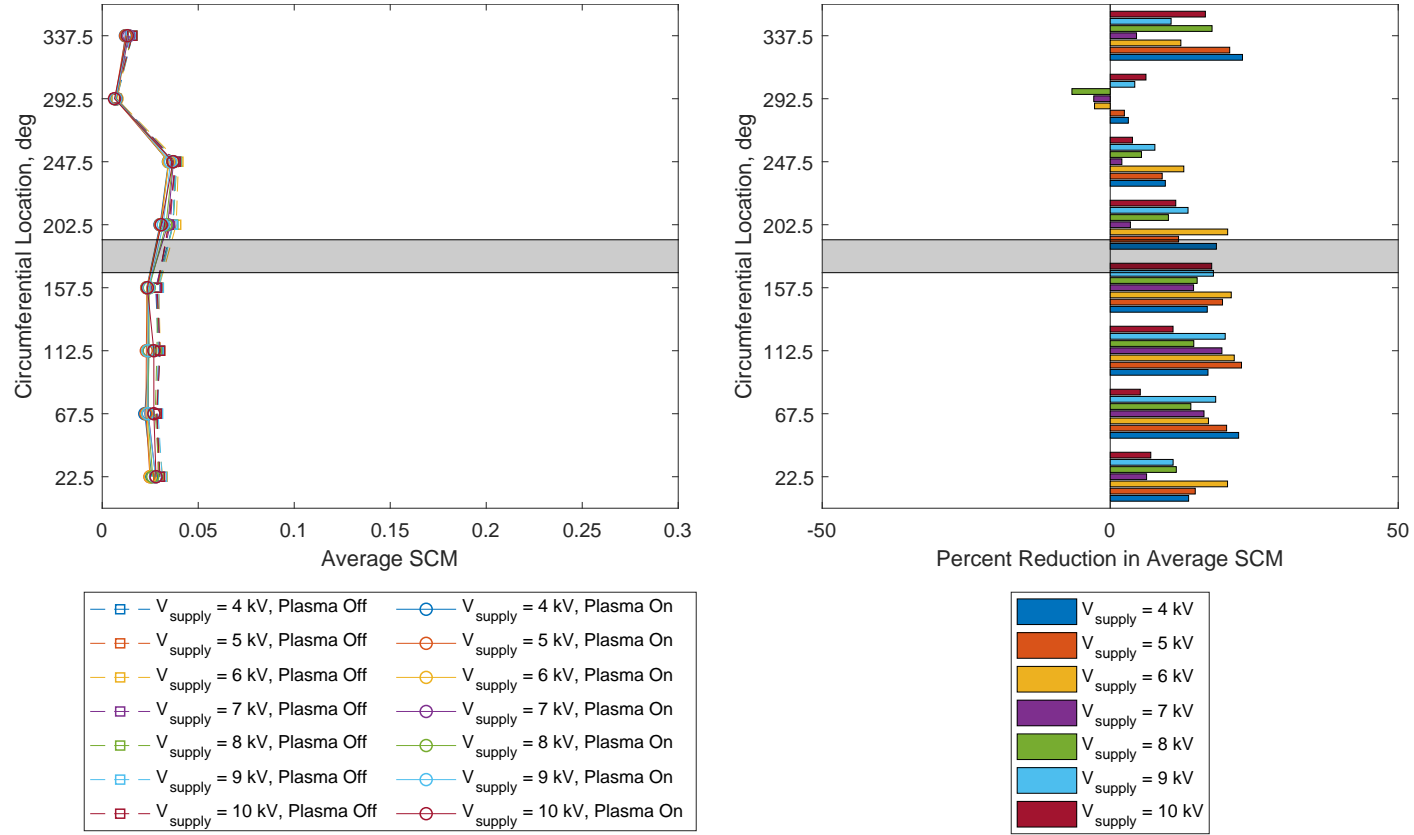


Figure 5.20. 00001000 1 segment configuration ($f = 1 \text{ kHz}$, $x = 0.12c_{ax}$);
 (left) mean spatial correlation metric with plasma off and plasma on;
 (right) reduction in mean spatial correlation metric. The dark bands
 represent the locations of the actuator segments.

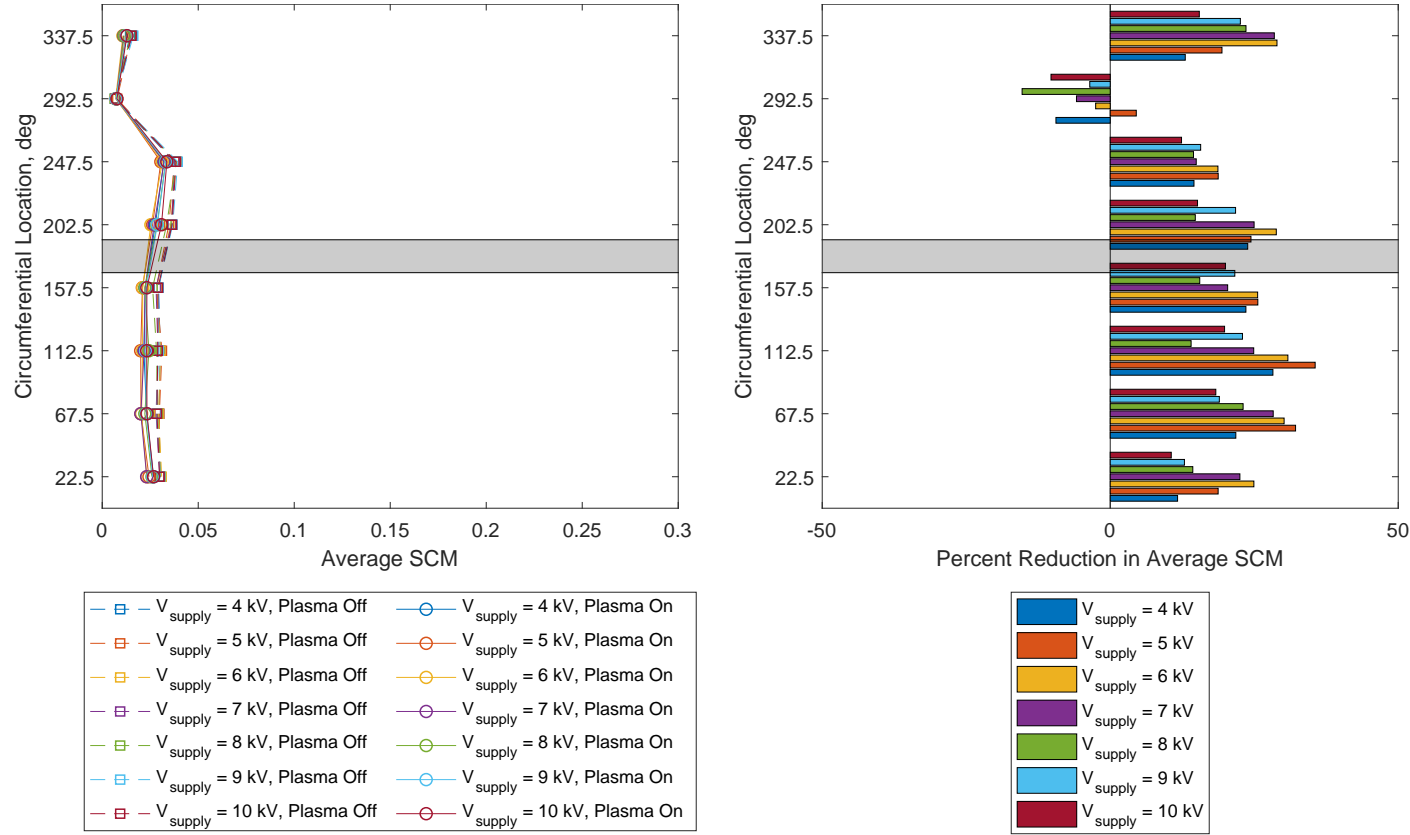


Figure 5.21. 00001000 1 segment configuration ($f = 2 \text{ kHz}$, $x = 0.12c_{ax}$);
 (left) mean spatial correlation metric with plasma off and plasma on;
 (right) reduction in mean spatial correlation metric. The dark bands
 represent the locations of the actuator segments.

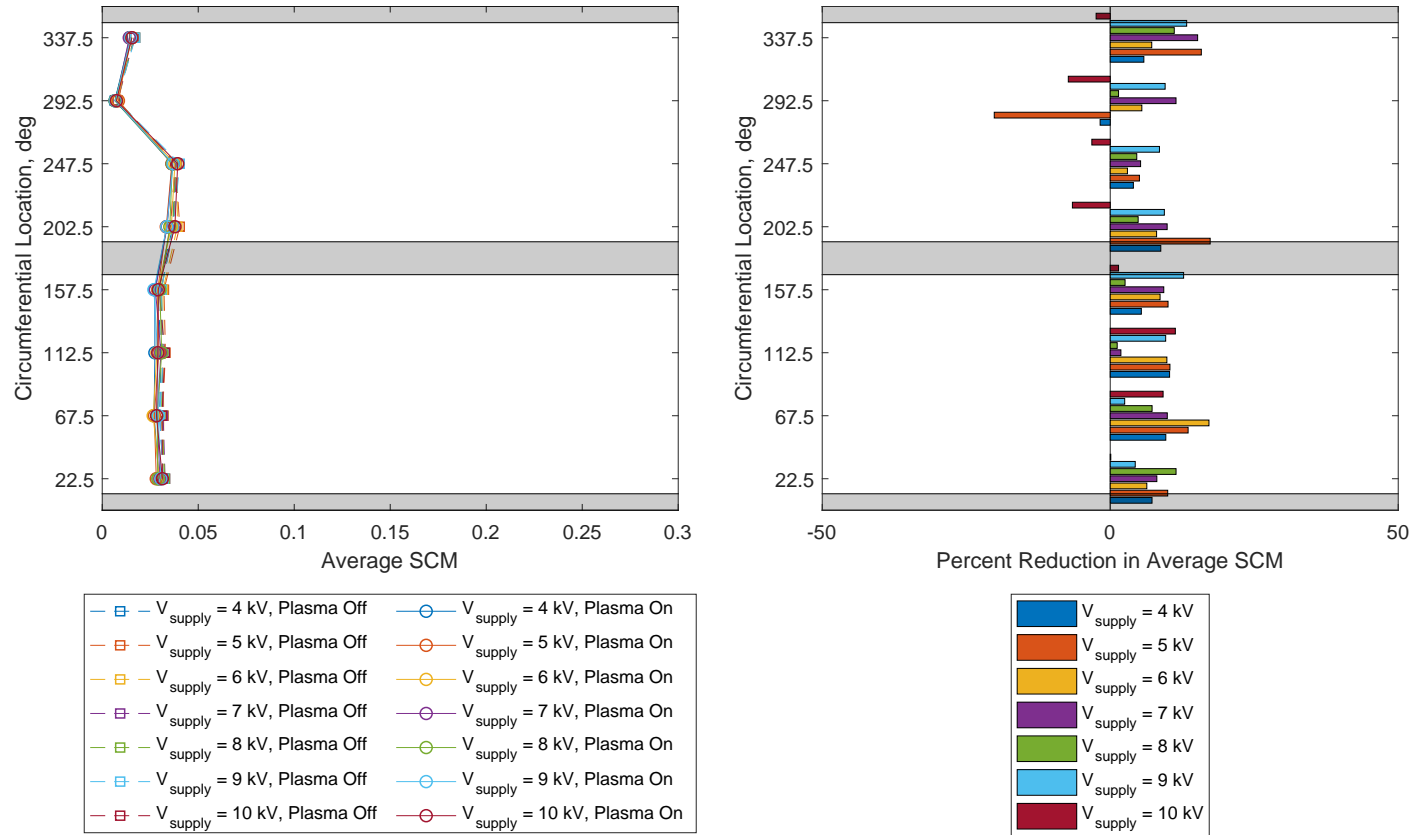


Figure 5.22. 10001000 2 segment configuration ($f = 500$ Hz, $x = 0.12c_{ax}$);
 (left) mean spatial correlation metric with plasma off and plasma on;
 (right) reduction in mean spatial correlation metric. The dark bands
 represent the locations of the actuator segments.

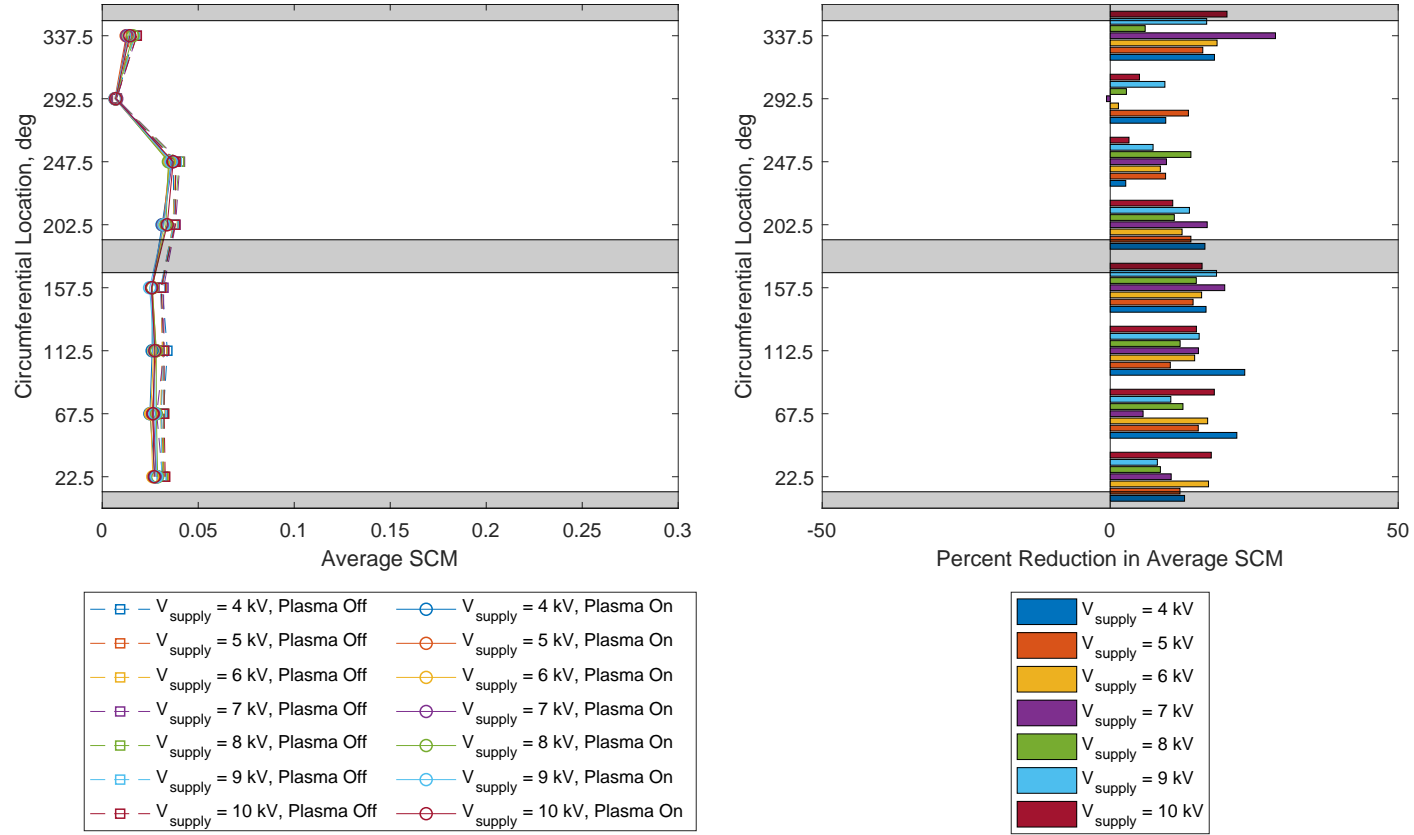


Figure 5.23. 10001000 2 segment configuration ($f = 1 \text{ kHz}$, $x = 0.12c_{ax}$);
 (left) mean spatial correlation metric with plasma off and plasma on;
 (right) reduction in mean spatial correlation metric. The dark bands
 represent the locations of the actuator segments.

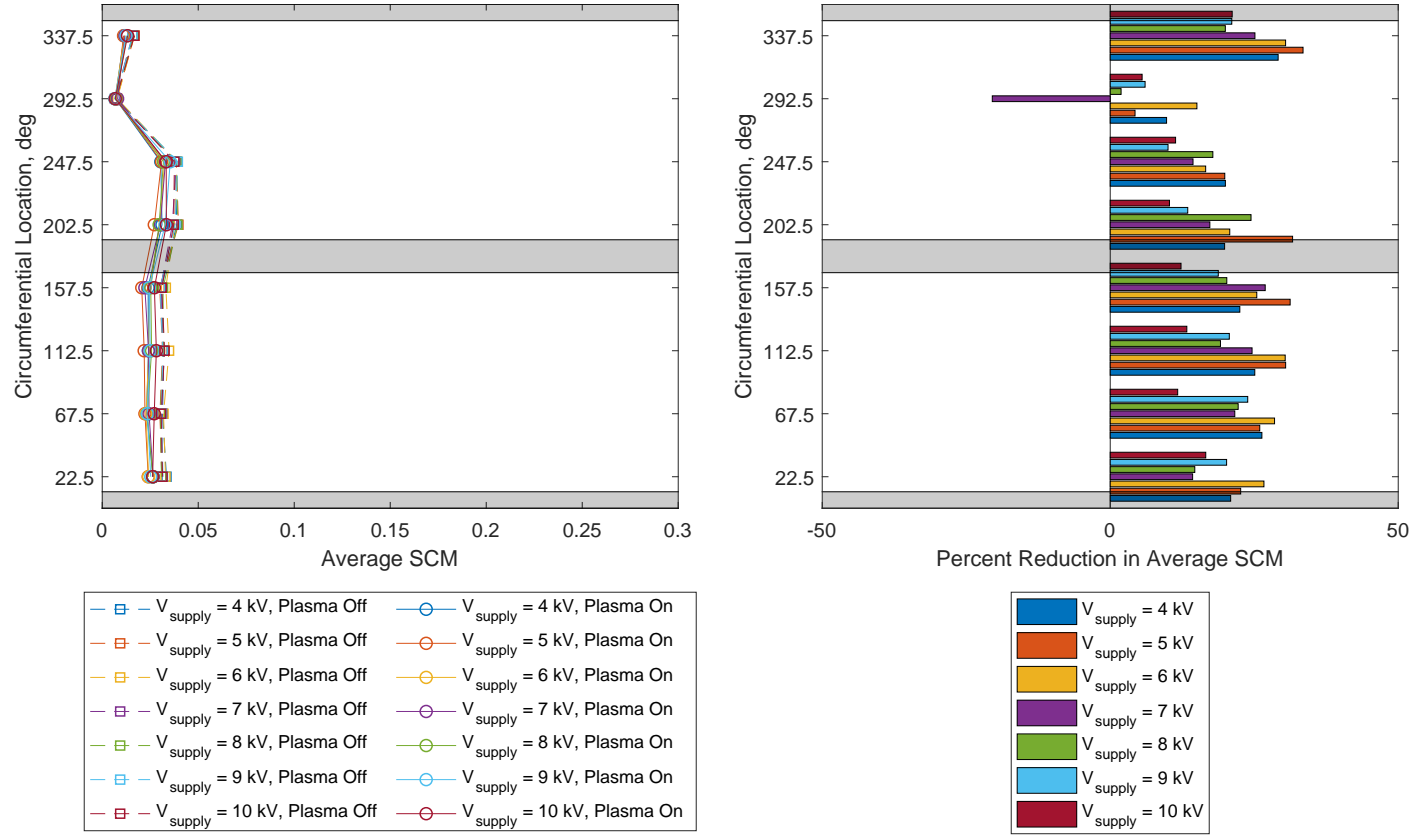


Figure 5.24. 10001000 2 segment configuration ($f = 2 \text{ kHz}$, $x = 0.12c_{ax}$);
 (left) mean spatial correlation metric with plasma off and plasma on;
 (right) reduction in mean spatial correlation metric. The dark bands
 represent the locations of the actuator segments.

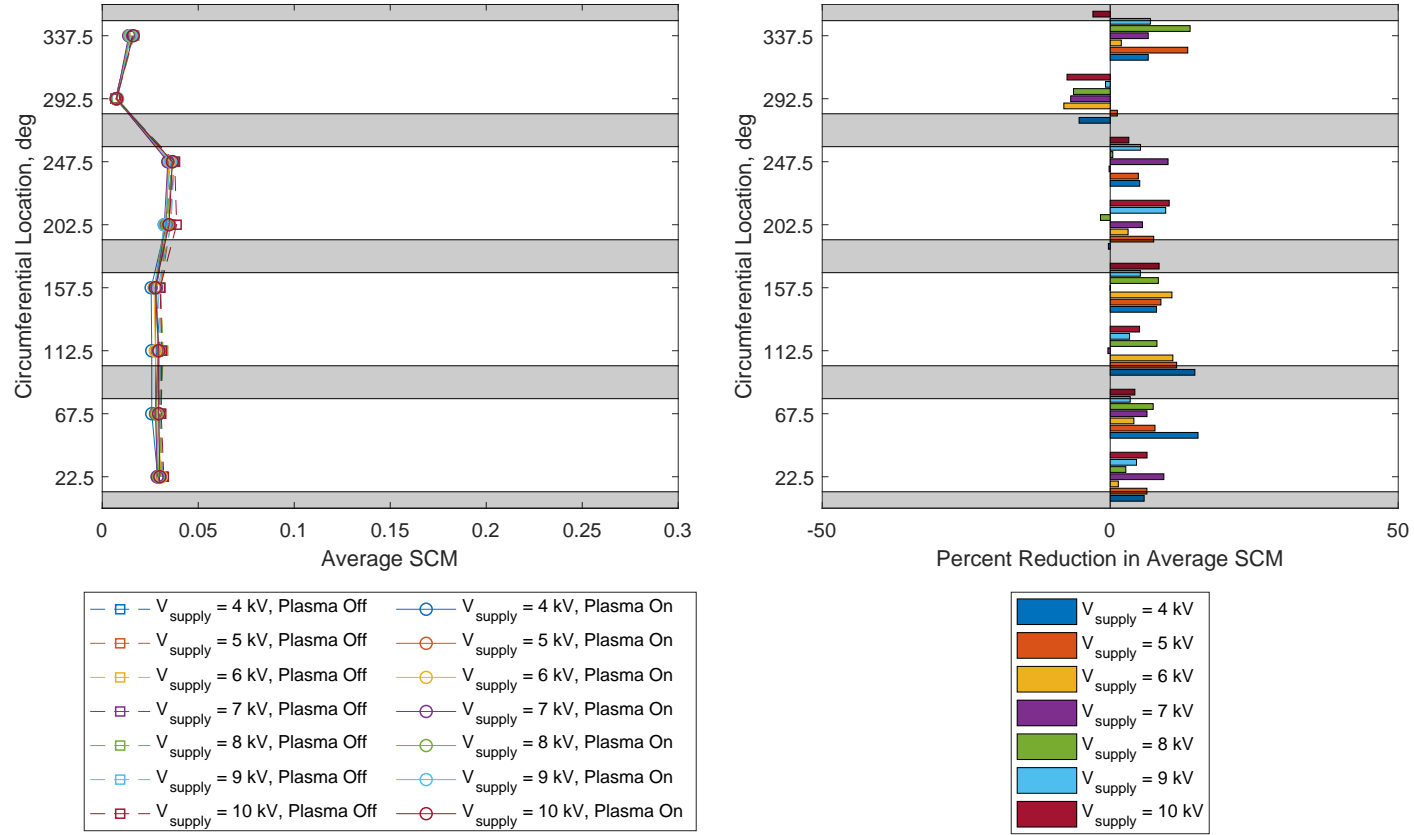


Figure 5.25. 10101010 4 segment configuration ($f = 500 \text{ Hz}$, $x = 0.12c_{ax}$);
 (left) mean spatial correlation metric with plasma off and plasma on;
 (right) reduction in mean spatial correlation metric. The dark bands
 represent the locations of the actuator segments.

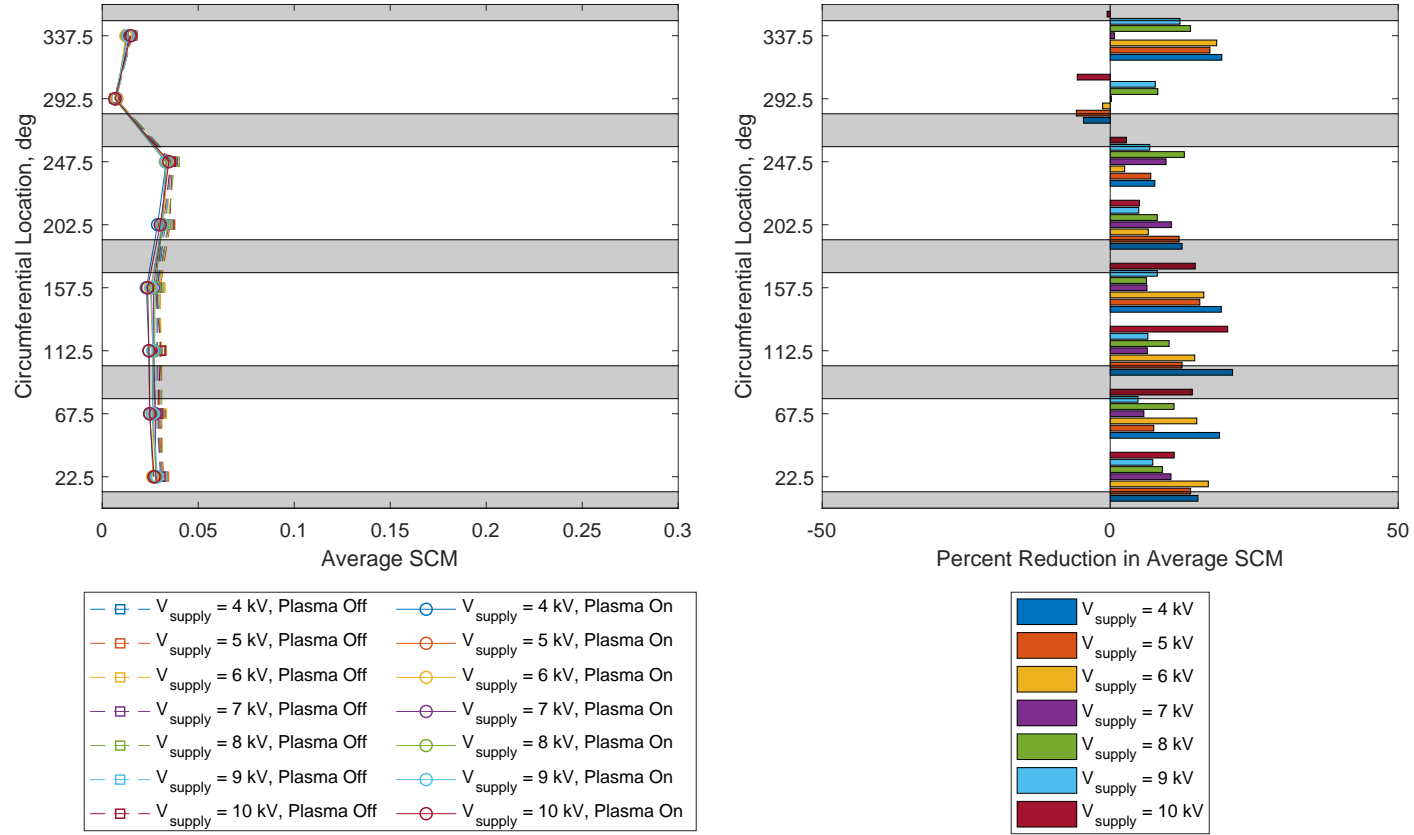


Figure 5.26. 10101010 4 segment configuration ($f = 1 \text{ kHz}$, $x = 0.12c_{ax}$);
 (left) mean spatial correlation metric with plasma off and plasma on;
 (right) reduction in mean spatial correlation metric. The dark bands
 represent the locations of the actuator segments.

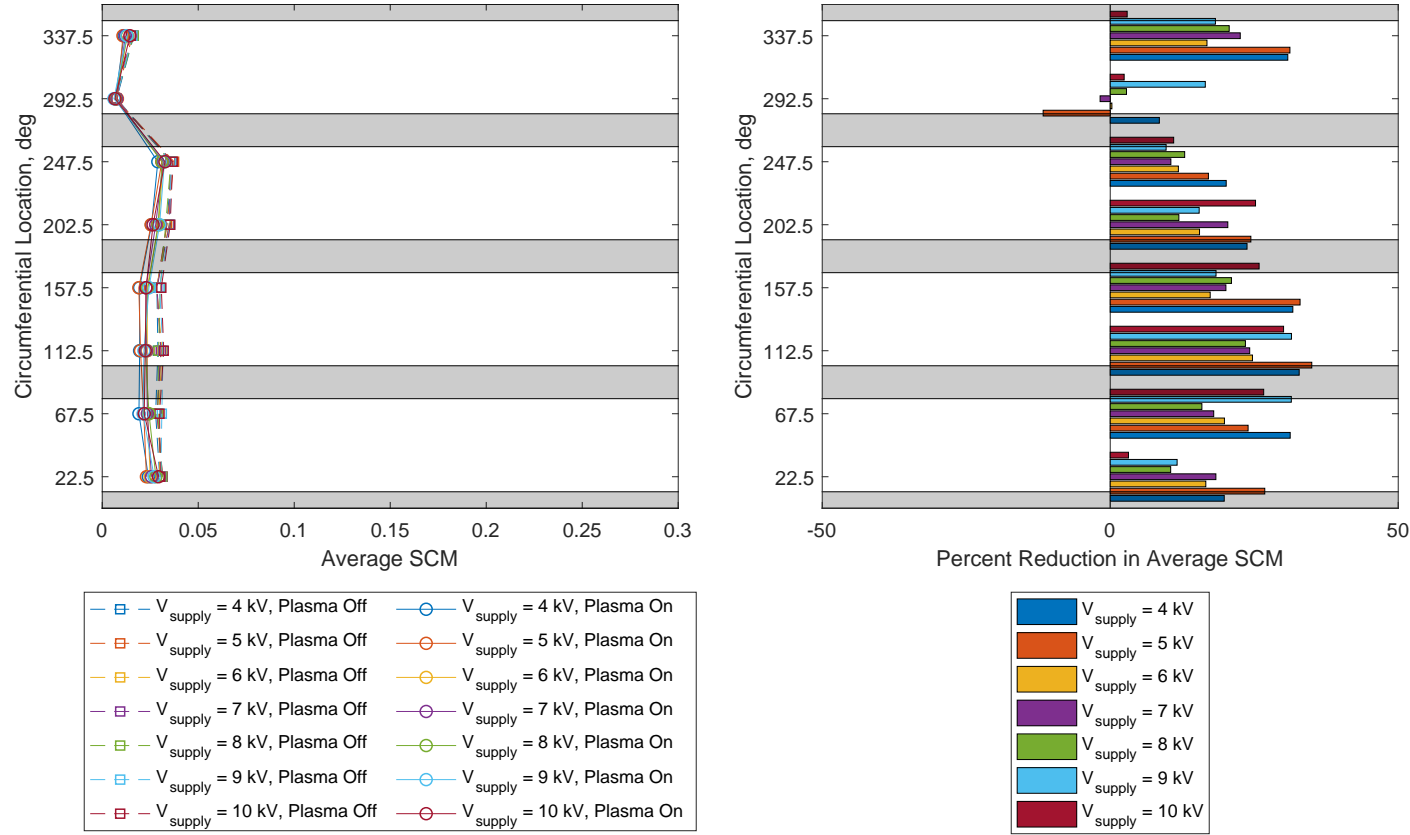


Figure 5.27. 10101010 4 segment configuration ($f = 2 \text{ kHz}$, $x = 0.12c_{ax}$);
 (left) mean spatial correlation metric with plasma off and plasma on;
 (right) reduction in mean spatial correlation metric. The dark bands
 represent the locations of the actuator segments.

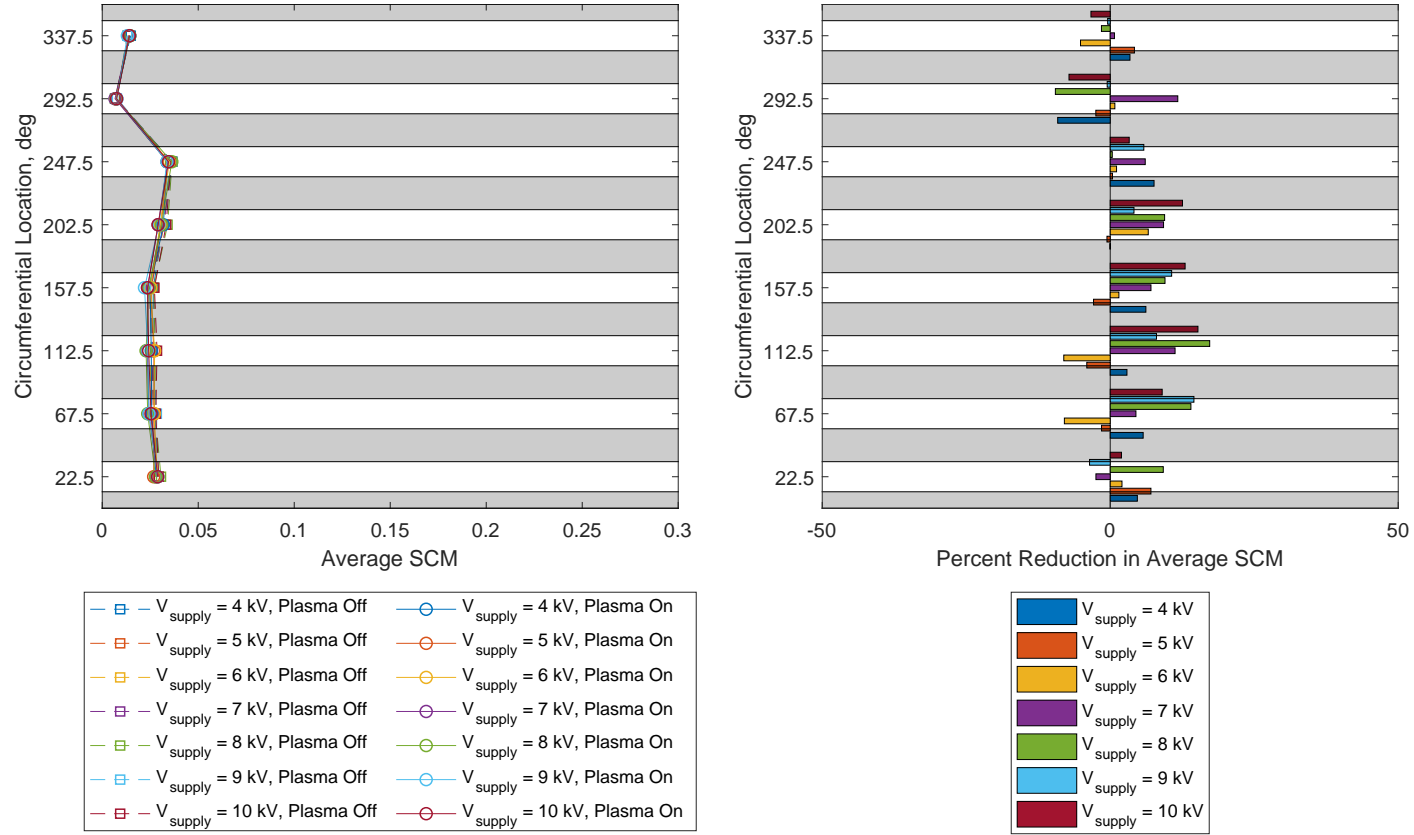


Figure 5.28. 11111111 8 segment configuration ($f = 500$ Hz, $x = 0.12c_{ax}$);
 (left) mean spatial correlation metric with plasma off and plasma on;
 (right) reduction in mean spatial correlation metric. The dark bands
 represent the locations of the actuator segments.

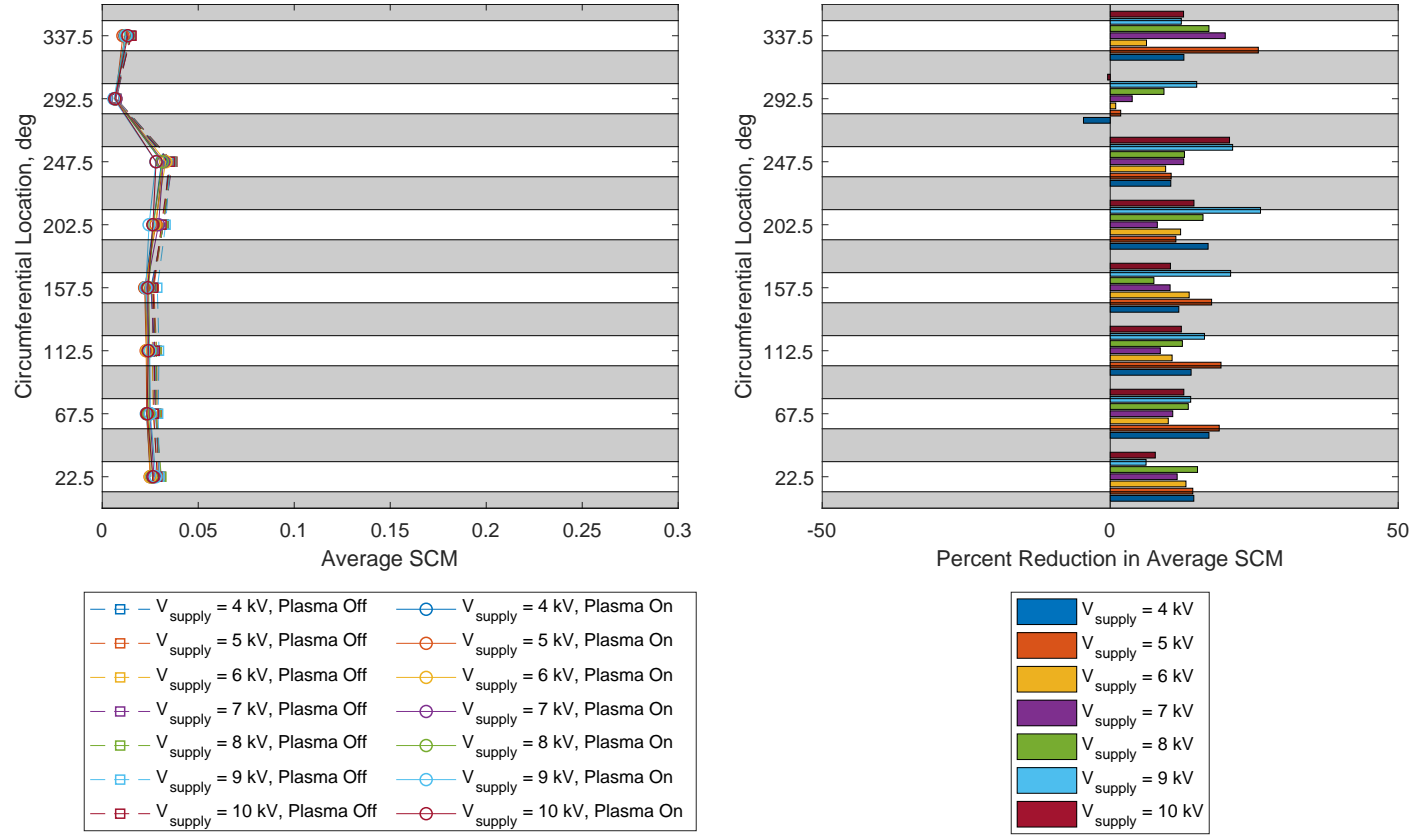


Figure 5.29. 11111111 8 segment configuration ($f = 1 \text{ kHz}$, $x = 0.12c_{ax}$);
 (left) mean spatial correlation metric with plasma off and plasma on;
 (right) reduction in mean spatial correlation metric. The dark bands
 represent the locations of the actuator segments.

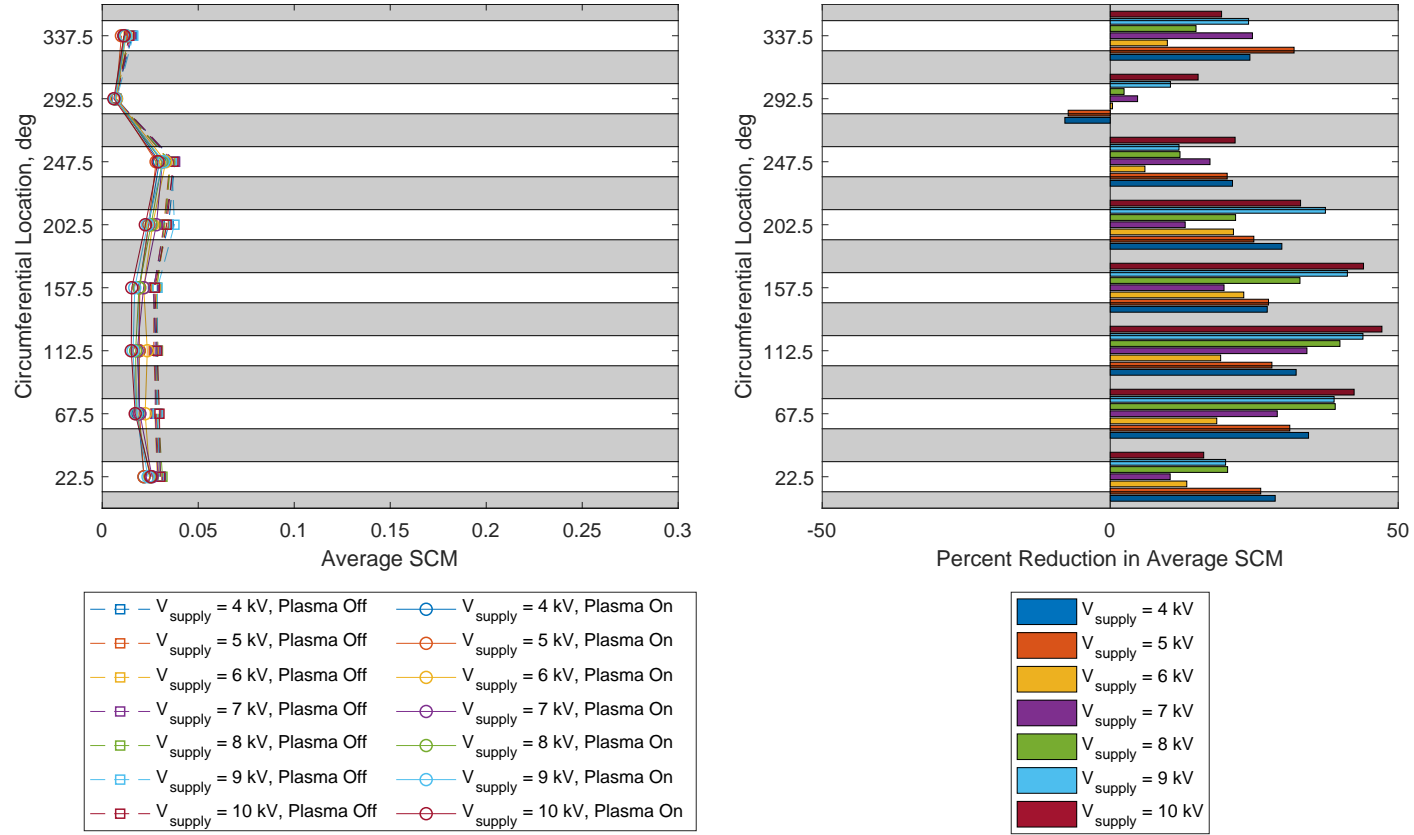


Figure 5.30. 11111111 8 segment configuration ($f = 2 \text{ kHz}$, $x = 0.12c_{ax}$);
 (left) mean spatial correlation metric with plasma off and plasma on;
 (right) reduction in mean spatial correlation metric. The dark bands
 represent the locations of the actuator segments.

5.3.3 Actuators at $x = 0.51c_{ax}$

The other local maximum in stall margin improvement found by Houghton and Day [18] occurred for a location close to the midchord. In their study, they noted that this location resulted in “the greatest stall margin improvement with the least efficiency loss.” On the left side of Figures 5.31–5.42, the mean of the spatial correlation metric is calculated for a plasma-off and plasma-on time window and plotted as a function of location for several different pulse amplitudes. The reduction in this mean due to plasma actuation is plotted on the right side.

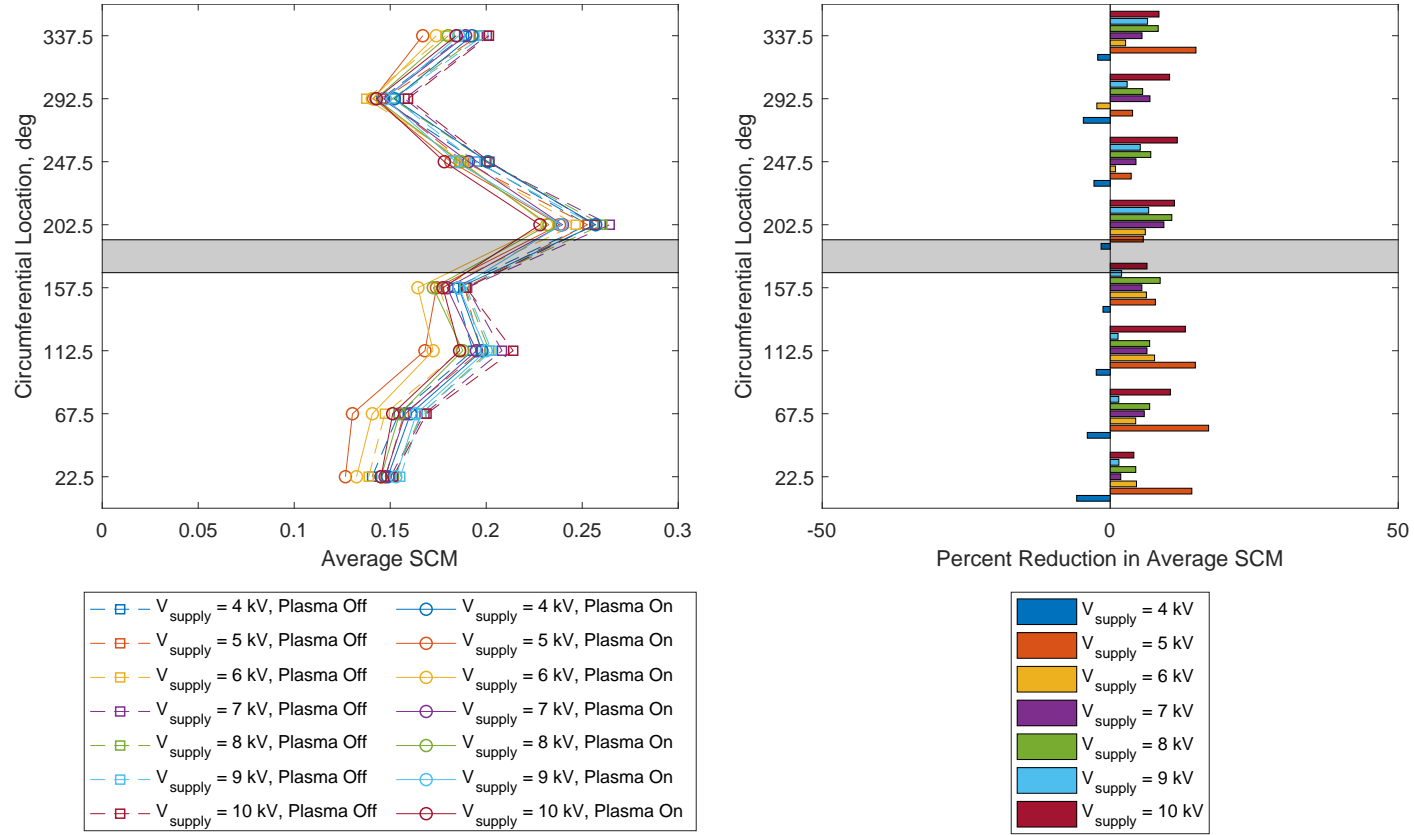


Figure 5.31. 00001000 1 segment configuration ($f = 500$ Hz, $x = 0.51c_{ax}$);
 (left) mean spatial correlation metric with plasma off and plasma on;
 (right) reduction in mean spatial correlation metric. The dark bands
 represent the locations of the actuator segments.

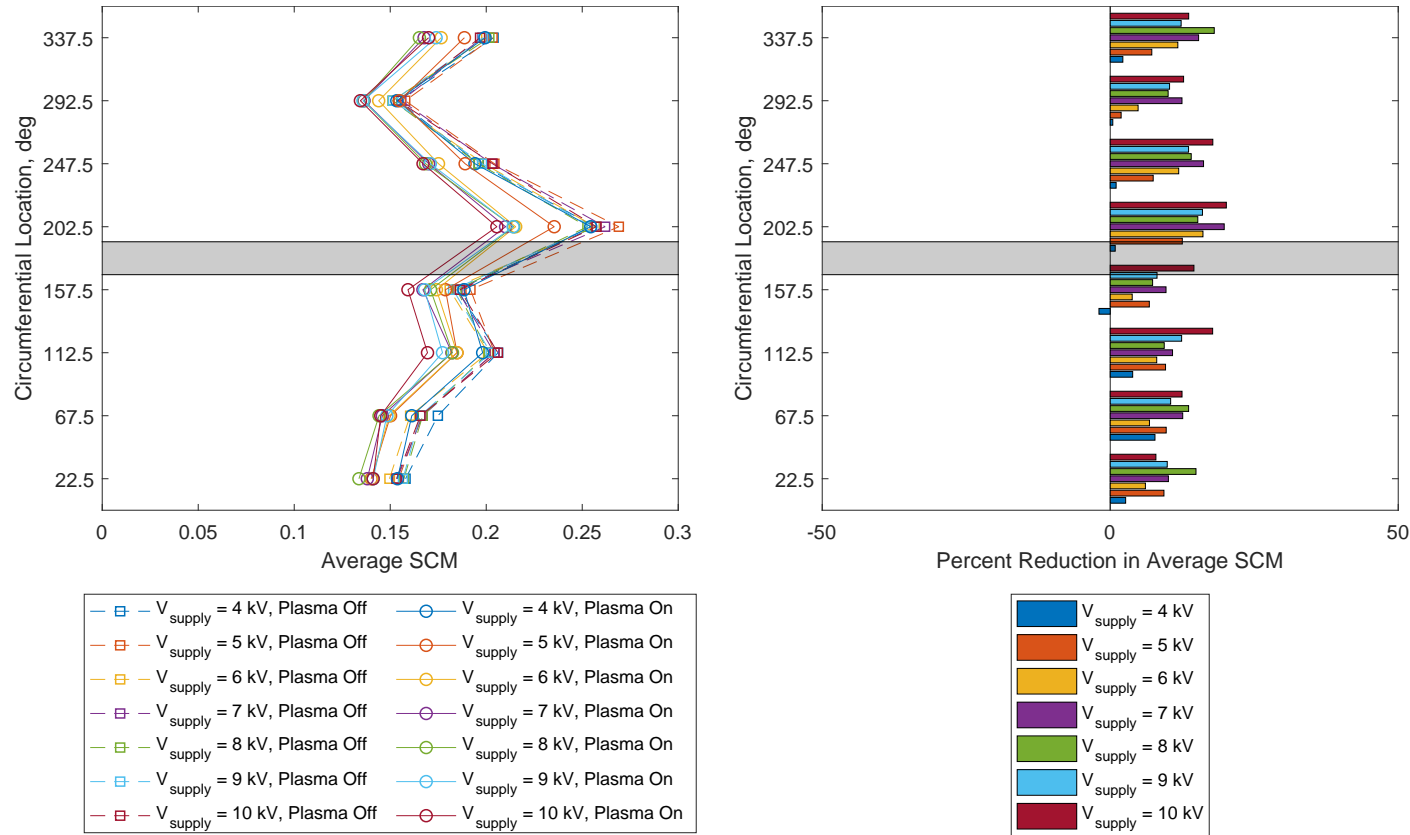


Figure 5.32. 00001000 1 segment configuration ($f = 1 \text{ kHz}$, $x = 0.51c_{ax}$);
 (left) mean spatial correlation metric with plasma off and plasma on;
 (right) reduction in mean spatial correlation metric. The dark bands
 represent the locations of the actuator segments.

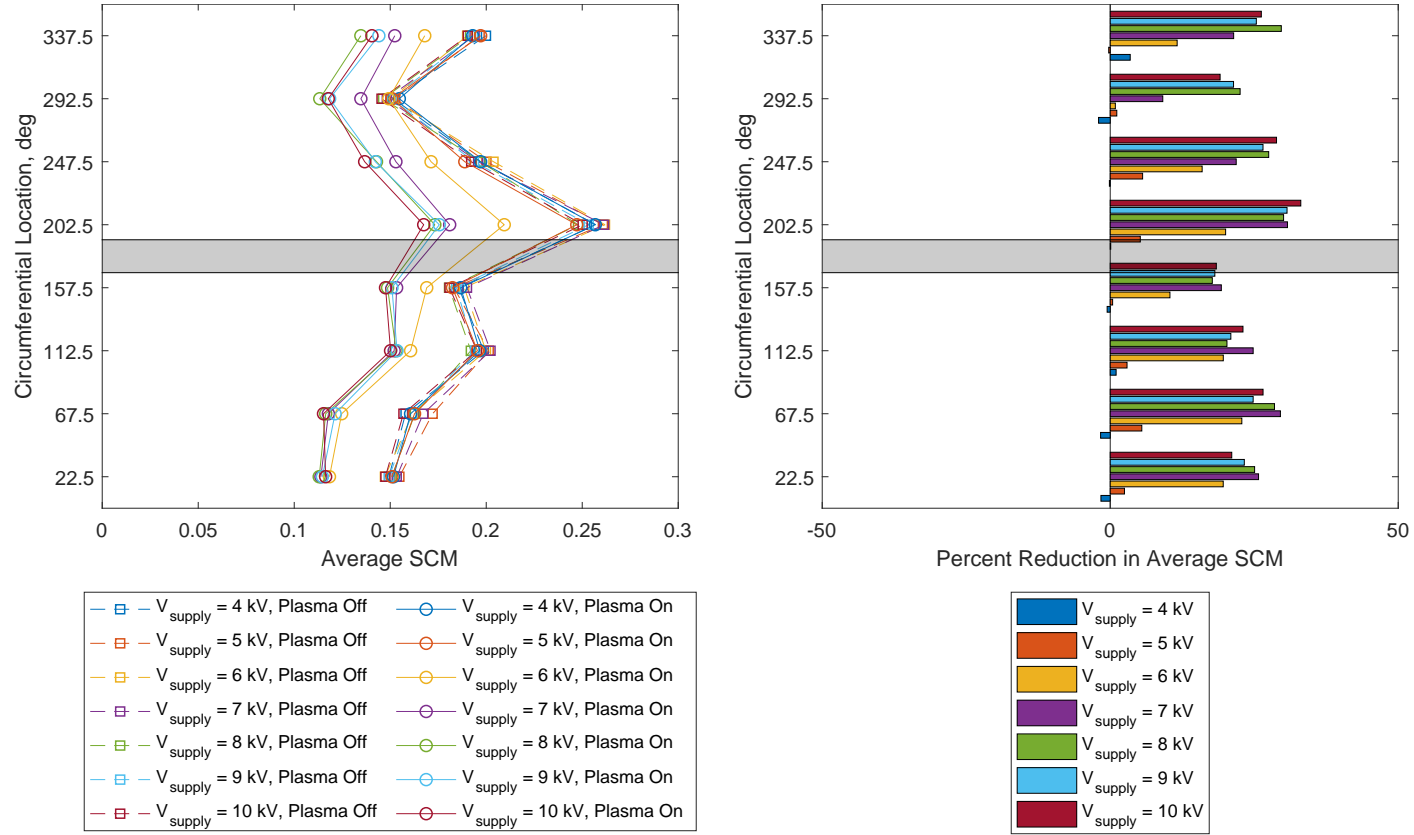


Figure 5.33. 00001000 1 segment configuration ($f = 2 \text{ kHz}$, $x = 0.51c_{ax}$);
 (left) mean spatial correlation metric with plasma off and plasma on;
 (right) reduction in mean spatial correlation metric. The dark bands
 represent the locations of the actuator segments.

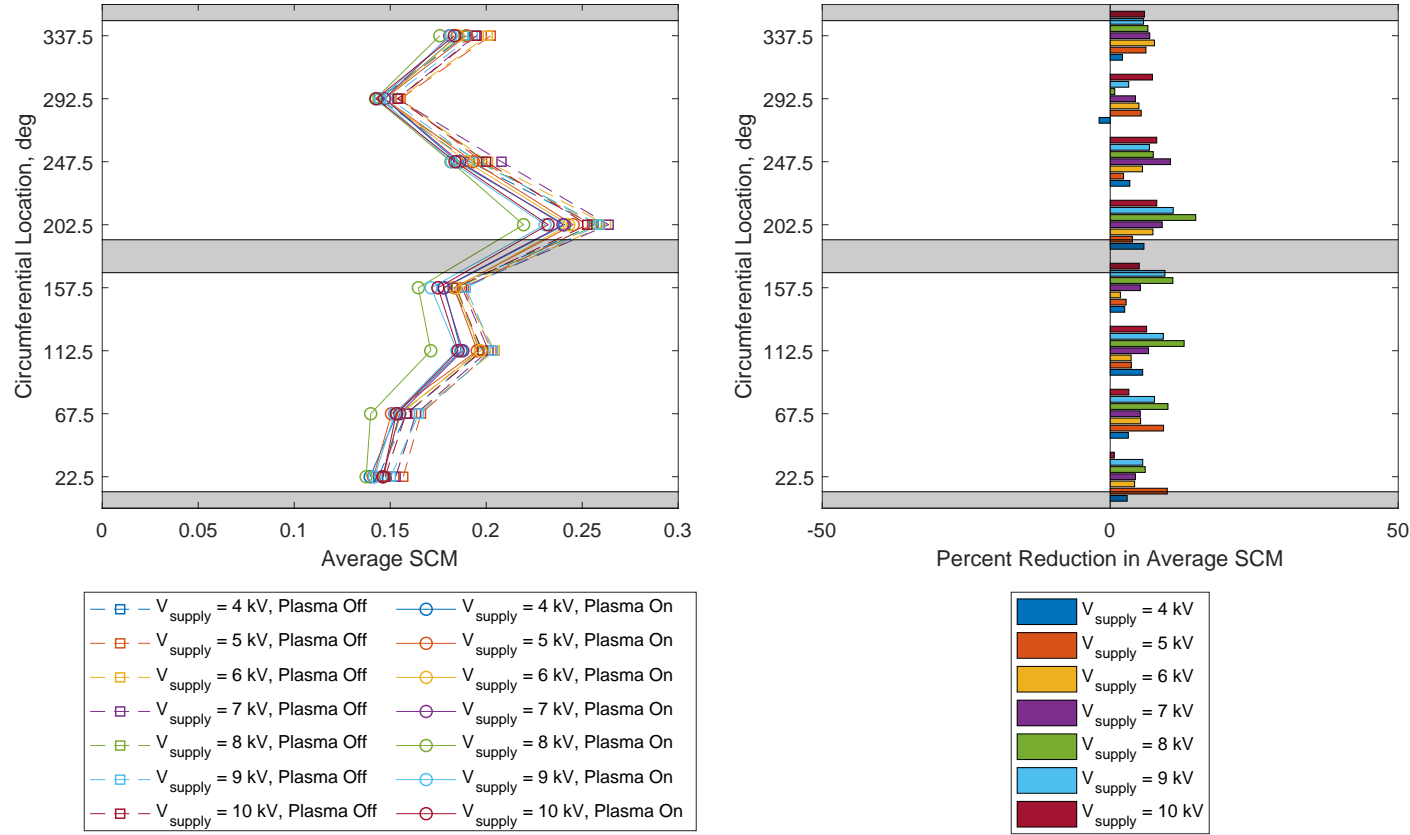


Figure 5.34. 10001000 2 segment configuration ($f = 500$ Hz, $x = 0.51c_{ax}$);
 (left) mean spatial correlation metric with plasma off and plasma on;
 (right) reduction in mean spatial correlation metric. The dark bands
 represent the locations of the actuator segments.

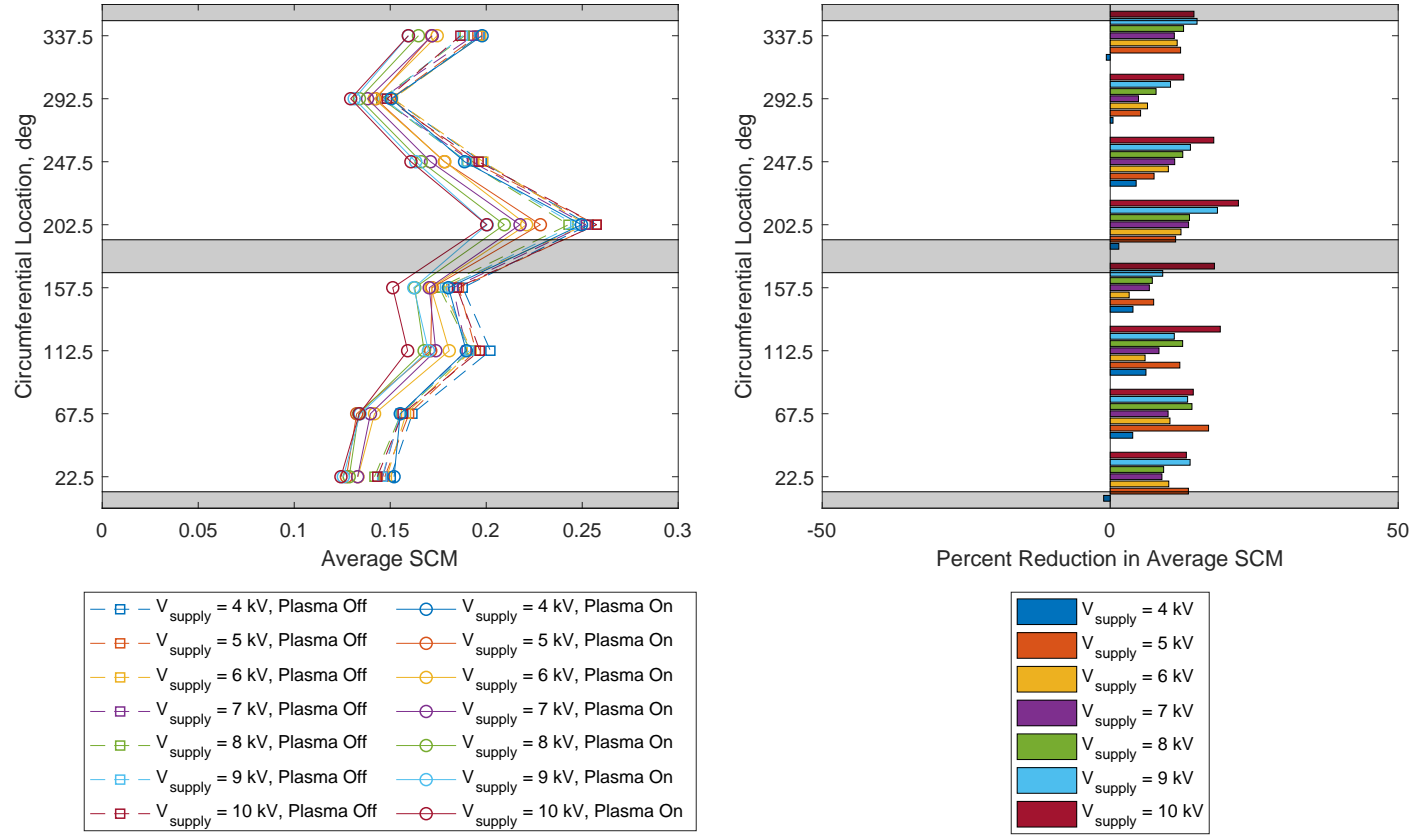


Figure 5.35. 10001000 2 segment configuration ($f = 1 \text{ kHz}$, $x = 0.51c_{ax}$);
 (left) mean spatial correlation metric with plasma off and plasma on;
 (right) reduction in mean spatial correlation metric. The dark bands
 represent the locations of the actuator segments.

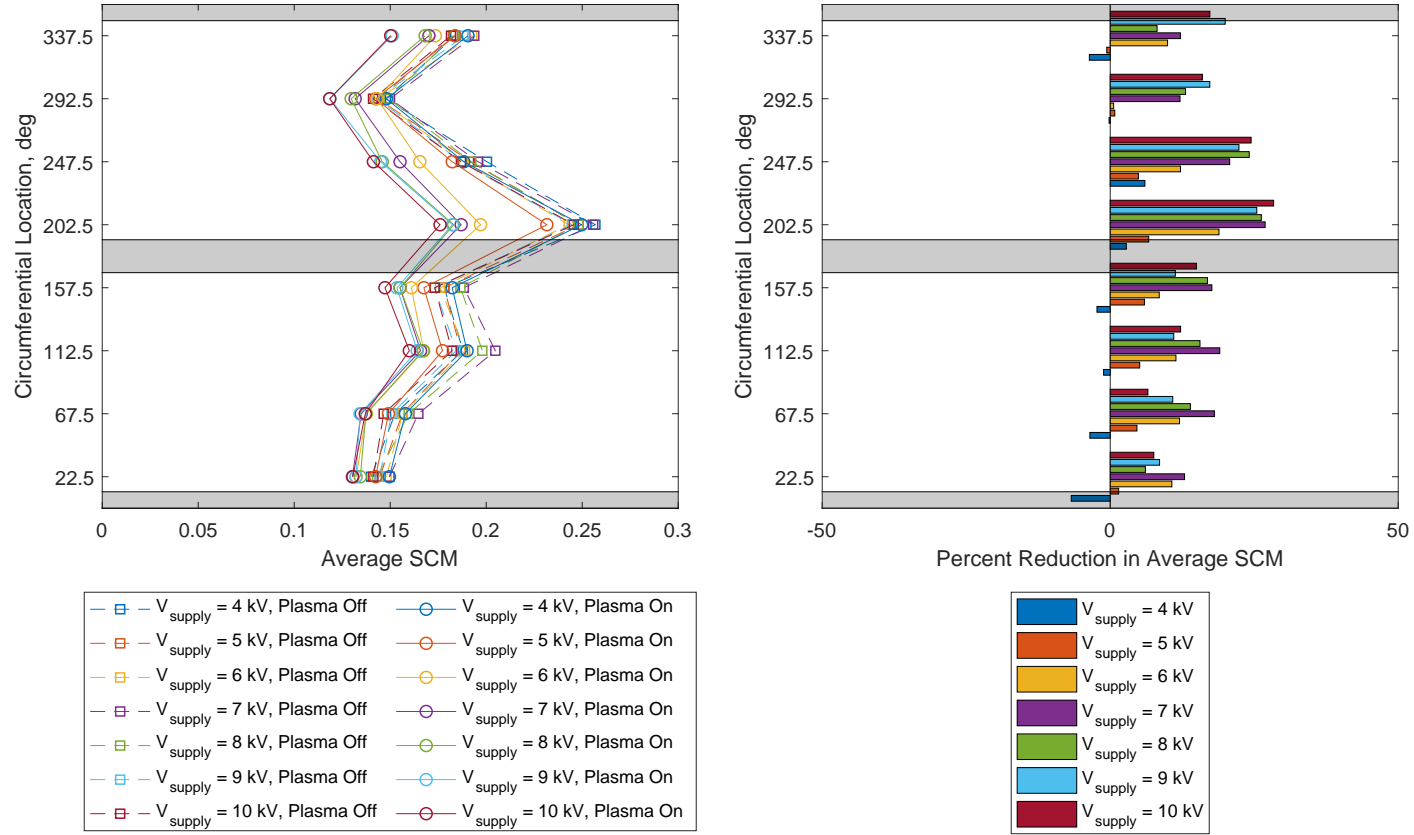


Figure 5.36. 10001000 2 segment configuration ($f = 2 \text{ kHz}$, $x = 0.51c_{ax}$);
 (left) mean spatial correlation metric with plasma off and plasma on;
 (right) reduction in mean spatial correlation metric. The dark bands
 represent the locations of the actuator segments.

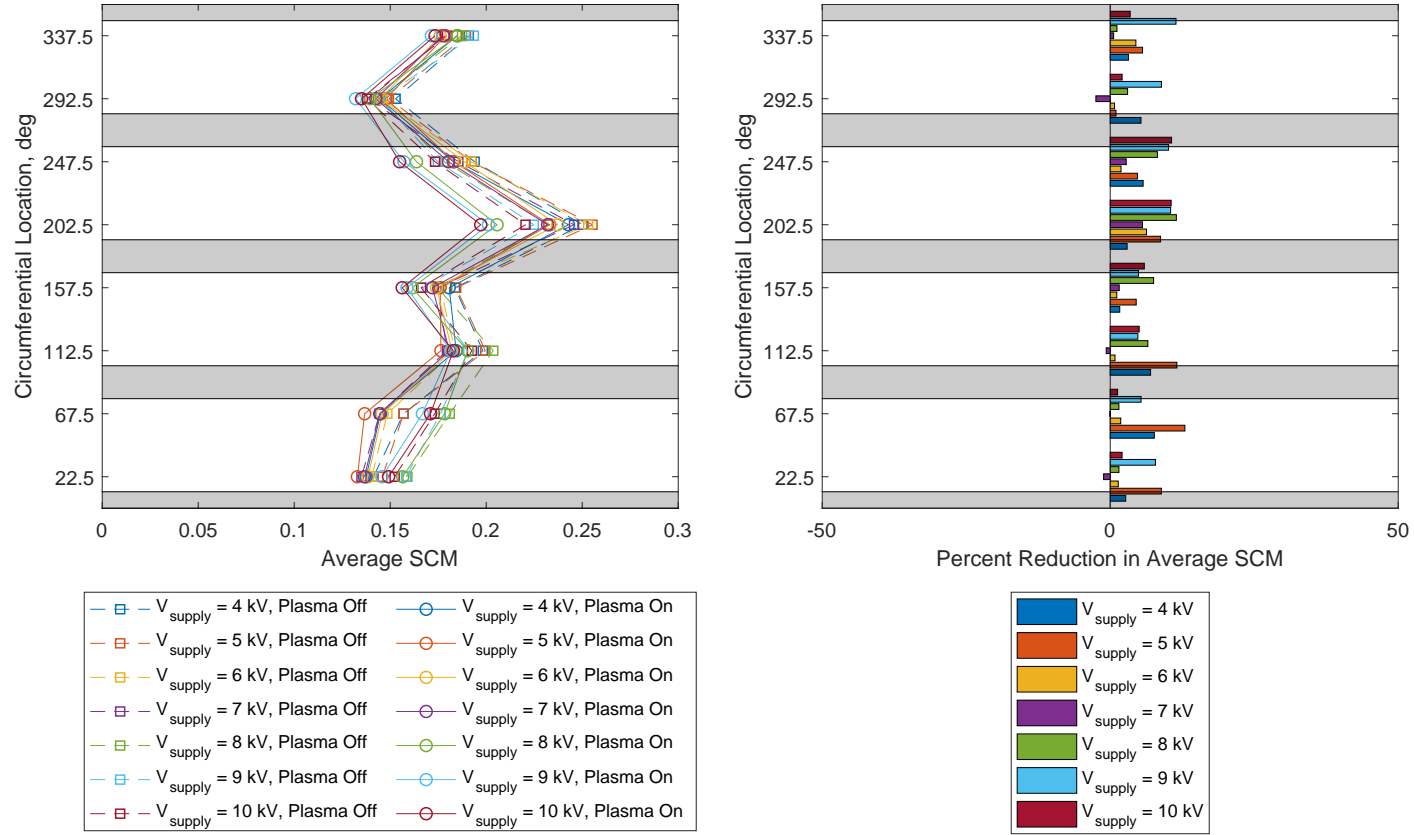


Figure 5.37. 10101010 4 segment configuration ($f = 500 \text{ Hz}$, $x = 0.51c_{ax}$);
 (left) mean spatial correlation metric with plasma off and plasma on;
 (right) reduction in mean spatial correlation metric. The dark bands
 represent the locations of the actuator segments.

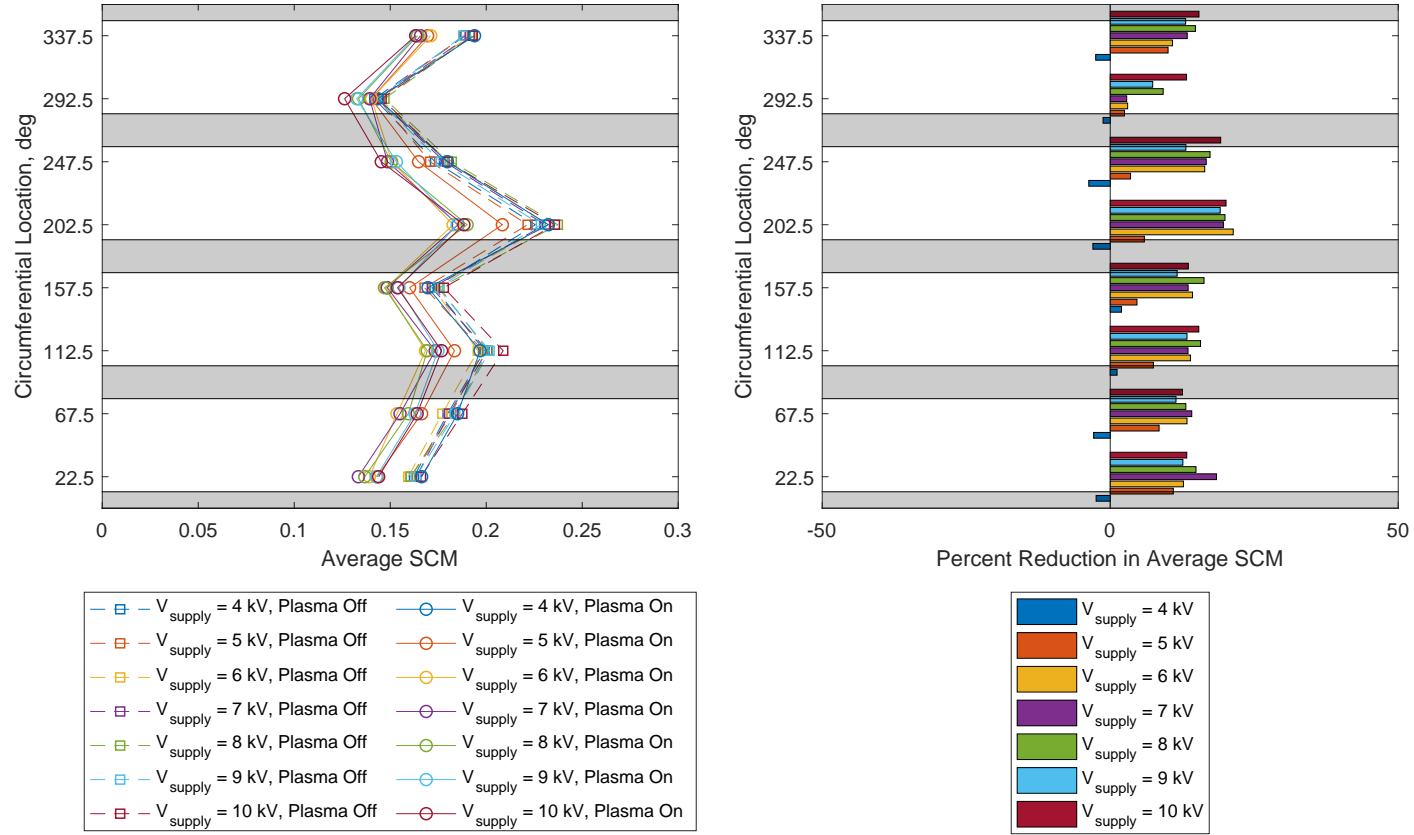


Figure 5.38. 10101010 4 segment configuration ($f = 1 \text{ kHz}$, $x = 0.51c_{ax}$);
 (left) mean spatial correlation metric with plasma off and plasma on;
 (right) reduction in mean spatial correlation metric. The dark bands
 represent the locations of the actuator segments.

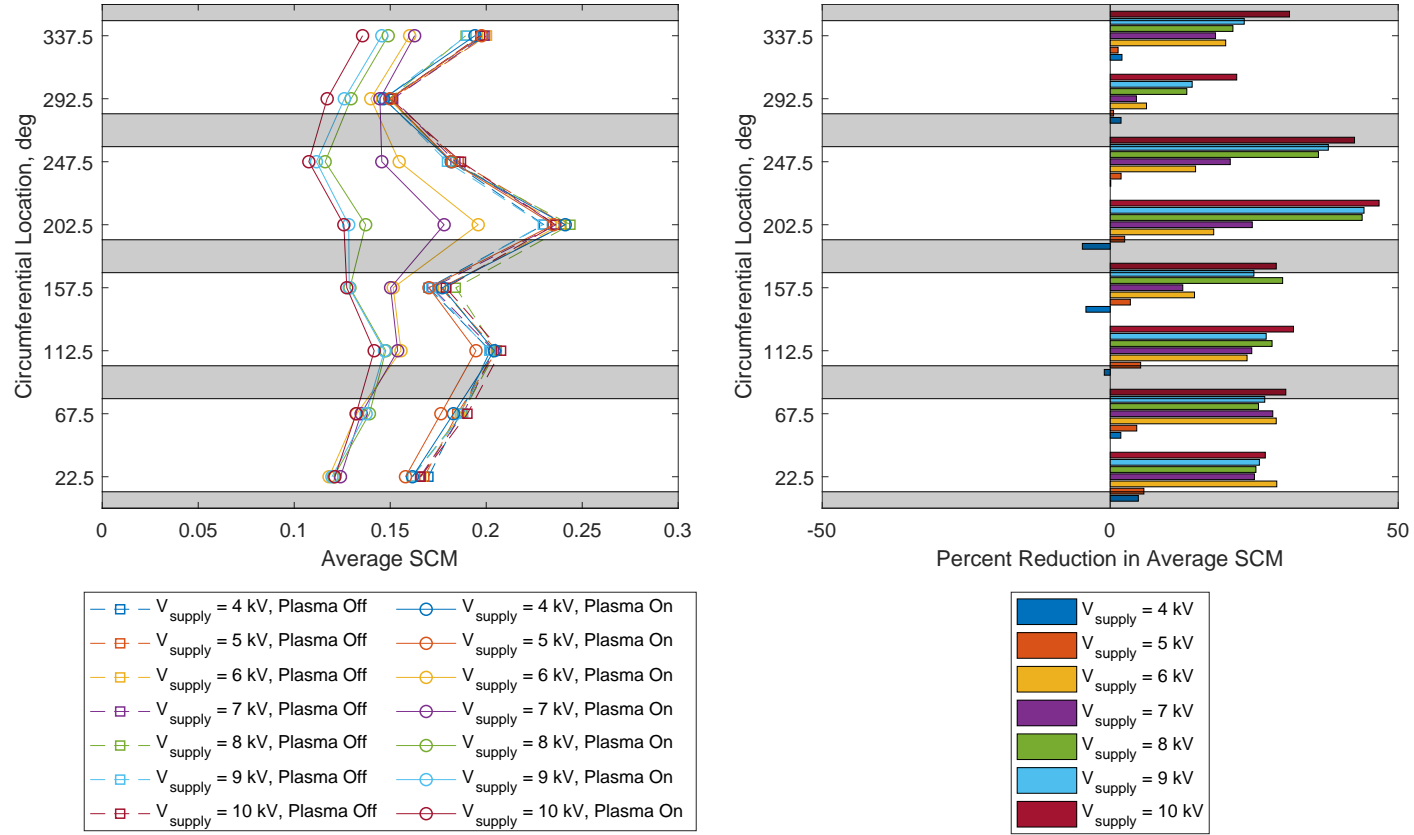


Figure 5.39. 10101010 4 segment configuration ($f = 2 \text{ kHz}$, $x = 0.51c_{ax}$);
 (left) mean spatial correlation metric with plasma off and plasma on;
 (right) reduction in mean spatial correlation metric. The dark bands
 represent the locations of the actuator segments.

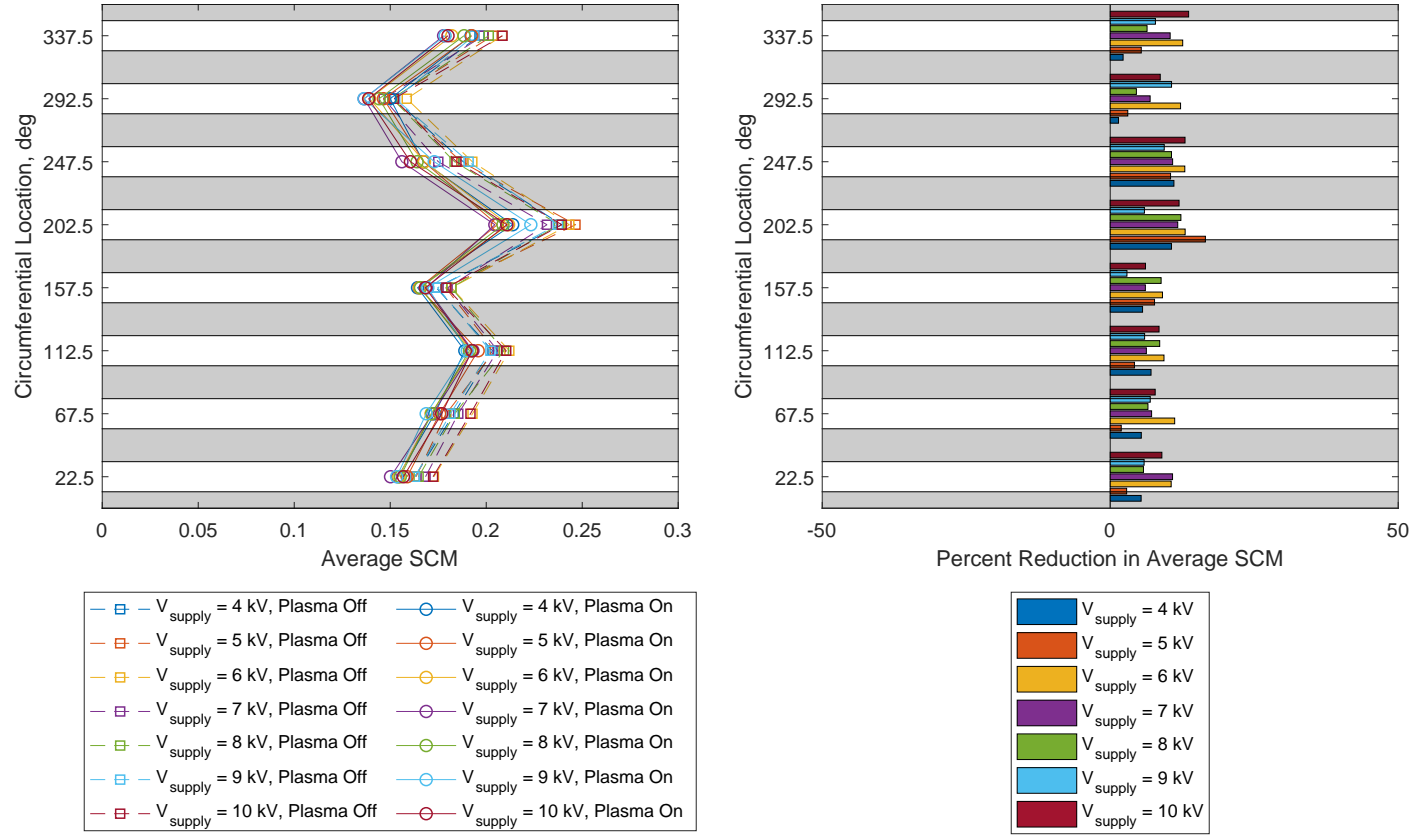


Figure 5.40. 11111111 8 segment configuration ($f = 500$ Hz, $x = 0.51c_{ax}$);
 (left) mean spatial correlation metric with plasma off and plasma on;
 (right) reduction in mean spatial correlation metric. The dark bands
 represent the locations of the actuator segments.

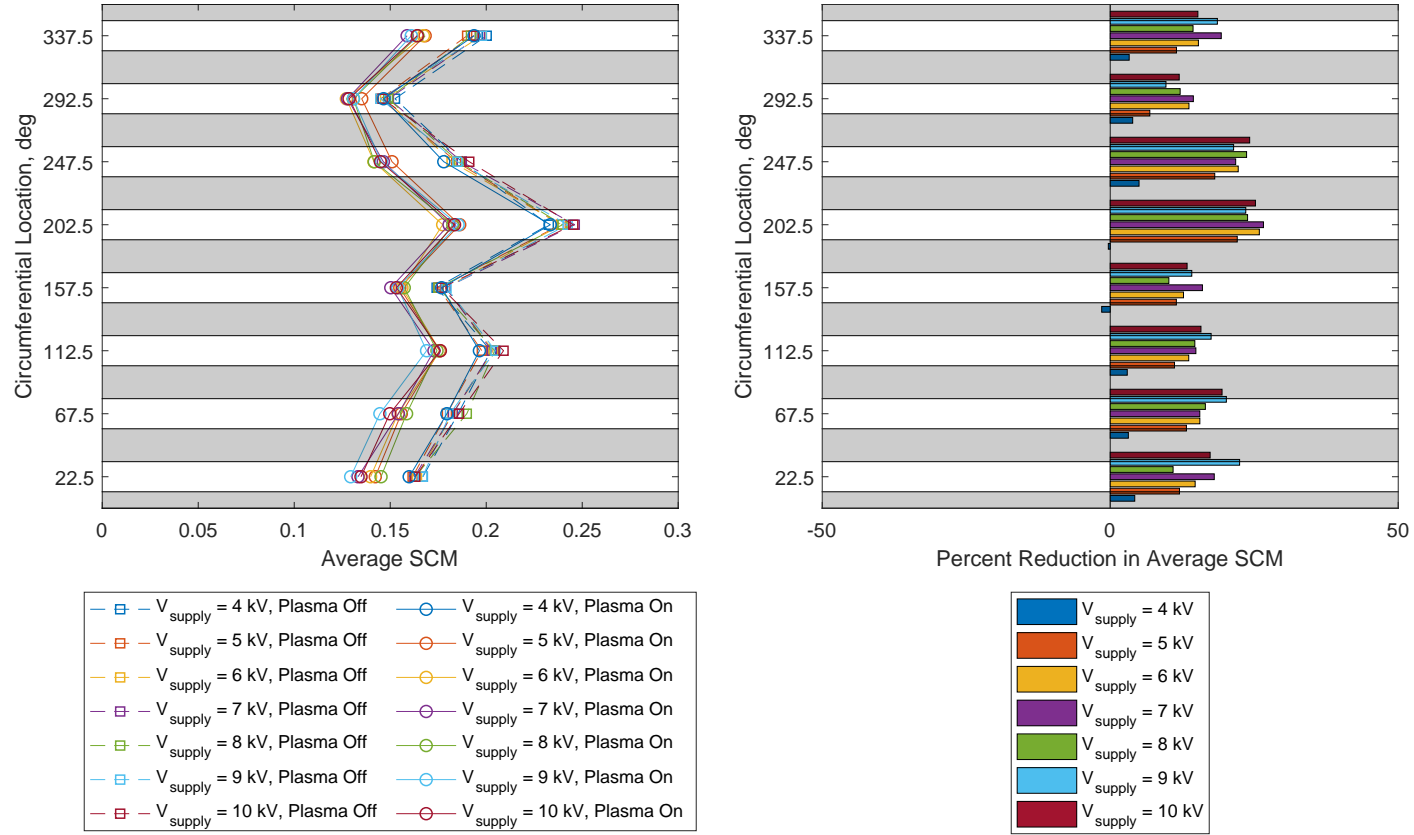


Figure 5.41. 11111111 8 segment configuration ($f = 1 \text{ kHz}$, $x = 0.51c_{ax}$);
 (left) mean spatial correlation metric with plasma off and plasma on;
 (right) reduction in mean spatial correlation metric. The dark bands
 represent the locations of the actuator segments.

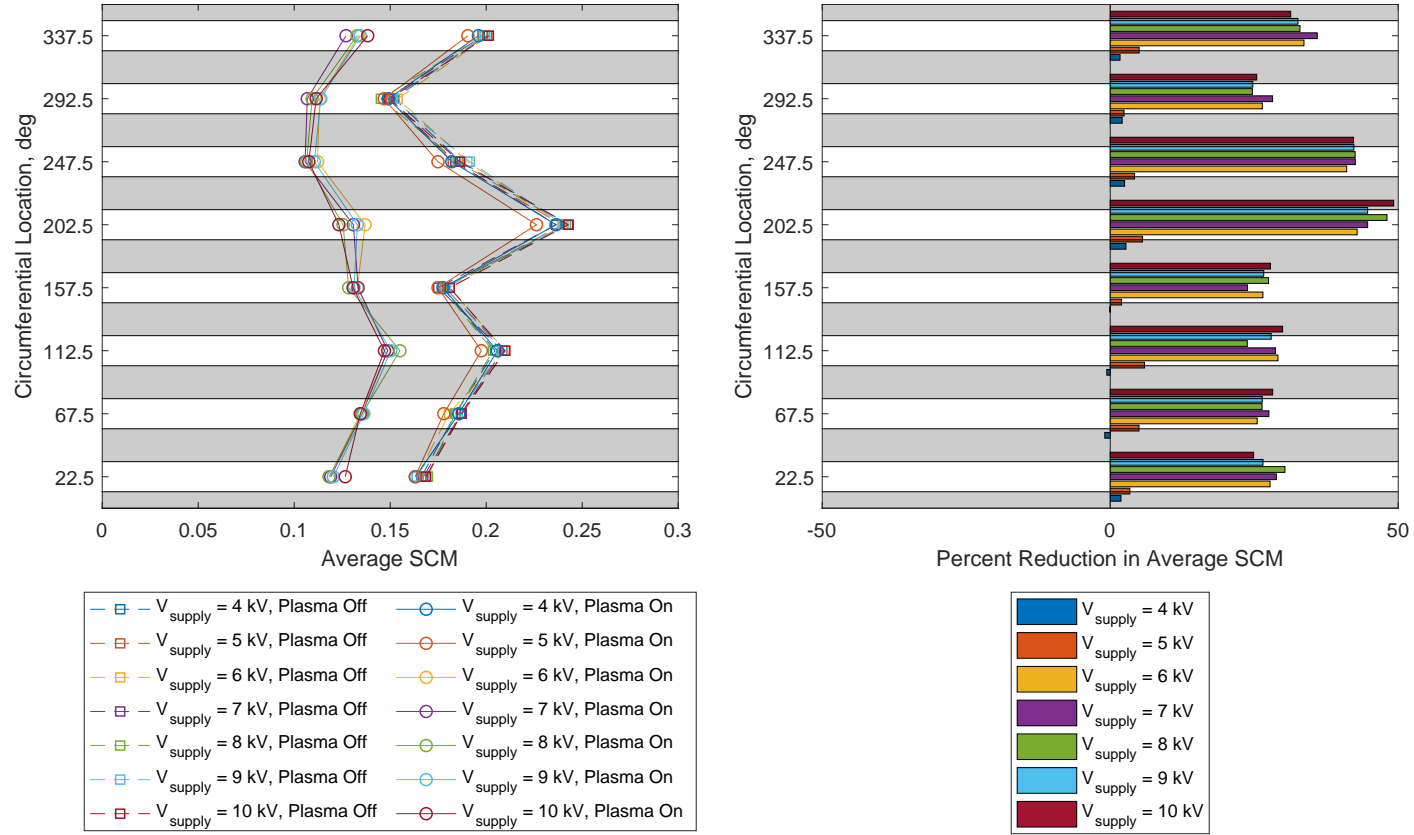


Figure 5.42. 11111111 8 segment configuration ($f = 2\text{ kHz}$, $x = 0.51c_{ax}$);
 (left) mean spatial correlation metric with plasma off and plasma on;
 (right) reduction in mean spatial correlation metric. The dark bands
 represent the locations of the actuator segments.

5.4 Fan Performance Curve Measurements

The performance of an axial fan can be visualized for a variety of operating conditions on a fan map. For an adjustable-duty fan, the fan static pressure P_s is plotted as a function of volumetric flow rate Q for each blade pitch angle. In this case, the blade pitch angle was kept constant at 34° . By convention, fan static pressure is *not* simply the difference in static pressure between the inlet and outlet but instead is defined as

$$P_s = P_t - P_v \quad (5.3)$$

$$= (P_{t2} - P_{t1}) - P_{v2} \quad (5.4)$$

$$= P_{s2} - P_{t1} \quad (5.5)$$

Since the stall cell measurements showed that the correlation of these rotating disturbances is successfully decreased by pulsed-DC casing plasma actuation, the next step was to quantify any change in stall margin due to this reduction. For each actuator location, the fan was throttled to stall at approximately 100%, 90%, and 70% of the design speed (3501 rpm, 3151 rpm, and 2449 rpm respectively). A baseline plasma-off data set and a plasma-on data set were acquired at each speed, resulting in six unique fan performance curves per location. Since the largest reduction in stall cell correlation was seen when all eight actuator segments were run at $f = 2$ kHz and $V_{\text{supply}} = 10$ kV, these operating conditions were also used to generate the plasma-on fan curves.

The inlet area of the fan was adjusted by rotating the cover to achieve several different flow rates. Then, for each throttle position, the data were acquired over 30 s and the airflow rate, velocity pressure, and static pressure were calculated as prescribed in AMCA 210. To maintain consistent flow rates between experiments, the different positions were marked on the throttling cover.

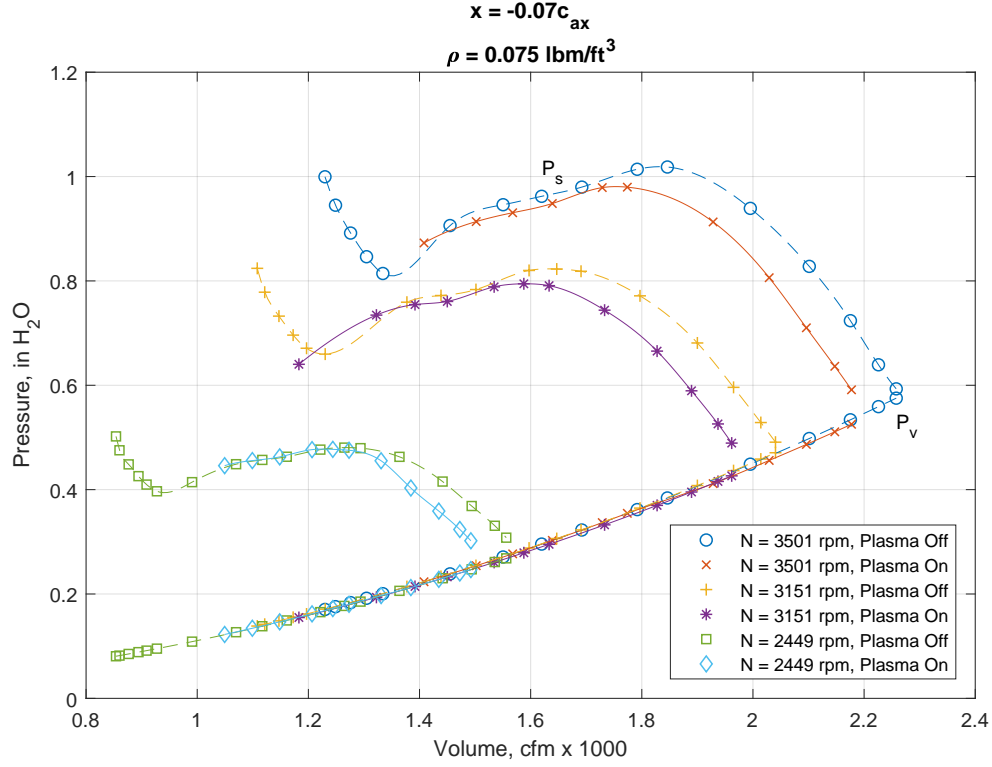


Figure 5.43. Fan performance curve for actuators at $x = -0.07c_{ax}$

The same actuator locations as were tested for the stall cell measurements were examined for the fan performance curves. Figures 5.43, 5.44, and 5.45 show the performance characteristics of the fan as measured in the lab for each location. The baseline fan curves differ from those provided by the manufacturer; this is assumed to be a result of changing the system by using a different test setup.

Although the plasma actuators slightly decreased the fan static pressure, the stall points were also shifted to lower flow rates. The decrease in fan static pressure is a result of an increase in the inlet static pressure. This increase causes P_{t1} in Equation 5.5 to rise. Although the outlet static pressure P_{s2} also increases, it is outweighed by the change in P_{t1} , explaining the net decrease in P_s . The plasma actuators add energy to the flow which can increase P_{t1} . If the stall cells are not

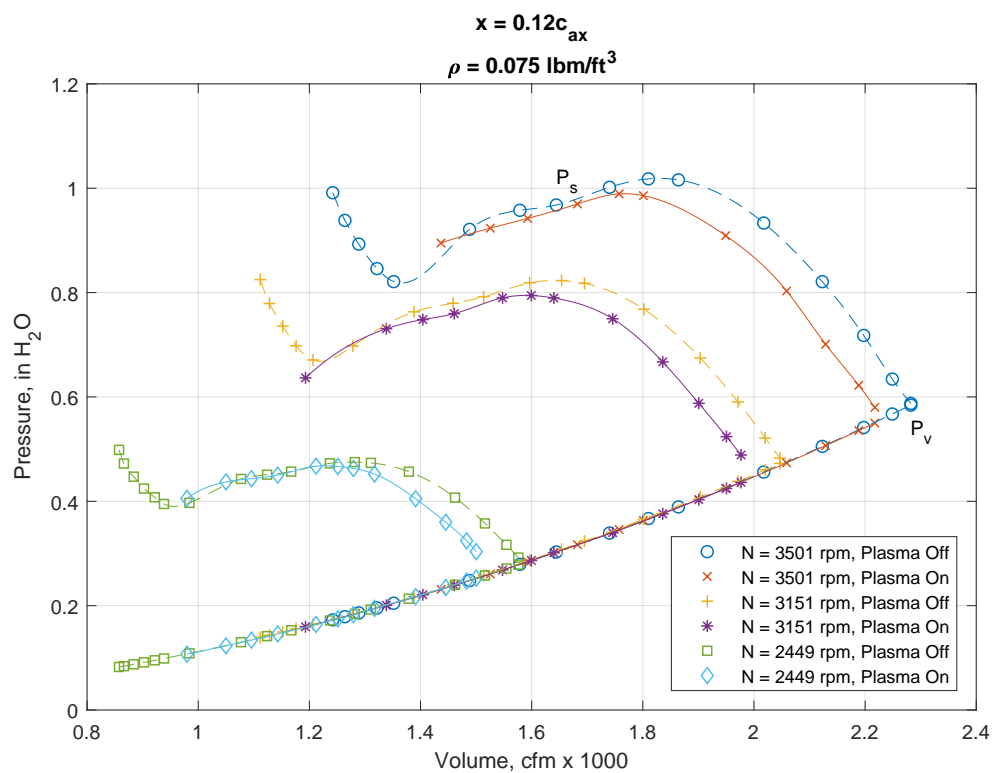


Figure 5.44. Fan performance curve for actuators at $x = 0.12c_{ax}$

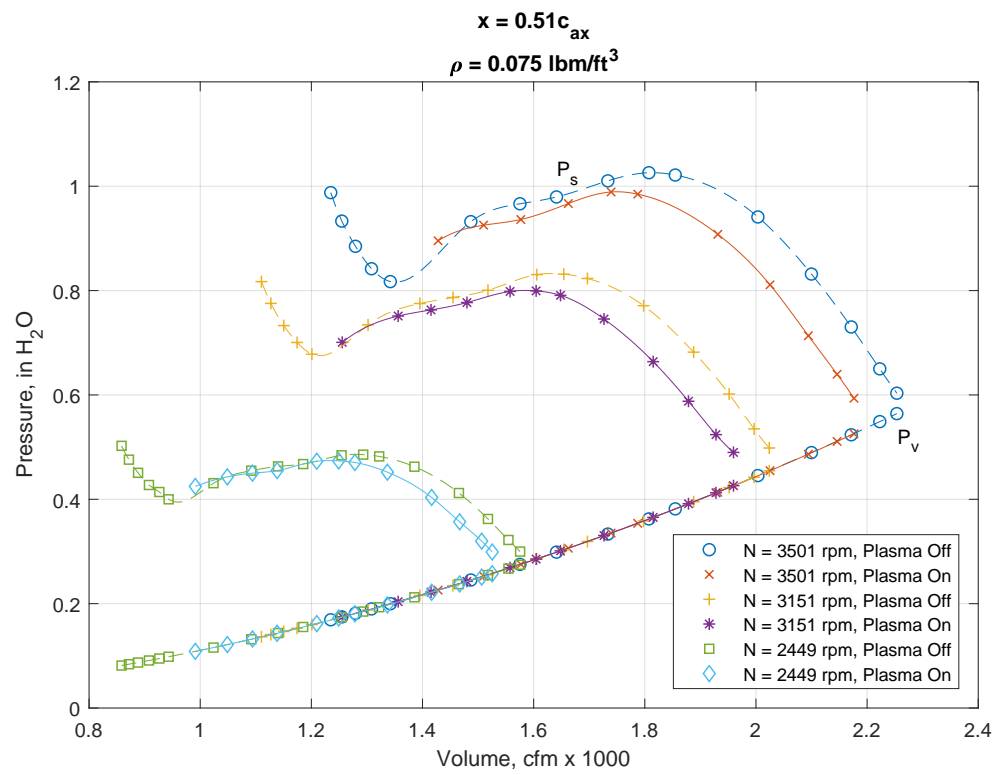


Figure 5.45. Fan performance curve for actuators at $x = 0.51c_{ax}$

completely eliminated but only partially diminished as demonstrated by the stall cell measurements, then they could still present a “blockage” to the flow which converts the added energy to static pressure at the inlet.

The stall margin improvement for an axial fan is defined in Equation 5.6, where the flow coefficient ϕ is the ratio between axial velocity and blade tip speed $V_{\text{in}}/U_{\text{tip}}$. This can be compared to the stall margin extension defined in Equation 3.3 and provides a means of quantifying the change in stall points seen in Figures 5.43, 5.44, and 5.45.

$$\text{SMI} = \frac{\phi_{s1} - \phi_{s2}}{\phi_{s1}} \quad (5.6)$$

The stall margin improvement due to the casing plasma actuation is tabulated in Table 5.3 for each actuator location and rotor speed. At 3501 rpm, the highest SMI was seen for actuator locations of $-0.07c_{ax}$ and $0.51c_{ax}$; this matches the trend in average SCM reduction from the stall cell measurements. It also suggests that the actuators may still be able to extend stall margin at locations farther upstream, which would be advantageous for preventing arcing to the blades in a metal fan or compressor. On the other hand, the highest SMI was seen for different actuator locations at 3151 and 2449 rpm, which is an important consideration if a plasma control scheme is to be used at non-design speeds.

TABLE 5.3
STALL MARGIN IMPROVEMENT FOR VARIOUS ACTUATOR
LOCATIONS

Rotational Speed	$-0.07c_{ax}$	$0.12c_{ax}$	$0.51c_{ax}$
3501 rpm	3.91%	2.90%	3.75%
3151 rpm	3.60%	3.30%	3.01%
2449 rpm	1.63%	5.45%	3.42%

CHAPTER 6

CONCLUSIONS AND RECOMMENDATIONS

In this chapter, several conclusions from the experimental characterization of the pulsed-DC actuator's thrust generation are presented. The initial work planned for the ND-TAC and subsequent experiments using the pulsed-DC actuator to control stall in the nonconductive fan facility are also summarized. Finally, a few areas are identified and recommended for future work to better understand the pulsed-DC actuator's flow physics and improve its stall control authority.

6.1 Conclusions

In Chapter 1, the pulsed-DC plasma actuator was presented as an alternative to conventional AC-driven plasma actuators, particularly for flow control applications in confined areas where a large body force at low operating voltages is needed. Delaying the onset of rotating stall in axial compressors and fans was identified as one such application. In Chapter 2, a stacked MOSFET switch for producing the pulsed waveform was designed and built, and the induced thrust generated by pulsed-DC DBDs was compared to that by AC DBDs. The objective was to maximize the thrust recorded by the mass balance, which is a metric of the body force generated by the plasma actuators. The results indicated that at atmospheric pressure, for the same input voltages, the thrust from the pulsed-DC operation was almost ten times larger compared to the AC operation. The thrust produced by pulsed-DC operation also exceeded the highest thrust produced by AC operation using thick dielectrics and input voltages that were ten times higher. Thus, the advantage of the pulsed-DC

plasma actuator is the ability to achieve very high body force levels at considerably lower voltages and with a thin form factor. This makes it considerably easier to incorporate into active flow control applications.

Further experiments were carried out in Chapter 2 to determine the effect of dielectric material, rise time, pulse amplitude, and static pressure on the thrust generation of the pulsed-DC actuator. In general, the thrust produced using an Ultem dielectric layer was less than that using a Kapton dielectric layer at low voltages. However, the slope of the thrust versus voltage line was higher for the Ultem actuator. The thrust was inversely proportional to the rise time: As the rise time was decreased by lowering R_{bias} , the thrust increased. Pulse amplitude was particularly important in ensuring optimal thrust generation. Since the depth of the pulse influences the amount of ionization, a faulty circuit which does not switch the covered electrode to ground completely will result in a significantly lower body force. Finally, the static pressure results indicated behavior similar to that investigated by Valerioti and Corke [38], with the thrust decreasing with increasing static pressure, reaching a minimum, and then beginning to increase again. However, the minimum occurred at 80 psig (5.5 bar) for the pulsed-DC actuator, while it occurred at 29 psig (2 bar) for the AC actuator.

In Chapter 3, a model developed by Ross [31] for predicting SME due to a circumferential groove casing treatment was modified for pulsed-DC casing plasma actuation instead. Assuming a generated thrust of 300 mN m^{-1} (which was attained with the pulsed-DC approach) a 3.4% stall margin extension can be obtained at compressor design conditions. It is important to note that this model cannot be applied to arbitrary compressors or fans, since some of the parameters are found by fitting curves to experimental data. However, if the necessary experiments or simulations were carried out for a given machine, the benefits of modifying that machine with a plasma casing treatment could then be weighed.

It was originally planned to validate the 3.4% SME prediction by manufacturing a survey ring for the ND-TAC facility which implemented a pulsed-DC plasma actuator in the casing. Chapter 4 discussed how this survey ring would have been used in experiments to observe the suppression of rotating stall cells as they traveled around the annulus of the compressor and past the actuator segment. Later, the survey ring would have been modified to include plasma actuators around the entire circumference so that a performance map could be constructed for the compressor with plasma actuation and compared to one for the smooth wall compressor. Unfortunately, the operating voltage required to generate the 300 mN m^{-1} of thrust still resulted in sparks between the exposed electrode and the rotor blades. An insulating coating of parylene was tested on the rotor but did not completely prevent sparking. DC offsets to reduce the voltage potential between the exposed electrode and rotor blades were also investigated, but these reduced the generated thrust.

Nonetheless, the experimental approach for measuring SME in the ND-TAC proved useful, and the new pulsed-DC plasma actuator was implemented for stall control in a nonconductive fan as covered in Chapter 5. The plasma actuators were shown to reduce stall cell correlation by almost 50% when arranged around the entire circumference of the rotor casing and operated at the highest frequencies and voltages. In most cases, this reduction in SCM caused a corresponding increase in stall margin, although the SME was negative when the fan speed was set to 3151 rpm. The stall margin was primarily increased by shifting the stall point to lower flow rates as opposed to increasing fan static pressure, and the highest values of SME (up to 4.03%) were seen for the slowest fan speed.

6.2 Recommendations

The discrepancies between the thrust measurements obtained from the electronic force scale and those from integration of the velocity profiles, as well as the fact

that the measured velocity profiles are not self-similar, illustrate the need for more detailed experiments to characterize the physics of the pulsed-DC plasma actuator. In particular, it has been shown that experimental setups using balances can be affected by the surrounding environment [1], while experimental setups using pitot probes can be affected by the location of the probe and require assumptions about the flow to be made [17]. Therefore, these variables must be accounted for when comparing the two methods of thrust measurement.

Particle image velocimetry (PIV) presents one alternative for velocity profile measurement which would allow for the flow through all sides of the control volume to be accounted for. It would also have increased spatial resolution as compared to a pitot probe setup and would not suffer from decreased signal-to-noise ratio due to EMI. However, dielectrophoresis of the seeding particles presents a challenge in ensuring adequate seeding distribution and accurate measurements—the particles must have the same density and electrical properties as air. Hot wire anemometers can also be used to measure velocity profiles and have the advantage of high temporal resolution, although care must be taken to make sure they aren't affected by electronic noise either.

The ideal method would be a nonintrusive technique unaffected by EMI or electrostatic forces that can measure the flow field produced by the actuator. Schlieren/shadowgraph imaging may prove useful in this respect and has been utilized for measurements of nanosecond-pulsed plasma [26], although the setup must be sensitive enough to resolve minute differences in air density and index of refraction since the velocities are relatively low.

Additionally, the actuator lifetime must be improved before the pulsed-DC actuator can be used in commercial applications. Organic polymers such as Kapton or Ultem will eventually degrade because they react with the ozone generated by the plasma. In spite of Ultem's increased resistance to ozone as compared to Kapton, the

actuators last no more than a few hours before the dielectric layer burns through and the two electrodes short. Inorganic materials such as silicone are impervious to ozone at the cost of lower dielectric strength and increased thickness, while ceramic materials have a high dielectric strength but are brittle. Mica is one inorganic material that is beginning to be used, but a more flexible solution must be found.

The SME model which was developed for the ND-TAC facility can still be validated if the arcing problem can be solved. As was mentioned before, the fan curve measurements indicated that actuator locations farther upstream may still be able to extend stall margin, and these would place the actuators farther away from the metal blades (but closer to other metal components in the compressor). Alternatively, further experiments and simulations could be performed on the nonconductive fan in order to find the missing parameters needed to model SME in this facility.

Eventually, the goal is to develop the pulsed-DC plasma actuator as an active method of flow control in axial compressors and fans. To this end, a feedback loop for stall control has yet to be designed and tested. The controller will have to be able to sense spike-type disturbances as they form and then adjust the plasma fast enough to effectively damp them.

APPENDIX A

ACTUATOR DIMENSIONS AND PROPERTIES

Actuator dimensions are shown in Figure A.1. Table A.1 lists the naming convention for each actuator configuration.

The materials used are listed below.

Electrode materials:

Saint-Gobain A603 aluminum foil tape

Backing thickness: 2.0 mil

Adhesive thickness: 2.0 mil

Saint-Gobain C661 copper foil tape

Backing thickness: 1.6 mil

Adhesive thickness: 2.4 mil

Dielectric materials:

CS Hyde 18-2S-2-36 Kapton tape

Backing thickness: 2 mil

CS Hyde 36-3A-2-5 Ultem tape

Backing thickness: 3 mil

CS Hyde 36-5A-2-5 Ultem tape

Backing thickness: 5 mil

Substrate materials:

McMaster-Carr 8667K241 G-10/FR4

Thickness: 1/16 in

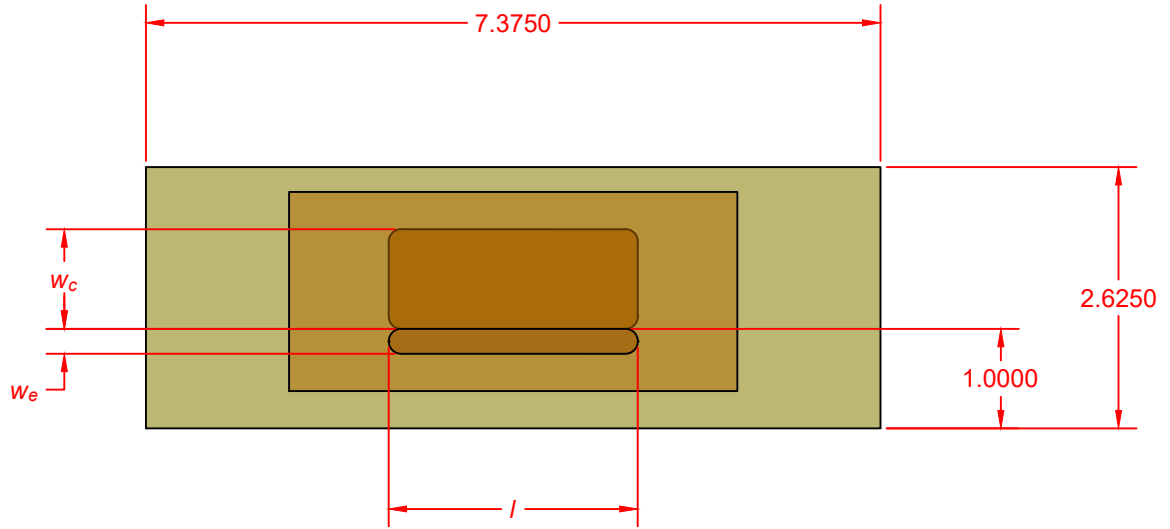


Figure A.1. Test article geometry and dimensions

TABLE A.1

ACTUATOR CONFIGURATIONS AND NOMENCLATURE

Configuration	Covered	w_c , in	Dielectric	t_d , mil	Exposed	w_e , in
CK4C	Cu	1	Kapton	4	Cu	1/4
CU3A	Cu	1	Ultem	3	Al	1/16
CU3C	Cu	1	Ultem	3	Cu	1/4
CU5A	Cu	1	Ultem	5	Al	1/16
CU5C	Cu	1	Ultem	5	Cu	1/4

APPENDIX B

MATLAB FUNCTIONS

```
function chi = scm(t,p,w,tau_min,tau_max)
%SCM Spatial correlation metric.
%   CHI = SCM(T,P,W,TAU_MIN,TAU_MAX) computes the spatial
%   correlation
%   metric of pressure P at time T as described in "
%   Analysis of Axial
%   Compressor Stall Inception Using Unsteady Casing
%   Pressure Measurements"
%   by Cameron and Morris. The spatial correlation metric
%   is based on a
%   windowed, two-point correlation function between
%   adjacent sensors and
%   provides a scalar function that is nonzero only when
%   disturbances that
%   rotate around the compressor annulus in the direction
%   of the rotor's
%   rotation are present.
%
%   W, the cross-correlation window length, specifies the
%   time scale
```

```

%   (length scale for rotating disturbances) at which the
%   "comparison" of
%   data traces is made. For example,  $W = 1/N$  will cause
%   CHI to be
%   sensitive to rotating disturbances with length scale
%   on the order of
%   the compressor circumference and smaller. TAU_MIN and
%   TAU_MAX, the time
%   lags, specify the desired rotational speed range.
%   Disturbances that are
%   rotating outside of the specified range of angular
%   velocity will not
%   contribute to the net CHI value.
%
%   For column-oriented data analysis, use SCM(T',P',W,
%   TAU_MIN,TAU_MAX).

%   Version 2017.06.15
%   Copyright 2017 Ryan McGowan

[n_theta,n_t] = size(p);
pNeighbor = [p(2:end,:);p(1,:)];
chi = zeros(n_theta,n_t);
parfor i = 1:n_theta
    for j = 1:n_t
        % Window home trace around t_0
        W = heaviside(t-(t(j)-w/2))-heaviside(t-(t(j)+w/2))
    end
end

```



```

    );
    pHat = p(i,:).*W;

    % Compute cross-correlation between windowed
    % signal and neighbor
    % time trace
    [R,lags] = xcorr(pHat,pNeighbor(i,:));

    % Compute SCM
    tau = lags*mean(diff(t));
    [~,i_tau_min] = min(abs(tau-tau_min));
    [~,i_tau_max] = min(abs(tau-tau_max));
    i_tau = i_tau_min:i_tau_max;
    chi(i,j) = trapz(tau(i_tau),R(i_tau));
end
end
end

```

BIBLIOGRAPHY

1. D. E. Ashpis and M. C. Laun. Thrust measurement of dielectric barrier discharge (DBD) plasma actuators: New anti-thrust hypothesis, frequency sweeps methodology, humidity and enclosure effects. Technical report, National Aeronautics and Space Administration, July 2014.
2. R. J. Baker and B. P. Johnson. Stacking power MOSFETs for use in high speed instrumentation. *Review of Scientific Instruments*, 63(12):5799–5801, December 1992.
3. J. P. Boeuf, Y. Lagmich, T. Unfer, T. Callegari, and L. C. Pitchford. Electrohydrodynamic force in dielectric barrier discharge plasma actuators. *Journal of Physics D: Applied Physics*, 40(3):652–662, February 2007.
4. J. D. Cameron and S. C. Morris. Analysis of axial compressor stall inception using unsteady casing pressure measurements. *Journal of Turbomachinery*, 135(2), March 2013.
5. T. C. Corke, B. Mertz, and M. P. Patel. Plasma flow control optimized airfoil. In *44th AIAA Aerospace Sciences Meeting and Exhibit*, January 2006.
6. T. C. Corke, M. L. Post, and D. M. Orlov. Single dielectric barrier discharge plasma enhanced aerodynamics: Physics, modeling and applications. *Experiments in Fluids*, 46(1):1–26, January 2009.
7. T. C. Corke, C. L. Enloe, and S. P. Wilkinson. Dielectric barrier discharge plasma actuators for flow control. *Annual Review of Fluid Mechanics*, 42:505–529, 2010.
8. G. Davidson and R. O’Neil. Optical radiation from nitrogen and air at high pressure excited by energetic electrons. *The Journal of Chemical Physics*, 41(12):3946–3955, December 1964.
9. I. J. Day. Active suppression of rotating stall and surge in axial compressors. *Journal of Turbomachinery*, 115(1):40–47, January 1993.
10. I. J. Day. Stall, surge and 75 years of research. In *Proceedings of ASME Turbo Expo 2015: Turbine Technical Conference and Exposition*, June 2015.
11. C. L. Enloe, T. E. McLaughlin, R. D. VanDyken, K. D. Kachner, E. J. Jumper, and T. C. Corke. Mechanisms and responses of a single dielectric barrier plasma actuator: Plasma morphology. *AIAA Journal*, 42(3):589–594, March 2004.

12. C. L. Enloe, T. E. McLaughlin, R. D. VanDyken, K. D. Kachner, E. J. Jumper, T. C. Corke, M. Post, and O. Haddad. Mechanisms and responses of a single dielectric barrier plasma actuator: Geometric effects. *AIAA Journal*, 42(3):595–604, March 2004.
13. Z. Falkenstein and J. J. Coogan. Microdischarge behaviour in the silent discharge of nitrogen–oxygen and water–air mixtures. *Journal of Physics D: Applied Physics*, 30(5):817–825, March 1997.
14. H. Fujita and H. Takata. A study on configurations of casing treatment for axial flow compressors. *Bulletin of JSME*, 27(230):1675–1681, August 1984.
15. H. L. Hess and R. J. Baker. Transformerless capacitive coupling of gate signals for series operation of power MOS devices. *IEEE Transactions on Power Electronics*, 15(5):923–930, September 2000.
16. P. G. Hill and C. R. Peterson. *Mechanics and Thermodynamics of Propulsion*. Addison-Wesley Publishing Company, Inc., 1992.
17. A. R. Hoskinson, N. Hershkowitz, and D. E. Ashpis. Force measurements of single and double DBD plasma actuators in quiescent air. *Journal of Physics D: Applied Physics*, 41(24), December 2008.
18. T. Houghton and I. Day. Stability enhancement by casing grooves: The importance of stall inception mechanism and solidity. *Journal of Turbomachinery*, 134(2), March 2012.
19. S. Kanazawa, M. Kogoma, T. Moriwaki, and S. Okazaki. Stable glow plasma at atmospheric pressure. *Journal of Physics D: Applied Physics*, 21(5):838–840, May 1988.
20. E. E. Kunhardt. Electrical breakdown of gases: The prebreakdown stage. *IEEE Transactions on Plasma Science*, 8(3):130–138, September 1980.
21. E. E. Kunhardt. Generation of large-volume, atmospheric-pressure, nonequilibrium plasmas. *IEEE Transactions on Plasma Science*, 28(1):189–200, February 2000.
22. G. Li, Y. Xu, L. Yang, W. Du, J. Zhu, and C. Nie. Low speed axial compressor stall margin improvement by unsteady plasma actuation. *Journal of Thermal Science*, 23(2):114–119, April 2014.
23. J. M. Meek and J. D. Craggs. *Electrical Breakdown of Gases*. John Wiley & Sons, 1978.
24. E. J. Mentze. A self-biased scalable high-voltage switching circuit for applications in low-voltage nanometer scale CMOS technologies and discrete power electronics. Master’s thesis, University of Idaho, December 2006.

25. E. Nasser. *Fundamentals of Gaseous Ionization and Plasma Electronics*. John Wiley & Sons, 1971.
26. D. F. Opaitis. Dielectric barrier discharge plasma actuator for flow control. Technical report, National Aeronautics and Space Administration, September 2012.
27. D. M. Orlov. *Modelling and Simulation of Single Dielectric Barrier Discharge Plasma Actuators*. PhD thesis, University of Notre Dame, October 2006.
28. D. M. Orlov, G. I. Font, and D. Edelstein. Characterization of discharge modes of plasma actuators. *AIAA Journal*, 46(12):3142–3148, December 2008.
29. J. D. Paduano, A. H. Epstein, L. Valavani, J. P. Longley, E. M. Greitzer, and G. R. Guenette. Active control of rotating stall in a low-speed axial compressor. *Journal of Turbomachinery*, 115(1):48–56, January 1993.
30. M. L. Post. *Plasma Actuators for Separation Control on Stationary and Oscillating Airfoils*. PhD thesis, University of Notre Dame, April 2004.
31. M. H. Ross. *Tip Clearance Flow Interaction with Circumferential Groove Casing Treatment in a Transonic Axial Compressor*. PhD thesis, University of Notre Dame, December 2013.
32. J. R. Roth and X. Dai. Optimization of the aerodynamic plasma actuator as an electrohydrodynamic (EHD) electrical device. In *44th AIAA Aerospace Sciences Meeting and Exhibit*, January 2006.
33. H. Saathoff and U. Stark. Tip clearance flow induced endwall boundary layer separation in a single-stage axial-flow low-speed compressor. In *ASME Turbo Expo 2000: Power for Land, Sea, and Air*, May 2000.
34. A. Shabbir and J. J. Adamczyk. Flow mechanism for stall margin improvement due to circumferential casing grooves on axial compressors. *Journal of Turbomachinery*, 127(4):708–717, October 2005.
35. G. D. J. Smith and N. A. Cumpsty. Flow phenomena in compressor casing treatment. *Journal of Engineering for Gas Turbines and Power*, 106(3):532–541, July 1984.
36. J. Sontag, S. Gordeyev, A. Duong, F. O. Thomas, and T. C. Corke. Studies of pulsed-DC plasma actuator and its effect on turbulent boundary layers using novel optical diagnostics. In *AIAA Aviation and Aeronautics Forum and Exposition*, June 2018. Pending publication.
37. F. O. Thomas, T. C. Corke, M. Iqbal, A. Kozlov, and D. Schatzman. Optimization of dielectric barrier discharge plasma actuators for active aerodynamic flow control. *AIAA Journal*, 47(9):2169–2178, September 2009.

38. J. A. Valerioti and T. C. Corke. Pressure dependence of dielectric barrier discharge plasma flow actuators. *AIAA Journal*, 50(7):1490–1502, July 2012.
39. R. J. Vidmar and K. R. Stalder. Air chemistry and power to generate and sustain plasma: Plasma lifetime calculations. In *41st Aerospace Sciences Meeting and Exhibit*, January 2003.
40. H. D. Vo. Suppression of short length-scale rotating stall inception with glow discharge actuation. In *ASME Turbo Expo 2007: Power for Land, Sea and Air*, May 2007.
41. H. D. Vo. Rotating stall suppression in axial compressors with casing plasma actuation. *Journal of Propulsion and Power*, 26(4):808–818, July 2010.
42. H. D. Vo, J. D. Cameron, and S. C. Morris. Control of short length-scale rotating stall inception on a high-speed axial compressor with plasma actuation. In *Proceedings of ASME Turbo Expo 2008: Power for Land, Sea and Air*, June 2008.
43. H. D. Vo, C. S. Tan, and E. M. Greitzer. Criteria for spike initiated rotating stall. *Journal of Turbomachinery*, 130(1), January 2008.
44. A. R. Wadia, G. Jothiprasad, and S. Saddoughi. The effect of plasma actuators on tip clearance flows in compressor rotors. In *28th International Congress of the Aeronautical Sciences*, September 2012.
45. H. J. Weigl, J. D. Paduano, L. G. Frechette, A. H. Epstein, E. M. Greitzer, M. M. Bright, and A. J. Strazisar. Active stabilization of rotating stall and surge in a transonic single-stage axial compressor. *Journal of Turbomachinery*, 120(4): 625–636, October 1998.